3D Super Level non-LTE Radiative Transfer for Molecules

Dissertation
zur Erlangung des Doktorgrades
des Fachbereichs Physik
an der Fakultät für Mathematik, Informatik und Naturwissenschaften
der Universität Hamburg

vorgelegt von

Alexander Berkner

aus Stuttgart

Hamburg
2015

Gutachter der Dissertation:	Prof. Dr. Peter Hauschildt Prof. Dr. Eddie Baron
Mitglieder der Prüfungskommission:	Prof. Dr. Dieter Horns Prof. Dr. Peter Hauschildt Prof. Dr. Robi Banerjee Prof. Dr. Marcus Brüggen Dr. Robert Baade
Datum der Disputation:	16.01.2015
Vorsitzende des Promotionsausschusses:	Prof. Dr. Daniela Pfannkuche
Dekan der MIN-Fakultät:	Prof. Dr. Heinrich Graener
Leiter des Fachbereichs Physik:	Prof. Dr. Peter Hauschildt

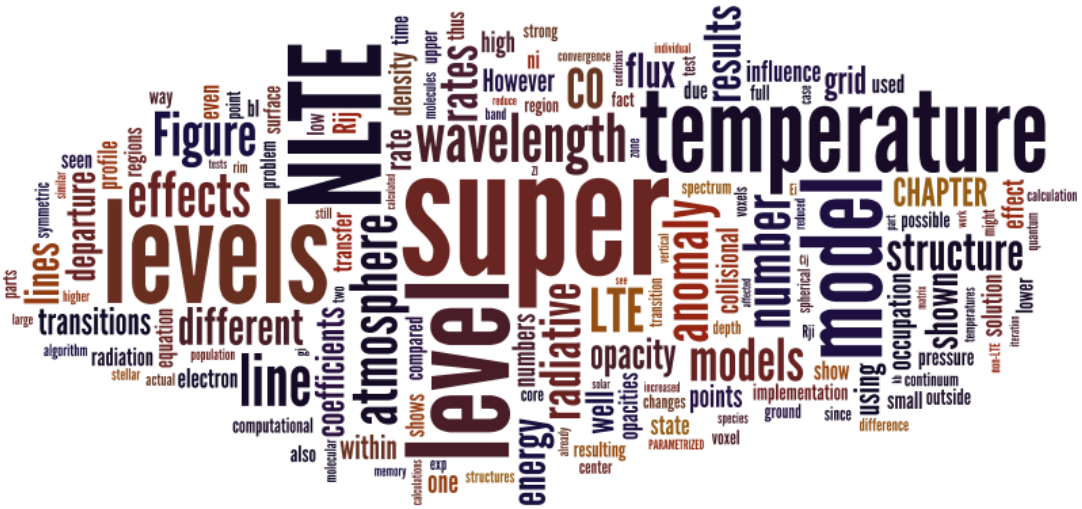
super
level
levels
temperature
NLTE
model
wavelength
atmosphere
effects
Figure
line
lines
different
structure
anomaly
number
models
radiative
results
rates
flux
CO
LTE
opacity
CHAPTER
transitions
departure
coefficients
energy
shown
occupation
grid
influence
points
density
rate
collisional
profile
radiation
electron
within
well
opacities
state
implementation
pressure
solution
effect
However
high
upper
molecules
time
thus
strong
convergence
individual
test
used
full
case
region
band
reduce
fact
due
spectrum
voxels
possible
calculation
quantum
work
might
matrix
temperatures
iteration
non-LTE
lower
continuum
outside
small
using
since
difference
ground
species
voxel
changes
increased
PARAMETRIZED
center
resulting
solar
already
core
numbers
exp
memory
calculations
structures
one
shows
compared
molecular
also
computational
actual
stellar
population
algorithm
large
higher
parts
symmetric
similar
seen
regions
tests
rim
problem
surface
bl
point
even
way
low
Rij
transfer
still
two
equation
gi
calculated
spherical
Cji
reduced
affected
Rji
Ei
vertical
transition
depth
show
zone
see
Zi
ni
conditions
part
kb

Abstract

Non-local thermodynamic equilibrium (NLTE) effects are relevant in regions, where strong radiation fields dominate the level populations so that they can not be determined using Boltzmann statistics. In many cases, this is true for optically thin regions with low temperature and pressure that are also rich in molecules. However, due to the fact that molecules have a large number of excited states, solving the rate equations directly is computationally expensive, especially for large scale 3D simulations.

To overcome this problem, a "super level" algorithm was implemented. Here, individual actual levels are combined into super levels reducing the rank of the equation system that needs to be solved. The new implementation was tested extensively and was able to reproduce the results of the well tested 1D implementation.

Results did show that combining actual levels into super levels can reduce the computational demands. In particular, the memory requirements were reduced significantly, as the full NLTE calculations were proven to exceed available memory even for a single voxel. While still a huge amount of computing time is necessary to calculate the radiative rates, a significant speed-up with respect to the solution of the rate equations was achieved.

During tests of the super level method, the accuracy of the full NLTE solution using actual levels was mostly retained, granted that the logic sorting levels into super levels reflects the physical conditions. In cool stellar atmospheres, several super level configurations that include energy as a criterion have proven to be accurate. Another method that combined levels with large energy ranges into super levels could not reproduce the full NLTE effects in.

In the two atmosphere structures tested, the NLTE effects for the CO molecule proved to be limited to the $\Delta\nu = 1$ band. The $\Delta\nu = 2$ CO lines in the mid infrared were shown to form at a depth that is mostly unaffected by NLTE effects as the collisional rates are still large.

A small zone of locally reduced temperature was introduced into an M-dwarf atmosphere, were NLTE effects were shown to be persistent in the entire upper atmosphere, as well as a solar like G-type atmosphere, where no strong NLTE effects were present outside the temperature anomaly. In both cases, the reduced temperature caused strong NLTE effects, changing the opacity structure of the entire atmosphere. This produced a significant influence on the resulting surface profiles and the outgoing spectrum. While the surface brightness is linked directly to the temperature structure in LTE, NLTE effects act as an equalizer between hot and cool regions, spreading the effects of the low temperature zone beyond its physical limits, reducing the maximum contrast. This effect is caused by the NLTE opacities affecting the depth at which a line is formed. This indicates the influence that NLTE effects have on the temperature structure already seen in 1D models.

Zusammenfassung

Effekte des nicht-lokalen thermodynamischen Gleichgewichts (NLTE) sind dort relevant, wo das Strahlungsfeld die Besetzung der Zustände bestimmt, so dass die Besetzungszahlen nicht der Boltzmann-Statistik genügen. In vielen Fällen ist dies in optischen dünnen Regionen mit geringer Temperatur und geringem Druck der Fall, welche reich an Molekülen sind. Aufgrund der großen Anzahl an Zuständen erfordert die Lösung der Ratengleichungen für Moleküle allerdings viel Rechenzeit.

Um dieses Problem zu umgehen, wurde der Super-Level Algorithmus implementiert. Dieser kombiniert einzelne Molekül-Zustände zu Super-Zuständen oder auch Super-Leveln. Hierdurch wird die Ordnung des Gleichungssystems, welches gelöst werden muss, verringert. Die neue Implementation wurde ausgiebig getestet und konnte Ergebnisse der gut getesteten 1D Implementation erfolgreich reproduzieren.

Die Ergebnisse haben gezeigt, dass die Zusammenfassung in Super-Level die rechentechnischen Anforderungen senkt. In erster Linie wird der Speicher-Verbrauch erheblich reduziert, was notwendig ist, da eine Rechnung in vollem NLTE selbst für nur einen Voxel den zur Verfügung stehenden Speicher übersteigt. Die benötigte Rechenzeit zur Lösung der Ratengleichungen konnte erheblich reduziert werden, so dass sie im Vergleich zur Berechnung der Strahlungsraten kaum noch eine Rolle spielt.

Der Super-Level Algorithmus produzierte Ergebnisse, welche gut mit den Ergebnissen einer vollen NLTE Rechnung übereinstimmten, vorausgesetzt die Sortierung der Level in Super-Level spiegelte die physikalischen Gegebenheiten wieder. In kühlen Atmosphären haben sich mehrere Methoden, welche Energie als eines der Kriterien verwenden, als akkurat erwiesen. Eine Methode, in der Zustände mit großen Energieunterschieden kombiniert wurden, erwies sich hingegen als ungeeignet.

In den Atmosphären, welche in diesen Tests verwendet wurden, zeigte sich, dass die NLTE Effekte im Spektrum auf das $\Delta\nu = 1$ Band beschränkt sind. Die $\Delta\nu = 2$ Linien von CO formieren sich hingegen in einer Tiefe, in der die NLTE Effekte aufgrund von hohen Kollisionsraten gering sind.

Eine kleine Zone geringer Temperatur wurde in eine M-Zwerg Atmosphäre eingebracht, welche auch außerhalb NLTE Effekte zeigt, weiterhin in eine sonnenähnliche G-Typ Atmosphäre, die außerhalb keine starken NLTE Effekte zeigt. In beiden Fällen zeigte sich, dass die verringerte Temperatur starke NLTE Effekte und dementsprechend veränderte Opazitäts-Strukturen erzeugt. Dies hat einen starken Einfluss auf die Oberflächen-Helligkeit und das ausgehende Spektrum. Während die Oberflächen-Helligkeit in LTE direkt von der Temperaturstruktur abhängt, wirken die NLTE Effekte als Ausgleich zwischen heißen und kalten Regionen. Hierbei verteilt sich der Effekt auf eine größere Fläche während gleichzeitig der Kontrast reduziert wird. Der Grund hierfür ist die Veränderung der Sichttiefe durch die NLTE Opazitäten. Dies zeigt, dass NLTE Effekte einen Einfluss auf die Temperaturstruktur selbst haben, wie in 1D Fällen bereits gezeigt wurde.

Contents

"Somewhere, something incredible is waiting to be known."
– Carl Sagan

Chapter 1

Introduction

Light is among the few sources of information available to us, if we aspire to decode the manifold mechanisms at work within a star. As such, it is of utmost importance to understand the interaction between light and matter that takes place when the light produced in the hot stellar interior passes through the outer shell of the star before it can be observed.

This interaction is a complicated process, as the radiation field interacts with the matter within the star and both shapes it, and is shaped by it in return. Over the past two decades it has become a common practice to use synthetic spectra, produced by detailed radiative transfer simulations, to decipher information about the stars interior, and the processes therein that are encoded in the spectrum of a star. This is especially important, since, with the currently available instruments, the surface of no other star than the sun can be fully resolved, so that the only information available to us is the integrated spectrum produced by the various interactions of the light with the stellar matter.

Synthetic spectra obtained by 1D radiative transfer have been available and successfully used to put our understanding of the conditions within a star to a test as well as attain to additional information about stars as such, for the past twenty years using codes such as the Phoenix/1D atmosphere simulation code as described by, e.g., Hauschildt [1992, 1993], Hauschildt and Baron [1999].

In this respect, it is often assumed that the star is in *Local Thermodynamic Equilibrium* or *LTE*, to determine the occupation numbers of all atomic and molecular levels, which are relevant to deduce the strength of spectral lines for the purpose of the simulation. However, this is frequently a very bad approximation, as the radiation field has its own influence on the state of each atom, and in turn is also influenced by the rate of absorptions and emissions, thus, creating a feedback with the matter within the atmosphere. To include this, *non-LTE* calculations, in which the rate equations for all populations and depopulations are calculated directly, have become more commonly used.

In the case of molecules, this poses an additional challenge, as molecules have a very large number of excited levels, which leads to very large system of equations that need to be solved. In 1D, solving large systems for, at least, a select number of molecular species is possible with current computational capabilities, as the number of spatial points, where the equations systems need to be solved is small.

Yet, the temperature and pressure structure and, thus, all other physical conditions

within a star are not solely determined by the distance from the stellar core. From observations of the resolved surface of the sun, it is known that the photosphere shows both large-scale, as well as small-scale temperature variations caused by the complex convection patterns in the outer shell of the star. These patterns occur both in the form of granulation, as well as the formation of spots and pores as the most obvious features of a non-uniform temperature structure.

In other words, the temperature and pressure structures of a star is highly dependent on horizontal and lateral position with temperature deviations that range up to a couple of thousand degrees for the coolest spots seen on the stellar surface compared to the mean temperature in that layer of the atmosphere. Apart from the different temperature patterns caused by convection, a large number of other reasons for non spherical symmetric temperature or pressure structure can occur in stars other than the sun. A stellar companion might induce a zone of high temperature due to irradiation, which would be another localized feature on the surface, but would at the same time, have additional consequences for the radiation field for half of the stellar surface. Another example of a more global feature could be accretion induced heating caused by the disk surrounding a young star.

Thinking beyond stars, exo-planets can have even more assymetric temperature structures created by the difference between the irradiated and the non-irradiated side. This is especially true for planets in close orbit around their primary. While radial velocity or transit methods can only obtain information about the size and the mass of a planet, transition or reflectance spectra could give additional information about both the surface and a possible atmosphere of an exo-planet if they can be retrieved out of the total spectrum of star and planets combined. However, this requires detailed modelling of both.

To include the possible diverse temperature structure of a star or planet, the radiative transfer needs to be solved in 3D. While this is a great deal more expensive in terms of computational demands, it is no longer an impossibility thanks to the large parallel computer systems that are available today. Hence, the influence these diverse structures have on the resulting total spectrum can now be simulated consistently, limited only by the spatial resolution the available computational time allows for.

The 3D radiative transfer code PHOENIX/3D that was extended and employed for this work, is described by a dedicated series of papers Hauschildt and Baron [e.g. 2014]. 3D temperature variations have already been proven to have an influence on the opacity structure within the atmosphere, the angle integrated outgoing spectrum and the limb variations on the resolved surface by, e.g., Berkner et al. [2013].

Of course, simulating the stellar atmosphere in 3D poses an additional number of challenges and vastly increases the computational requirements. For this reason, solving the non-LTE problem in 3D is an additional strain on the already limited computational capabilities available as it requires the solution of a potentially large system of equations for a large number of spatial points as well as the solution of the radiative transfer problem for a sufficient number of wavelength points. For atoms, this has recently been implemented into PHOENIX/3D, as described by Hauschildt and Baron [2014]. However, for molecules, the task is even more laborious, as the number of molecular levels is extensive. Thus, the size of the system of equations that needs to be solved for every spatial point increases as well.

Nonetheless, it was already proven by Schweitzer [1999] and Schweitzer et al. [2000] that molecular NLTE has an undeniable influence on the vertical temperature structure. It stands to reason that molecular NLTE effects will affect lateral temperature variations as well. In particular, as optically thin regions that are dominated by NLTE effects often also show low temperatures that cause an increased formation of molecules. Here, we can expect that temperature variations will cause an even more diverse pattern of opacities and, as such, an influence on the temperature structure itself in NLTE than in LTE. This could possibly create a feedback loop that would require a temporal relaxation and affect the life time of features such as spots.

Furthermore, apart from low temperature or pressure regions, any region where the level populations are determined by a radiation field that connects spatially distant parts of the atmosphere and is rich in molecules will be influenced by NLTE effects. For instance, this is also true in the low density, high temperature chromosphere, where CO is still found at least in the lower layers, as shown by, e.g., Wedemeyer et al. [2004].

This work uses a method that was first conceived to reduce the complexity of the non-LTE problem for atoms in 1D to implement 3D molecular non-LTE radiative transfer into the existing 3DRT framework of PHOENIX. This method is described in detail in chapter 3 and the implementation is described in chapter 4.

The purpose of this work was to test the implementation with respect to computational effort, stability and accuracy. Furthermore, it was our aim to compare different models and investigate, which super level configuration would show the most reasonable balance between computational effort and accuracy of the result.

In this work, we have focused on two different scenarios. The atmospheres of cool stars such as M-dwarfs that are by their very nature rich in molecules, have a temperature and pressure profile that suggest strong NLTE effects in their outer atmosphere even without the inclusion of lateral temperature variations. On the other hand, cool zones in hotter stars, as for instance solar-like G-Type stars, can be both rich in molecules and show NLTE effects, where no significant effects would be expected outside of the zone. In this way, the second scenario was especially well suited to determine NLTE effects on the temperature structure.

Chapter 2

NLTE Radiative Transfer

The theory of radiative transfer explains how the electromagnetic radiation field changes, when it interacts with matter. Numerous species of atoms and molecules interact with the radiation field through absorption and emission of photons of various wavelengths, depending on their excitation state. Each species of atoms and molecules can absorb and emit photons continuously, as well as at a number of specific wavelengths, which results in a set of spectral lines. These lines depend strongly on the various properties of the matter, for instance on the density of the species, but also on the temperature, pressure and excitation state of each atom or molecule. In the case of stellar atmospheres, radiative transfer determines, how the radiation that originates from the stellar core changes while it passes through the stellar atmosphere and thus, how the resulting spectrum, which can be observed, will appear. Furthermore, it is also an important mechanism of energy transport within the atmosphere.

This chapter is meant as a reminder of the general principles of radiative transfer, introducing the necessary variables and concepts that are needed to solve the radiative transfer problem within the confines of a stellar atmosphere, as is the purpose of this work. The deliberations of this chapter are based upon the works of Rutten [2003], Mihalas [1970, 1978], Hauschildt [1992, 1993] and Hauschildt and Baron [2014] unless indicated otherwise.

2.1 Radiative Transfer

Electromagnetic radiation of any wavelength λ that passes trough matter, will interact with the matter and both influence it and be influenced by it in turn. Photons of a certain wavelength λ may be absorbed by a certain atomic species with a very high cross-section, while the cross-section for photons of a different wavelength is considerably smaller. Each atomic and molecular species produces different spectral lines and continua. However, the strength of a line is not only influenced by the presence or absence or even abundance of a species, but also by the excitation state the atom or molecule is in.

This makes radiative transfer a fairly complicated problem, which can be reduced to a single question: What happens to the *intensity*

$$I_\lambda = I_\lambda(\vec{r}, \vec{n}, \lambda) \tag{2.1}$$

which is the energy per unit wavelength interval transported by a beam of radiation of

the wavelength λ at a point $\vec{r}$ in the direction of $\vec{n}$, into a unit solid angle per unit time before it reaches $\vec{r} + d\vec{r}$?

Generally speaking, the matter along the path of a photon, following the *characteristic* $d\vec{r}$, will emit a certain amount of radiation, and, at the same time, absorb a certain amount of radiation. The latter is of course dependent on the amount of incoming radiation. This can be expressed as

$$dI_\lambda = \eta_\lambda(\vec{r}) \cdot d\vec{r} - \rho(\vec{r})\chi_\lambda(\vec{r})I_\lambda(\vec{r}) \cdot d\vec{r}, \tag{2.2}$$

defining the emissivity

$$\eta_\lambda(\vec{r}, \lambda) = \sum_{i<j} \eta_{ij}(\lambda, \vec{r}) + \widetilde{\eta}(\vec{r}, \lambda) \tag{2.3}$$

as the amount of radiation emitted per unit length, and the opacity

$$\chi_\lambda(\vec{r}, \lambda) = \sum_{i<j} \kappa_{ij}(\lambda, \vec{r}) + \widetilde{\kappa}(\vec{r}, \lambda) + \widetilde{\sigma}(\vec{r}, \lambda) \tag{2.4}$$

as the amount of radiation absorbed per path length and density ρ. Here, η_{ij}, κ_{ij} are emission and absorption coefficient, respectively, for each bound-bound transition between levels i and j. $\widetilde{\eta}$ is the background emission, $\widetilde{\kappa}$ is the background absorption and $\widetilde{\sigma}$ is the background scattering coefficient.

The *source function* can be defined as the local ratio of emission and absorption:

$$S_\lambda = \frac{\eta_\lambda}{\chi_\lambda}, \tag{2.5}$$

and the *optical depth* τ_λ

$$d\tau_\lambda = \rho\chi_\lambda d\vec{r} \tag{2.6}$$

as an optical path length that is more convenient for radiative transfer calculations than physical coordinates. Using this, equation (2.2) can now be written as

$$\frac{dI_\lambda}{d\tau_\lambda} = S_\lambda - I_\lambda \tag{2.7}$$

which is the standard form of the radiative transfer equation along the path $d\tau$.

As a first order differential equation, eq. (2.7) can be solved formally, whenever $S_\lambda = S_\lambda(\tau_\lambda)$ is known for the entire length of $d\vec{r}$:

$$I_\lambda(\tau_\lambda) = I(0) \cdot \exp(-\tau_\lambda) + \int_0^{\tau_\lambda} S(t) \exp(t - \tau_\lambda) \cdot dt \tag{2.8}$$

τ_λ is defined as optical depth along the characteristic. However, the amount of radiation absorbed and emitted along the path element $d\vec{r}$, and, hereby, the source function, depends on the radiation that is scattered along the path element, which in case is dependent on the radiation field along $d\vec{r}$. This dependency can be written as:

$$S_\lambda = \varepsilon_\lambda B_\lambda + (1 - \varepsilon_\lambda) J_\lambda \tag{2.9}$$

where B_λ is the Planck function, ε_λ is the *thermalization parameter* and J_λ is the mean intensity

$$J_\lambda = \frac{1}{4\pi} \oint_{4\pi} I_\lambda d\Omega \tag{2.10}$$

Due to the fact that the source function is now a function of I_λ, equation (2.7) can not be solved directly. It requires an iterative solution, which can formally be expressed as:

$$J_\lambda = \Lambda S_\lambda \tag{2.11}$$

where Λ is the operator that calculates the mean intensity J_λ for a specific source function S_λ. This includes calculating the formal solution for a given S_λ and integrating over the whole solid angle space.

While this would already allow for a rather direct iteration scheme, this scheme would show a very bad convergence rate for large optical depth τ and small values of ε_λ, i.e. cases of strong scattering. (See e.g. Hauschildt and Baron [2006], Mihalas [1978]).

Instead of directly implementing an iteration scheme for equation (2.11), it is possible to employ an operator splitting method, as suggested by Cannon [1973]. This is done by splitting the Λ operator as:

$$\Lambda = (\Lambda - \Lambda^*) + \Lambda^* \tag{2.12}$$

$$\Delta\Lambda \equiv (\Lambda - \Lambda^*) \tag{2.13}$$

so that

$$J_\lambda = [\Delta\Lambda + \Lambda^*]\,[S_\lambda] \tag{2.14}$$

and, with an iteration scheme in mind, rewritten to

$$J_\lambda^{(n+1)} = [\Lambda^*]\,[S_\lambda^{(n+1)}] + ([\Lambda] - [\Lambda^*])\,[S_\lambda^{(n)}] \tag{2.15}$$

Using equation (2.9) this can be reduced to the following expression to obtain the mean intensity for the next iteration $J_\lambda^{(n+1)}$ from the results of the previous iteration:

$$J_\lambda^{(n+1)} = (1 - \Lambda^*(1 - \varepsilon_\lambda))^{-1} \left(J_{FS} - [\Lambda^*] \left[(1 - \varepsilon_\lambda)\, J_\lambda^{(n)} \right] \right) \tag{2.16}$$

where $J_{FS} = [\Lambda] \left[S_\lambda^{(n)} \right]$ is the result of the formal solution for the previous iteration.

Using this so called *Approximate Lambda Iteration* method will be significantly faster, depending on the choice of the approximate lambda operator Λ^*. Different choices for Λ^* are discussed by e.g. Hauschildt [1992], Olson and Kunasz [1987].

At this point, the radiative transfer problem can be solved, as long as the relevant physical properties are known for each point of the stellar atmosphere. In this case, the relevant properties are for example temperature T, pressure p, density ρ, as well as emissivity η_λ and opacity χ_λ for all wavelength points.

2.2 The Non-LTE Problem

The solution shown in the previous section requires that the opacity χ_λ and the emissivity η_λ are known for all wavelengths. Absorption and emission include bound-bound and bound-free, as well as free-free transitions for a possibly large number of atomic and molecular species. There are three kinds of radiative transitions with transition rates described by the Einstein coefficients, as defined by Einstein [1917]:

spontaneous emission: A photon of wavelength λ_{ij} and energy $E = E_j - E_i$ is emitted spontaneously with a rate expressed by the Einstein coefficient for spontaneous emission A_{ji}

stimulated emission: The emission of a photon of wavelength λ_{ij} is stimulated by the reaction with another photon of the same wavelength. This occurs with a rate expressed by the Einstein coefficient for stimulated emission B_{ji} and proportional to the local mean intensity $J(\lambda)$.

absorption: A photon of wavelength λ_{ij} is absorbed with a rate dependent on the Einstein coefficient for absorption B_{ij}.

Each individual transition contributes to the total absorption and emission coefficients $\chi_\lambda, \eta_\lambda$ as defined in equations 2.4 and 2.3. The contribution of each transition is dependent on the population densities n_i, n_j of the atomic or molecular levels that are coupled to each transition $i \longleftrightarrow j$:

$$\eta_{ij}(\lambda) = \frac{2hc^2}{\lambda^5}\frac{g_i}{g_j}\alpha_{ji}(\lambda) \cdot n_j \tag{2.17}$$

$$\kappa_{ij}(\lambda) = \alpha_{ij}(\lambda)n_i - \alpha_{ji}(\lambda)\frac{g_i}{g_j} \cdot n_j \tag{2.18}$$

Transitions only contribute at certain wavelength. This is expressed through the transition cross sections $\alpha_{ji}(\lambda), \alpha_{ij}(\lambda)$, which give the probability that photon can be absorbed or emitted at wavelength λ. g_i, g_j are the statistical weights of each level.

It is often assumed that all parts of the atmosphere are in so called local thermodynamic equilibrium (LTE), so that it is possible to calculate the population densities for each species without much effort using the Saha-Boltzmann equation:

$$n_i^* = \frac{g_i}{g_\kappa} n_\kappa \frac{2h^3 n_e}{(2\pi m_e)^{3/2} \cdot (kT)^{3/2}} \exp\left(-\frac{E_i - E_\kappa}{kT}\right) \tag{2.19}$$

Here, g_i, g_κ are the statistical weights of levels i and κ, where κ is the ground state of the next ionization state of the same species with population density n_κ. E_i is the excitation energy of level i, E_κ is the ionization energy from the ground state of the current ionization stage. n_e is the electron density and m_e the electron mass.

However, this assumes that the population densities n_i for each level of each atomic or molecular species are solely dependent on the local temperature, and independent of the radiation field. This is an assumption that does not hold in all cases.

To calculate the population densities for each atomic or molecular level, without the assumption of LTE, it is necessary to solve the rate equations for the entire system directly and consistently, here written for a single level i:

$$\underbrace{\sum_{j<i} n_j P_{ji} + \sum_{j>i} n_j P_{ji}}_{\text{Transitions into level } i} = \underbrace{n_i \left(\sum_{j>i} P_{ij} + \sum_{j<i} P_{ij} \right)}_{\text{Transitions out of level } i} \tag{2.20}$$

which is basically a conservation-equation balancing all population and de-population processes for every level. n_i, n_j are the population densities and P_{ij} is the total rate coefficient:

$$P_{ij} = R_{ij} + C_{ij} \tag{2.21}$$

consisting of the radiative rate coefficient R_{ij} as well as the collisional rate coefficient C_{ij} for the transition from i to j.

2.2.1 Radiative Rates

Assuming that $j > i$ we can write the absorption rate R_{ij} for transitions $i \rightarrow j$ as

$$\begin{aligned} R_{ij} &= B_{ij} \overline{J} \\ &= \frac{4\pi}{hc} \cdot \int_0^\infty \alpha_{ij}(\lambda) J(\lambda) \mathrm{d}\lambda \end{aligned} \tag{2.22}$$

with

$$\alpha_{ij}(\lambda) = \frac{hc}{4\pi} \frac{\lambda_{ij}}{c} B_{ij} \phi_{ij} \tag{2.23}$$

and the emission rate R_{ji} for transitions $i \leftarrow j$ as

$$R_{ji} = \frac{4\pi}{hc} \cdot \int_0^\infty \alpha_{ji}(\lambda) \left(\frac{2hc^2}{\lambda^5} + J(\lambda) \right) \cdot \exp\left(-\frac{hc}{kT \cdot \lambda} \right) \mathrm{d}\lambda \tag{2.24}$$

with

$$\alpha_{ji}(\lambda) = \frac{hc}{4\pi} \frac{\lambda_{ij}}{c} B_{ij} \varphi_{ji} \tag{2.25}$$

This includes both stimulated and spontaneous emission and is written in the same way as done by Mihalas [1978] with an explicit Boltzmann factor n_j^*/n_i^* so that

$$P_{ij}^{\mathrm{em}} = n_i \left(\frac{n_j^*}{n_i^*} \right) R_{ij} + C_{ij} \tag{2.26}$$

where n_i^* and n_j^* are the LTE occupation numbers which are given by the Saha-Boltzmann equation 2.19.

$\alpha_{ji}(\lambda)$ and $\alpha_{ij}(\lambda)$ are the cross sections for wavelength λ for the upward and downward transitions, λ_{ij} is the rest wavelength of the transition $i \to j$, and ϕ_{ij}, φ_{ji} are the normalized absorption and emission profiles. In the special case of complete redistribution (CRD), absorption and emission profile are identical, so that

$$\varphi_{ji}(\lambda) = \phi_{ij}(\lambda)$$
$$\alpha_{ij}(\lambda) = \alpha_{ji}(\lambda)$$

Besides bound-bound transitions, there are also bound-free processes as in photo-ionization and photo-recombination to consider. The respective radiative rates $R_{i\kappa}$ and $R_{\kappa i}$ can be calculated in a similar fashion, with transition cross sections $\alpha_{i\kappa}$ and $\alpha_{\kappa i}$, coupled to the occupation numbers n_κ of the next ionization stage of the atom.

As the radiative rates can only be calculated when $J(\lambda)$ is known, there is, again, no direct solution for the NLTE problem.

2.2.2 Collisional Rates

Both atoms and molecules can not only be excited by radiation, but also by collision with other particles within the atmosphere. All possible collisions are included into the collisional rates C_{ij} and C_{ji}. Fortunately, these rates are independent of the radiation field, and only depend on the local temperature, density and partial pressures of the species that are considered. In regions of high temperature, the most numerous and relevant case is usually the collision with electrons. However, other species like hydrogen and helium atoms become relevant at lower temperatures, as the electron density declines with temperature.

In any case, where the occupation numbers solely depend on collisional excitation and no radiation field is present ($R = 0$) or relevant ($R \ll C$), the occupation numbers are determined exclusively by local conditions and LTE is restored.

The rates for collisional excitation and de-excitation are connected by

$$C_{ij} = \frac{g_i}{g_j} \exp\left(-\frac{\Delta E_{ij}}{k_b T}\right) \cdot C_{ji} = \frac{n_j^*}{n_i^*} C_{ji} \tag{2.27}$$

2.2.3 The Rate Operator

Using equations (2.26) and (2.27) in the equation for detailed balance (2.20) we can rewrite it as

$$\sum_{j<i} n_j \left(R_{ji} + C_{ji}\right) + \sum_{j>i} n_j \frac{n_i^*}{n_j^*} \left(R_{ji} + C_{ij}\right) = n_i \left(\sum_{j>i} \left(R_{ij} + C_{ij}\right) + \sum_{j<i} \frac{n_j^*}{n_i^*} \left(R_{ij} + C_{ji}\right) \right) \tag{2.28}$$

This equation system is closed by particle and charge conservation:

$$n_\kappa + \sum_i n_i = \text{const} \tag{2.29}$$

$$n_e + n_\kappa = \text{const} \tag{2.30}$$

where n_κ is the occupation number for ground state of the next ionization stage of the atom and n_e is the electron density. This equation system is non-linear in n_i and n_e, since the radiative rates depend on the occupation numbers for each level and the collisional rates C_{ij}, C_{ji} depend on the electron density.

To solve this equation system iteratively, it can be rewritten into an operator equation similar to equation (2.11), so that it is possible to apply the same operator splitting method as in the solution of the radiative transfer itself, with a radiative rate operator $[R_{ij}]$ and the population density operator $[n]$ so that:

$$R_{ij} = [R_{ij}]\,[n] \tag{2.31}$$

and inserting equation (2.22) and using eq. (2.11):

$$[R_{ij}]\,[n] = \frac{4\pi}{hc}\int_0^\infty \alpha_{ij}(\lambda)\Lambda(\lambda)S(\lambda)\lambda \mathrm{d}\lambda \tag{2.32}$$

Following Rybicki and Hummer [1991] the Λ Operator can be rewritten to remove the non linearity in n_i:

$$\Lambda(\lambda) = \Psi(\lambda)\left[\frac{1}{\chi(\lambda)}\right] \tag{2.33}$$

Using $S(\lambda) = \frac{\eta(\lambda)}{\chi(\lambda)}$, and defining an operator to calculate the emissivity from the population densities

$$[E(\lambda)]\,[n] \equiv \eta(\lambda) = \sum_{i<j}\eta_{ij}(\lambda) + \widetilde{\eta}(\lambda) \tag{2.34}$$

with $\eta_{ij}(\lambda)$ as the contribution of each transition to the total emissivity and $\widetilde{\eta}(\lambda)$ as background emissivity, equation (2.32) can be written as

$$[R_{ij}]\,[n] = \frac{4\pi}{hc}\left[\int_0^\infty \alpha_{ij}(\lambda)\Psi(\lambda)\,[E(\lambda)]\,\lambda \mathrm{d}\lambda\right][n] \tag{2.35}$$

In the same way, it it possible to introduce an operator form for the absorption rates from equation (2.24):

$$[R_{ji}]\,[n] = \frac{4\pi}{hc}\int_0^\infty \alpha_{ji}(\lambda)\left\{\frac{2hc^2}{\lambda^5} + \Psi(\lambda)\,[E(\lambda)]\,[n]\right\}\exp\left(-\frac{hc}{kT\lambda}\right)\lambda \mathrm{d}\lambda \tag{2.36}$$

Since a direct iteration scheme using these operators would suffer from the same problems as in the solution of the radiative transfer equation, it is possible to split these operators as was done for the Λ operator in equations (2.12) and (2.13) to introduce the approximate Lambda iteration method:

$$[R_{ij}] = \left([R_{ij}] - \left[R^*_{ij}\right]\right) + \left[R^*_{ij}\right] = [\Delta R_{ij}] + \left[R^*_{ij}\right] \tag{2.37}$$

$$[R_{ji}] = \left([R_{ij}] - \left[R^*_{ji}\right]\right) + \left[R^*_{ji}\right] = [\Delta R_{ji}] + \left[R^*_{ji}\right] \tag{2.38}$$

so that R_{ij} and R_{ji} can be written as

$$R_{ij} = [\Delta R_{ij}]\,[n_{\mathrm{old}}] + \left[R^*_{ij}\right]\,[n_{\mathrm{new}}] \tag{2.39}$$

$$R_{ji} = [\Delta R_{ji}]\,[n_{\mathrm{old}}] + \left[R^*_{ji}\right]\,[n_{\mathrm{new}}] \tag{2.40}$$

The split operators are now inserted into eq. (2.28) and, again following Rybicki and Hummer [1991], each occurrence of $n_{j,\mathrm{new}}\left[R^*_{ji}\right][n_{\mathrm{new}}]$ is replaced by $n_{j,\mathrm{old}}\left[R^*_{ji}\right][n_{\mathrm{new}}]$ to remove the non-linearity and write it in an iterative form:

$$\begin{aligned}
&\sum_{j<i} n_{j,\mathrm{old}}\left[R^*_{ji}\right][n_{\mathrm{new}}] - n_{i,\mathrm{old}}\left\{\sum_{j<i}\left(\frac{n^*_j}{n^*_i}\right)\left[R^*_{ij}\right][n_{\mathrm{new}}] + \sum_{j>i}\left[R^*_{ij}\right][n_{\mathrm{new}}]\right\} \\
&+\sum_{j>i} n_{j,\mathrm{old}}\left(\frac{n^*_i}{n^*_j}\right)\left[R^*_{ji}\right][n_{\mathrm{new}}] + \sum_{j<i} n_{j,\mathrm{new}}\left(\left[R^*_{\Delta ji}\right][n_{\mathrm{old}}] + C_{ji}\right) \\
&- n_{i,\mathrm{new}}\left\{\sum_{j<i}\left(\frac{n^*_j}{n^*_i}\right)\left([\Delta R_{ij}][n_{\mathrm{old}}] + C_{ij}\right) + \sum_{j>i}\left([\Delta R_{ij}][n_{\mathrm{old}}] + C_{ij}\right)\right\} \\
&+\sum_{j>i} n_{j,\mathrm{new}}\left(\frac{n^*_i}{n^*_j}\right)\left([\Delta R_{ji}][n_{\mathrm{old}}] + C_{ji}\right) \\
&= 0
\end{aligned} \tag{2.41}$$

which can now be solved to obtain a new set of n_i if all radiative and collisional rates are known. This system is still coupled to the electron density n_e since all collisional coefficients C_{ij} are dependant upon it. To solve the system, it is necessary to assume that n_e is constant during each iteration step, since the equation system is still non-linear in n_e.

The Non-LTE problem can now be solved iteratively. After the radiative transfer problem is solved for a given set of occupation numbers n_i, n_e, the rate operators $\left[R^*_{ij}\right]$ and $[\Delta R_{ij}]$ can be constructed using Λ and Λ^* from the solution of the radiative transfer equation, as the rate operators are built upon Ψ. Finally, equation system of (2.41) is solved to obtain the next set of n_i, n_e. This process is repeated until the desired precision is reached.

2.2.4 Departure Coefficients

To compare the resulting non-LTE population density n_i to the LTE population density n^*_i as introduced in equation (2.19) and quantify the strength of the non-LTE effect for each level at each point in the stellar atmosphere it is common to use *departure coefficients*

$$b_i = \frac{n_i}{n^*_i} \tag{2.42}$$

as used, e.g., by Mihalas [1978] and introduced in Menzel and Cillié [1937].

Chapter 3

The Super Level Algorithm

Solving the non-LTE problem, as described in the previous chapter, involves solving a linear equation system with a rank of the number of atomic and molecular levels included plus one. This involves the inversion of a matrix. Therefore, it is required to store all radiative rates, as well as all collisional rates for all transitions, for every volume cell of the computational domain.

Even simple molecules such as *carbon monoxide* have a vast number of individual levels and, thus, a large number of transitions have to be considered. Since 3D calculations with high spatial resolution may possibly consist of millions of voxels, in their computational domains while the equation system has to be solved for each voxel, this is computationally demanding. The memory requirements, just to store the data, are high.

To reduce the amount of computation time, as well as memory requirements, it is helpful to reduce the rank of the rate matrix by using the *super level algorithm*. Here, the number of individual molecular levels is artificially reduced by combining a set of actual levels into a super level. For this, the transitions between individual levels have to be combined into super transitions between super levels, as well. However, combining levels means not all actual levels and transitions are treated in full non-LTE, but only in an approximation thereof. This method allows for a trade-off between accuracy and the need to reduce the computational demands.

This chapter describes how the radiative rates for super transitions can be calculated to simplify the equation system (Eq. 2.41) and introduces several different super level definitions for the CO molecule.

To distinguish between real levels and super levels, indices for real levels will be denoted by lower case letters, while super level indices will be denoted by upper-case letters.

The super level algorithm, as a general approach, has been described by, e.g., Anderson [1989]. An implementation of the algorithm for CO molecules for 1D NLTE radiative transfer has been given by Schweitzer [1999] and Schweitzer et al. [2000].

3.1 Definition of Super Levels and Super Transitions

Each super level I consists of a set of actual levels $i \in I$. Different super levels I,J do not overlap, so that each level is a subset of exactly one super level:

$$I \cap J = \{\} \tag{3.1}$$

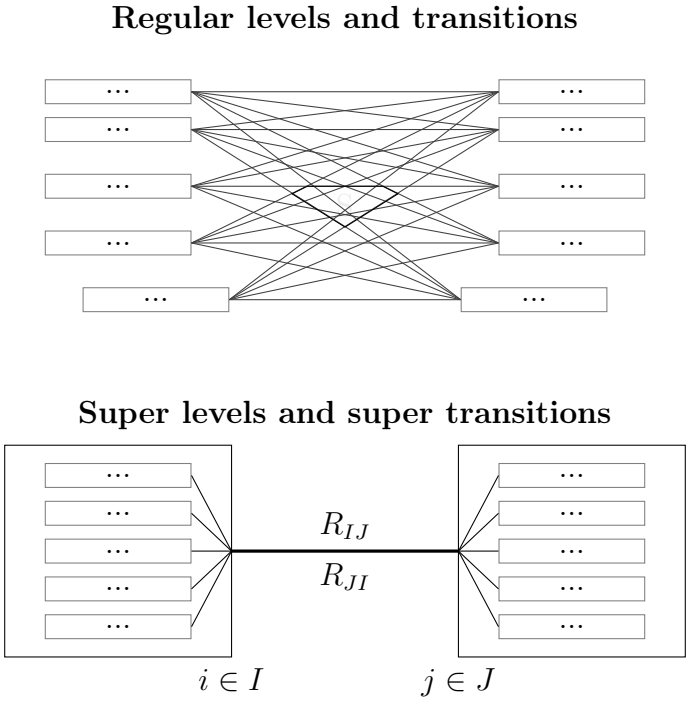

Figure 3.1: Definition: Super levels and super transitions. 10 actual levels i, j in the upper level scheme are combined into 2 super levels I, J linked by one transition with absorption rate R_{IJ} and emission rate R_{JI}. Transitions within the super levels have been omitted for enhanced legibility.

The total occupation number of a super level is the sum of the occupation numbers of all included levels:

$$n_I = \sum_{i \in I} n_i \tag{3.2}$$

Of course, the sum of all occupation numbers of all super levels plus the occupation numbers of all levels not part of a super level has to be the total occupation number of the entire molecule:

$$n_{\text{total}} = \sum_{I} n_I + \sum_{i \notin I} n_i \tag{3.3}$$

To estimate individual occupation numbers of the actual levels, we assume LTE for all levels of a super level, and distribute the super level occupation number n_I according to Boltzmann statistics over all levels within the super level:

$$n_i = \frac{1}{Z_I} \cdot g_i \exp\left(-\frac{E_i}{k_b T}\right) \cdot n_I \tag{3.4}$$

with Z_I as the *super level partition function* for super level I, which is defined as:

$$Z_I = \sum_{i \in I} g_i \cdot \exp\left(-\frac{E_i}{k_b T}\right) \tag{3.5}$$

Assuming LTE within all super levels is the most important approximation of the super level algorithm. It reduces the computational effort at the cost of accuracy of the solution. The better this assumption is for a given set of super levels, the closer the results will be to full NLTE. In this way, finding the right super level definition for a given molecule and problem becomes the most important task for implementing the super level algorithm.

By our definition, all levels of a super level share the same departure coefficient as introduced in Eq. 2.42. Thus, it suffices to define a general departure coefficient b_I, for the entire super level:

$$\frac{n_I}{n_I^*} = b_I = b_i = \frac{n_i}{n_i^*} \qquad \forall\ i \in I \tag{3.6}$$

where n_I^* is the LTE occupation number for super level I, which can is calculated as

$$n_I^* = n_{\text{total}} \frac{Z_I}{Q_{\text{NLTE}}} \tag{3.7}$$

using the non-LTE partition function

$$Q_{\text{NLTE}} \equiv \sum_I b_I Z_I + \underbrace{\sum_{i \notin I} b_i g_i \exp\left(-\frac{E_i}{k_b T}\right)}_{\text{Levels not in a super level}} = \sum_{i=0}^{\infty} b_i g_i \exp\left(-\frac{E_i}{k_b T}\right) \tag{3.8}$$

The super level LTE occupation numbers adhere to the Boltzmann relation for normal levels $\frac{n_i^*}{n_j^*} = \frac{g_i}{g_j} \exp\left(-\Delta E_{ij}/k_b T\right)$ which can, in this case, be rewritten to

$$\frac{n_I^*}{n_J^*} = \frac{Z_I}{Z_J} \tag{3.9}$$

On one hand, transitions between individual levels $i \to j$ can take place between two different super levels:

$$i \in I, j \in J, I \neq J \tag{3.10}$$

In this case, we can define a super transition between I and J, which contains all transitions between individual levels of both super levels. Super transitions have a complicated super line profile, which is the sum of all individual line profiles that are contained within:

$$\phi_{IJ}(\lambda) = \sum_{i \in I} \sum_{j \in J} \frac{g_i}{Z_i} \phi_{ij}(\lambda) \cdot \exp\left(-\frac{E_i}{k_b T}\right) \tag{3.11}$$

The other case is that the transition $j_1 \to j_2$ is coupled to two levels of the same super level:

$$j_1, j_2 \in J \tag{3.12}$$

Such a transition is of course not part of any super transition. It is, essentially, treated as taking place in internal LTE. Super level internal transitions contribute to opacity χ_λ

and emissivity η_λ, but not to the radiative rates R_{IJ}, R_{JI} of any super level. Avoiding that strong lines are left out in this way is one of the constraints for the distribution of levels into super levels (see chapter 3.6).

Figure 3.1 shows a simplified scheme of the relation between levels, super levels, transitions and super transitions. In this simple example, 10 regular levels are split into two super levels of five levels each, with just one super transition between the two super levels replacing all 25 transitions between the actual levels of both super levels.

3.2 Bound-Bound Transitions

The radiative rates for bound-bound transitions introduced in Eqs. 2.22 and 2.24 can now be written for each super transition between two super levels I and J by summation over all existing transitions between all levels of both super levels. For absorption this leads to

$$\begin{aligned} R_{IJ} &= \sum_{i\in I}\sum_{j\in J} \frac{g_i}{Z_i} R_{ij} \cdot \exp\left(-\frac{E_i}{k_b T}\right) \\ &= \sum_{i\in I}\sum_{j\in J} \frac{4\pi}{hc} \int_0^\infty \frac{g_i}{Z_i} \alpha_{ij} \exp\left(-\frac{E_i}{k_b T}\right) J_\lambda(\lambda)\lambda d\lambda \\ &= \frac{4\pi}{hc} \int_0^\infty \sum_{i\in I}\sum_{j\in J} \frac{g_i}{Z_i} \alpha_{ij} \exp\left(-\frac{E_i}{k_b T}\right) J_\lambda(\lambda)\lambda d\lambda \\ &= \frac{4\pi}{hc} \int_0^\infty \alpha_{IJ} J_\lambda(\lambda)\lambda d\lambda \end{aligned} \tag{3.13}$$

where we used the newly defined super level cross-section

$$\alpha_{IJ} = \sum_{i\in I}\sum_{j\in J} \frac{g_i}{Z_i} \alpha_{ij} \exp\left(-\frac{E_i}{k_b T}\right) \tag{3.14}$$

to write R_{IJ} in a similar form to the regular level rate that was shown in Eq. 2.22.

For emission, with radiative rates R_{ji}, the super transition radiative rate is

$$\begin{aligned} R_{JI} &= \sum_{i\in I}\sum_{j\in J} \frac{g_i}{Z_i} R_{ji} \cdot \exp\left(-\frac{E_i}{k_b T}\right) \\ &= \frac{4\pi}{hc} \int_0^\infty \sum_{i\in I}\sum_{j\in J} \frac{g_i}{Z_i} \cdot \alpha_{ji} \left(\frac{2hc^2}{\lambda^5} + J_\lambda(\lambda)\right) \exp\left(-\frac{hc}{\lambda k_b T}\right) \exp\left(-\frac{E_i}{k_b T}\right) \lambda d\lambda \\ &= \frac{4\pi}{hc} \int_0^\infty \alpha_{JI} \left(\frac{2hc^2}{\lambda^5} + J_\lambda(\lambda)\right) \cdot \exp\left(-\frac{hc}{\lambda k_b T}\right) \lambda d\lambda \end{aligned} \tag{3.15}$$

The radiative rate operators that were introduced in Eqs. 2.35 and 2.36 are constructed in the same way as before. Both operators depend on the $\Psi(\lambda)$ and the $E(\lambda)$ operators, which fortunately do not depend on the super level distribution since the treatment of opacity χ, emissivity η and the definition of the Λ operator have not changed.

The population density operator $[n]$ can now be used to retrieve super level occupation numbers. This results in the super level rate operators:

$$[R_{IJ}]\,[n] = \frac{4\pi}{hc}\left[\int_0^\infty \alpha_{IJ}(\lambda)\Psi(\lambda)\,[E(\lambda)]\,\lambda \mathrm{d}\lambda\right][n] \tag{3.16}$$

$$[R_{JI}]\,[n] = \frac{4\pi}{hc}\int_0^\infty \alpha_{JI}(\lambda)\left\{\frac{2hc^2}{\lambda^5} + \Psi(\lambda)\,[E(\lambda)]\,[n]\right\}\exp\left(-\frac{hc}{k_bT\lambda}\right)\lambda \mathrm{d}\lambda \tag{3.17}$$

3.3 Collisional Rates

The rates for collisional excitation and de-excitation introduced in chapter 2.2.2 are combined into collisional rates for super levels in the same fashion as the radiative rates:

$$C_{IJ} = \sum_{i\in I}\sum_{j\in J}\frac{g_i}{Z_i}C_{ij}\cdot\exp\left(-\frac{E_i}{k_bT}\right) \tag{3.18}$$

$$C_{JI} = \sum_{i\in I}\sum_{j\in J}\frac{g_i}{Z_i}C_{ji}\cdot\exp\left(-\frac{E_i}{k_bT}\right) \tag{3.19}$$

$$\tag{3.20}$$

using equation 3.9, this leads to:

$$\frac{C_{IJ}}{C_{JI}} = \frac{Z_J}{Z_I} = \frac{n_J^*}{n_I^*} \tag{3.21}$$

Since the collisional rates only depend on temperature, pressure and electron density, and are not wavelength dependent, calculating them is inexpensive compared to the radiative rates, as long as the individual rates C_{ij} are known.

To be able to compare our results to the results of the existing 1D implementation of the super level algorithm, this work makes use of the empirical formula for atomic collisions given by Allen [1973].

3.4 Bound-Free Transitions

In general, the super level algorithm handles bound-free-transitions the same way as bound-bound transitions, so that the radiative rates for photo-ionization and recombination can be written as

$$R_{Ic} = \frac{4\pi}{hc}\int_0^\infty \alpha_{Ic}J_\lambda(\lambda)\lambda d\lambda \tag{3.22}$$

$$R_{cI} = \frac{4\pi}{hc}\int_0^\infty \alpha_{cI}\left(\frac{2hc^2}{\lambda^5} + J_\lambda(\lambda)\right)\exp\left(-\frac{hc}{\lambda k_bT}\right)\lambda d\lambda \tag{3.23}$$

with

$$\alpha_{Ic} = \sum_{i \in I} \alpha_{ic} \frac{g_i}{Z_I} \exp\left(-\frac{E_i}{k_b T}\right) \tag{3.24}$$

$$\alpha_{cI} = \sum_{i \in I} \alpha_{ci} \frac{g_i}{Z_I} \exp\left(-\frac{E_i}{k_b T}\right) \tag{3.25}$$

The same is true for collisional ionization and recombination:

$$C_{Ic} = \sum_{i \in I} \frac{g_i}{Z_i} C_{ic} \cdot \exp\left(-\frac{E_i}{k_b T}\right) \tag{3.26}$$

$$C_{cI} = \sum_{i \in I} \frac{g_i}{Z_i} C_{ci} \cdot \exp\left(-\frac{E_i}{k_b T}\right) \tag{3.27}$$

In the case of CO, the ionization energy for the first ionization stage $E_{\text{ion}} \simeq 14\text{eV}$ is larger than the dissociation energy for the molecule $D_0 \simeq 11\text{eV}$ (see e.g. Allen [1973]). For this reason, CO will dissociate soon after it is ionized, depending on the life times on the actual molecular states involved. This would make it necessary to treat dissociation, as well as ionization and, thus, in Non-Local Chemical Equilibrium *NLCE*. However, our equation of state solver assumes chemical equilibrium and can not treat photo-dissociation. We have included a CO+ ground state to allow for ionization, but at least in the models used in this work, it is generally almost unpopulated. Collisional ionization of CO is possible. Unfortunately, there were no cross-sections for the relevant wide temperature and pressure ranges available. Thus, they were assumed to be very small.

3.5 Solving the NLTE Problem for CO

The rates have been brought into a form that is equivalent to the radiative rates for actual levels. Thus, it is possible, to solve the rate equations in the same way, as one would for the actual levels.

Equation 2.41 can be rewritten for the super level algorithm by replacing all original rate operators by the operators for the super transitions and all corresponding occupation numbers by the super level occupation numbers, leading to the following set of equations for all super levels I:

$$\begin{aligned}
&\sum_{J<I} n_{J,\text{old}} \left[R^*_{JI}\right] \left[n_{\text{new}}\right] - n_{I,\text{old}} \left\{ \sum_{J<I} \left(\frac{n^*_J}{n^*_I}\right) \left[R^*_{IJ}\right] \left[n_{\text{new}}\right] + \sum_{J>I} \left[R^*_{IJ}\right] \left[n_{\text{new}}\right] \right\} \\
&+ \sum_{J>I} n_{J,\text{old}} \left(\frac{n^*_I}{n^*_J}\right) \left[R^*_{JI}\right] \left[n_{\text{new}}\right] + \sum_{J<I} n_{J,\text{new}} \left(\left[R^*_{\Delta JI}\right] \left[n_{\text{old}}\right] + C_{JI}\right) \\
&- n_{I,\text{new}} \left\{ \sum_{J<I} \left(\frac{n^*_J}{n^*_I}\right) \left(\left[\Delta R_{IJ}\right] \left[n_{\text{old}}\right] + C_{IJ}\right) + \sum_{J>I} \left(\left[\Delta R_{IJ}\right] \left[n_{\text{old}}\right] + C_{IJ}\right) \right\} \\
&+ \sum_{J>I} n_{J,\text{new}} \left(\frac{n^*_I}{n^*_J}\right) \left(\left[\Delta R_{JI}\right] \left[n_{\text{old}}\right] + C_{JI}\right) \\
&= 0
\end{aligned} \tag{3.28}$$

which represents a system of N equations with N+1 unknowns for the occupation numbers $n_I, I \in N$ of each super level plus the occupation number n_C of the continuum ground state. In the case of CO, the dependence on the electron density n_e, which is represented in the collisional rate coefficients C_{IJ}, is not an issue for the iterative solution, since the ionization and recombination rates for CO are considered negligible, so that n_c can be treated as constant, thus, removing it as an unknown.

To close this system, we use the fact that the total number of particles is known and conserved:

$$n_C + \sum_{I \in N} n_I = n_{\text{total,CO}} \tag{3.29}$$

From the super level occupation numbers n_I we can obtain the occupation number for each individual level by equation (3.4). The NLTE opacities, which are to be used in the next radiative transfer iteration, are then calculated for each actual level for each wavelength point.

3.6 Super Level Models for CO

So far super levels have been treated as a collection of levels, without giving any explicit detail, how the individual levels of a molecule are combined into super levels.

The arrangement of levels into super levels can, hypothetically, take almost any form. Any number of super levels from 2 to $N-1$, N being the number of actual levels, though using the extreme case is, of course, not very useful. We expect that the higher the number of super levels, the closer the result will be to true NLTE for all levels. It will be necessary to balance computational demands with accuracy. Determining how many super levels are needed to achieve a sufficiently close approximation of full level NLTE is one of the purposes of this work.

As was stated in section 3.1, transitions within a super level are not considered in the radiative transition rates, and, therefore, do not contribute to the NLTE occupation numbers. Opacity and emissivity for these lines are calculated using occupation numbers that only depend on all external lines coupling to the respective super level. This reduces the computational effort, due to the fact that fewer wavelength points are required to sample the super line profiles, but also reduces the accuracy of the solution.

For this reason, the levels within one super level should be strongly coupled. If this is the case, the assumption that the occupation numbers for all levels of a super level can be determined using Boltzmann statistics, as shown in equation 3.4, is sufficiently close to reality.

Each level is defined by a set of quantum numbers or its energy above the ground state. Using the same models as in Schweitzer [1999] and Schweitzer et al. [2000], the levels are sorted into super levels by vibrational quantum number ν, because the strong CO bands contain transitions of $\Delta\nu = \{1, 2\}$ and energy E_i, as actual levels within one super level should be close in excitation energy. Using the same models allows for a direct comparison with the previous results of the 1D code.

All relevant level and line properties, such as excitation energy, quantum numbers, statistical weights, as well as transition wavelength, oscillator strength and coupled levels

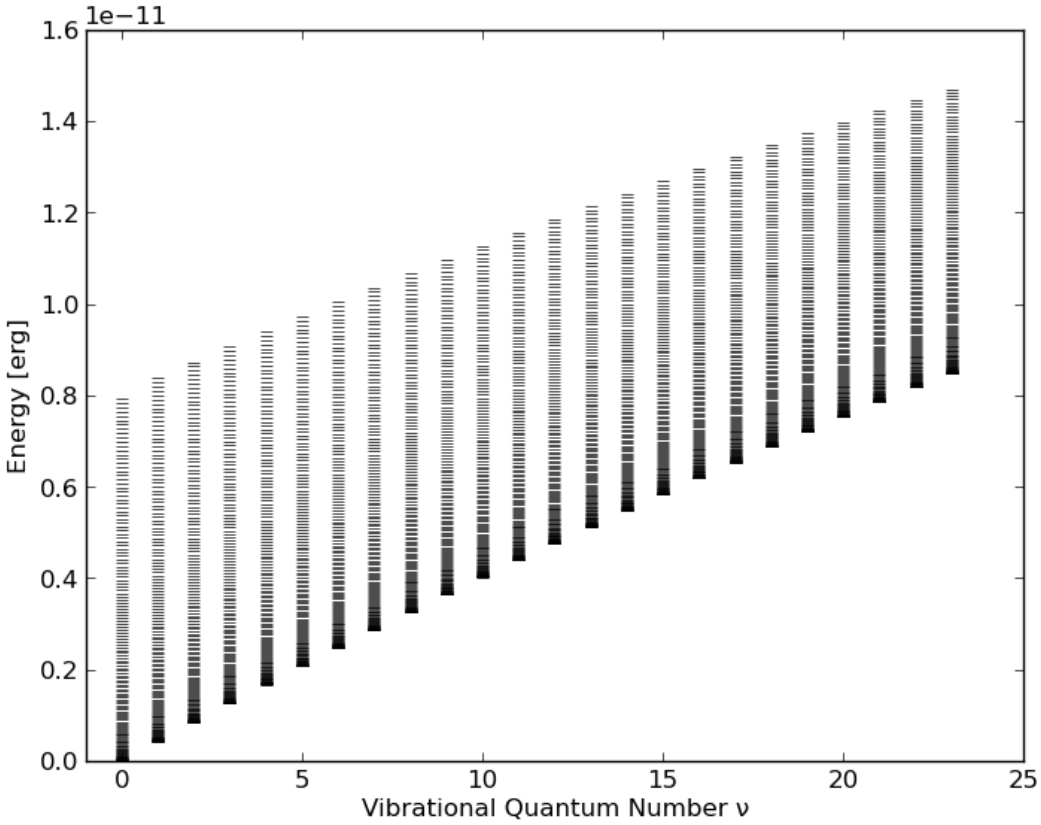

Figure 3.2: Energy level diagram for all levels of $C^{12}O^{16}$, separated by energy E_{level} and vibrational quantum number ν. All transitions have been omitted for legibility.

have been taken from the line lists published by Goorvitch [1994], Goorvitch and Chackerian [1994a,b]. To further reduce the numbers of lines and levels, only $C^{12}O^{16}$ was used, which is the most abundant CO isotope.

3.6.1 Super Levels by vibrational Quantum Number

This model can be deduced from Figure 3.2, which shows energy above ground-state and vibrational quantum number ν for all known levels of $C^{12}O^{16}$. In this model, each super level consists of all levels that share the same vibrational quantum number ν, represented by one vertical ladder of levels in the plot. This model corresponds to vibrational LTE models as used by, e.g., Kutepov et al. [1991]. It incorporates the fact that radiative transitions between levels with the same vibrational quantum number have very long lifetimes and that strong transitions for CO are usually found with $\Delta\nu = 1$ or $\Delta\nu = 2$.

Splitting by vibrational quantum number produces 24 super levels from 3623 levels for $\nu \in [0, 23]$ linked by 63 super transitions for 18837 actual transitions. 366 of these transitions are located between levels of the same super level and are, therefore, not included in any super transition. Opacity and emissivity for these transitions are obtained using occupation numbers obtained by vibrational LTE within the respecitve super levels.

This is a simple alternative of splitting the CO levels into super levels. However, as

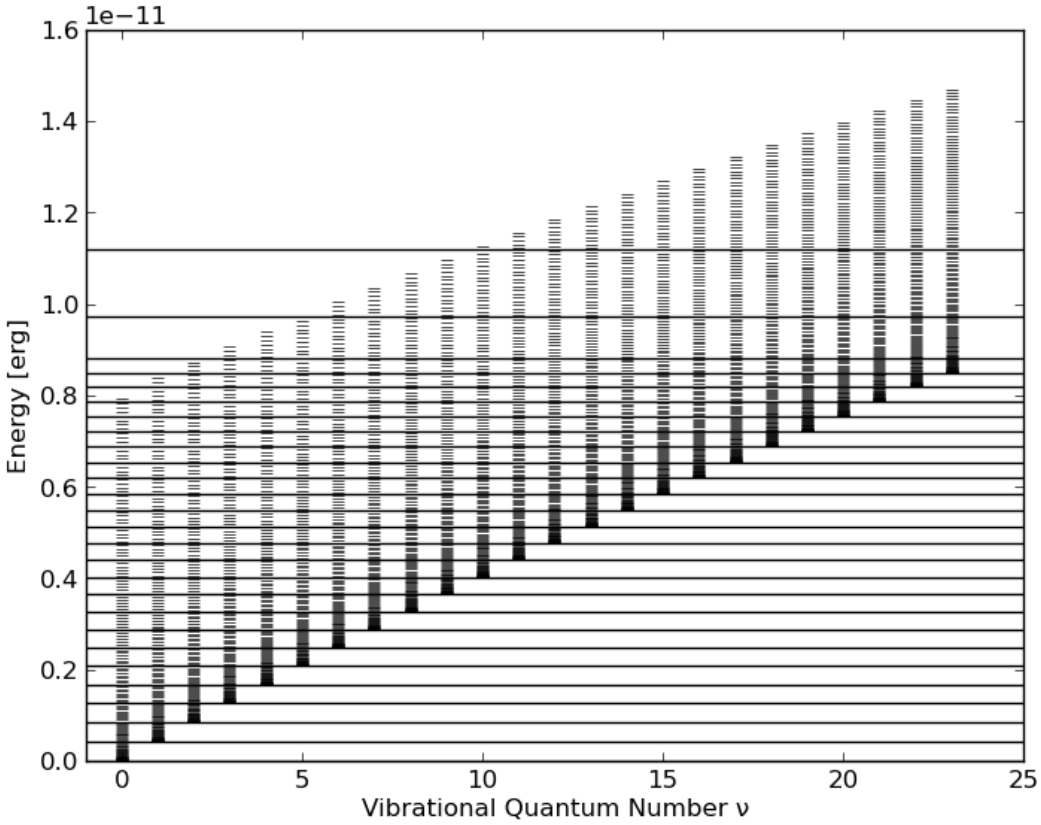

Figure 3.3: Energy level diagram for all levels of $C^{12}O^{16}$, separated by energy E_{level} and vibrational quantum number ν. Super level divisors are indicated by horizontal lines.

can be seen in Figure 3.2 the individual superlevels strongly overlap in energy, which might lead to problems, even if the number of transitions that can not be included into super transitions is small.

3.6.2 Super Levels by Energy

The second model distributes the levels not by vibrational quantum number, but by level energy E_i. Levels of similar energy above ground-state are combined in the same super level. This can be seen in Figure 3.3 where the super levels are separated by the added horizontal lines. In this model, the energy of the lowest level of each set of levels sharing the same vibrational quantum number was used to divide the levels in energy. In this way, each super level is still dominated by one vibrational state, as the levels of lowest energy of one vibrational state usually are higher populated than the upper levels of another vibrational state.

The advantage of this method is that all levels within one super level are close in level energy. On the other hand, the levels are not as strongly coupled, as in the first model, since an influence of other vibrational states is possible, even if it is small.

Using only the vibrational ground states as a boundary would produce a super level with a very high number of levels for the super level containing the levels of highest

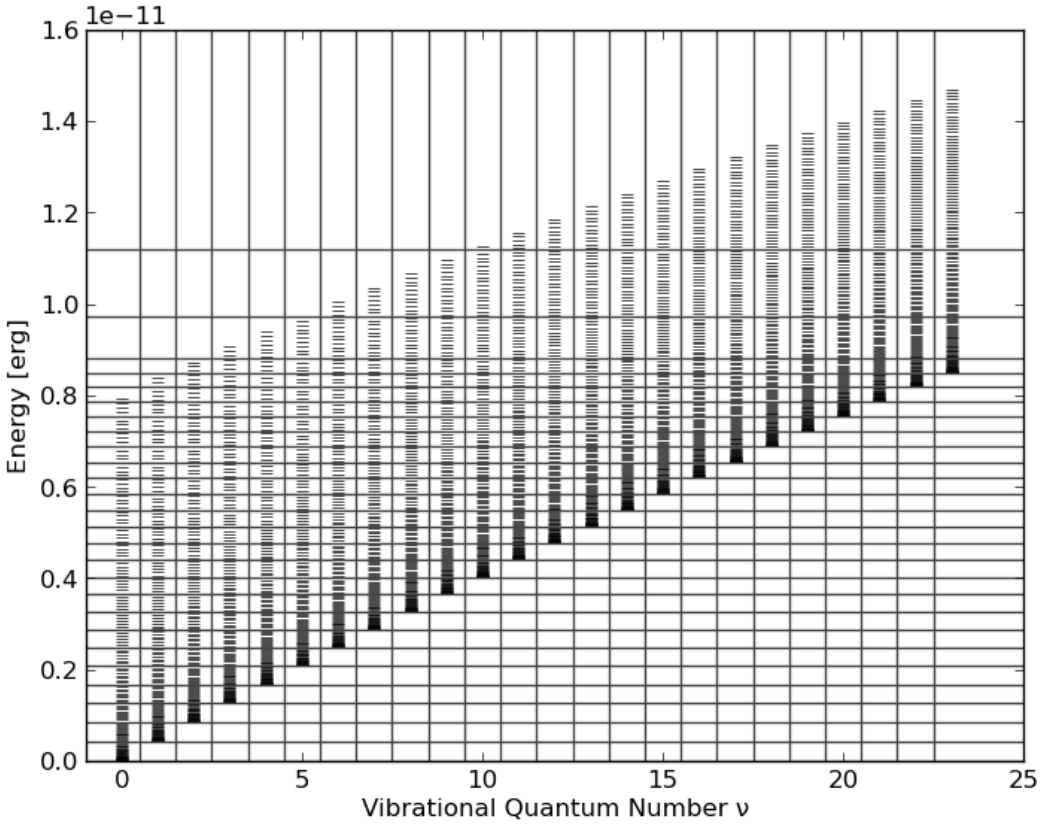

Figure 3.4: Energy level diagram for all levels of $C^{12}O^{16}$, separated by energy E_{level} and vibrational quantum number ν. Super levels boundaries are indicated by horizontal and vertical lines.

energy. For this reason, this level was split to construct super levels with a roughly constant number of levels.

This model uses 27 superlevels linked by 93 super transitions. Due to the way it has been set up, 3324 of the 18837 transitions in the line list are part of the same super level, which at the same time reduces the computational effort but might also reduce accuracy.

3.6.3 Super Levels by Energy and Quantum Number

The third method combines the aforementioned division by energy E_{level} and vibrational quantum number ν, using both criteria. This model benefits from the advantages of both prior models. All levels within each super level are strongly linked since they belong the the same vibrational state, and the energetic overlap between the superlevels is much smaller than in the first model.

This kind of model is visualized in Figure 3.4 - each cell of the shown grid is one super level. Of course, only superlevels containing any actual levels are incorporated into the model. This leads to 350 superlevels with 2388 super transitions, where only 348 transitions are between levels of the same super level.

The downside of this model is the large number of super levels, as well as external

transitions, which require an equally large computational effort to obtain the radiative rates and solve the rate equations and have a greater memory consumption. In this way, it can be treated as an intermediate step between the small-scale super level models and full NLTE.

3.6.4 Real Levels

As a final test, we have set up a model where each super level is populated by exactly one level. Thus, we are actually calculating the real model with 3623 levels and 18837 transitions. This model was used primarily in 1D calculations to compare different super level models against the results of the real calculation. In a 3D calculation this model requires the computational domain to be distributed over a high number of processes as not to exceed the available memory, since storing occupation numbers for 3623 levels and radiative upward and downward rates of more than 18000 transitions, as well as the coefficients of the solution matrix of the equation system for a huge number of voxels is not easily feasible, if at all possible.

Chapter 4

Numerical Implementation and Tests

This chapter describes the implementation of the super level NLTE algorithm into the existing Phoenix/3D general purpose atmosphere code. The implementation is based upon the existing solver for atomic NLTE in Phoenix/1D and Phoenix/3D as described by Hauschildt [1993] and Hauschildt and Baron [2014], as well as the 1D implementation of the super level method for molecular NLTE by Schweitzer [1999] and Schweitzer et al. [2000].

Furthermore, the results of a number of implementation tests that were carried out to ensure the reliability of the new implementation are presented. Each super level definition used was also tested for computational performance both in computation time and memory requirements, as well as convergence behaviour.

4.1 Implementation of Super Levels for Phoenix/3D

A flow chart of the Phoenix/3D atmosphere code including the steps necessary to solve the NLTE problem using the super level algorithm is presented in Figure 4.1. The code uses a predefined hydro structure $(T(x, y, z), p(x, y, z))$ and is capable of handling voxel grids of both, Cartesian, cylindrical and spherical geometries.

The NLTE radiative transfer problem is solved using a *full characteristics method* for the formal solution and operator splitting with a non-local Λ^* operator for the radiative transfer and a diagonal R^* operator for the rate equations. The technical details of the solution implemented in Phoenix/3D are described in detail by Hauschildt and Baron [2006, 2008, 2009, 2010, 2014] and Baron and Hauschildt [2007].

The super level algorithm was tested for the CO molecule, which required the following input data:

- A line list of all CO lines with information on transition wavelength λ_{ij}, Einstein coefficient B_{ij} and upper as well as lower level coupled to the transition.
- A list of all known CO levels including excitation energy E_i and degeneracy g_i.
- A super level definition sorting each known level into a super level as introduced in chapter 3.6.
- A list of super transitions

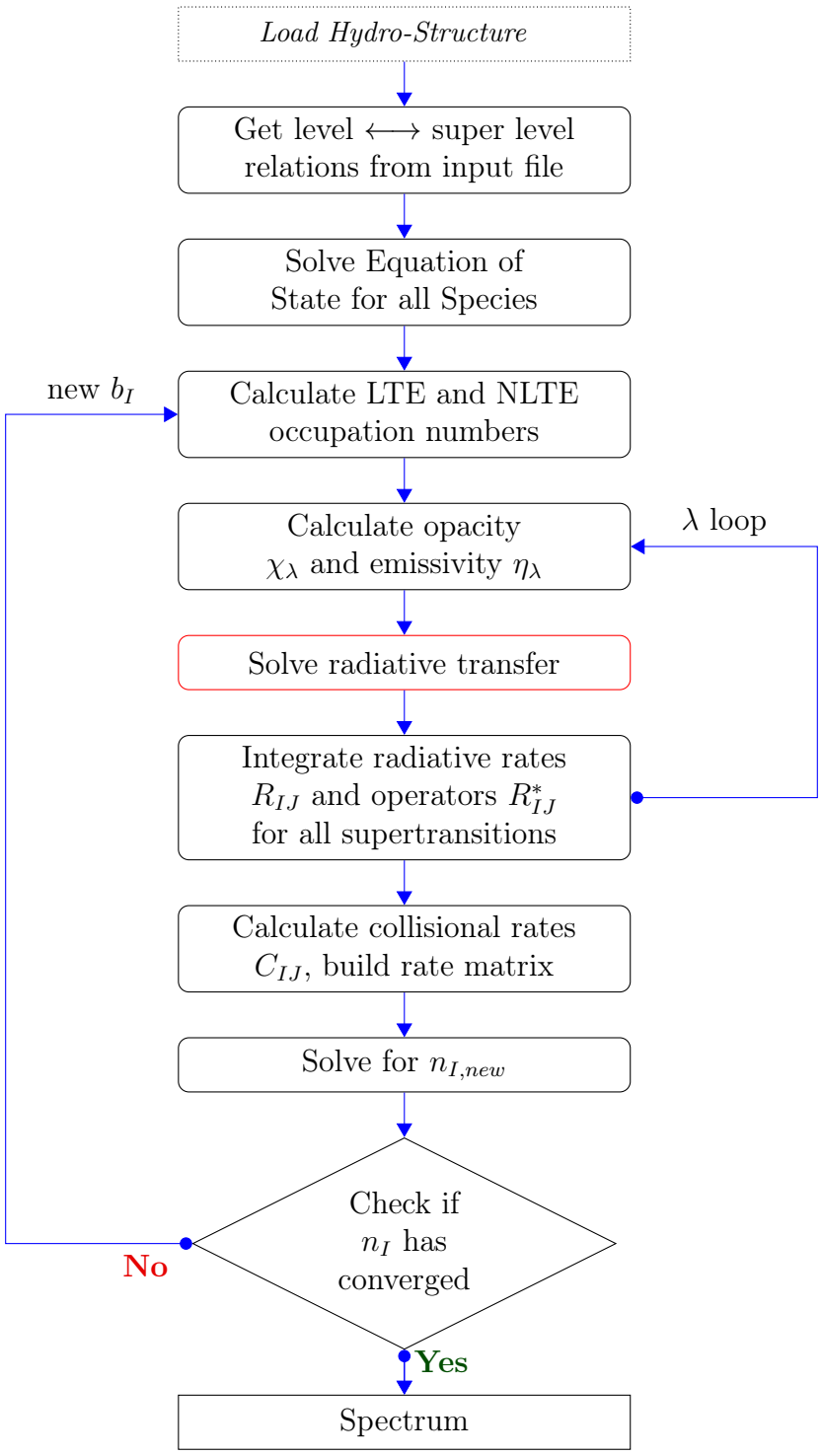

Figure 4.1: Iteration Scheme for the Super level Algorithm as implemented into the PHOENIX/3D atmosphere code. Steps marked in red are non-local and require communication over the full domain - all other steps are done independently for each voxel.

The program uses the super level definition from the input files to assign each actual level in the input level list to a super level and each actual transition between different super levels to a super transition. A system of pointers connects levels to super levels, transitions to super transitions and vice versa. This ensures that loops can be written either for super levels and transitions or for actual levels and transitions while the correct fields are easily accessible at all times.

Since all molecular data and super level and line definition is read from input files, the program can be used for different super level definitions and different molecules without need for a change to the code.

For the first iteration, LTE is assumed to determine the initial occupation numbers for all super levels.

After this initial setup and allocation of all necessary data structures, the opacity is calculated and the radiative transfer problem is solved for each wavelength point separately. The wavelength integrals for the radiative rate operators R_{IJ} and R^*_{IJ} are calculated during this step using J_λ and Λ^* from the RT solution. To reduce memory usage, only wavelength dependent data for the current wavelength point and the resulting rate integrals of each super transition are stored.

Once the wavelength loop is completed, the rate operators and collisional rates are combined into the rate matrix for the system of equations 3.28. This matrix is allocated as an arbitrary-precision floating point number with typically 32 to 62 digits, for an average of 52 digits. The number of digits used in the solution is estimated from the largest and smallest occupation number for each voxels and increased by 24 as a safety margin. Using arbitrary precision is advisable for every calculation that potentially operates on very large numbers with very small numbers to avoid round-of errors.

The matrix is then solved for $[n_{new}]$ using the same arbitrary precision matrix solver as Hauschildt and Baron [2014], from which the new departure coefficients b_I^{new} are computed.

Having completed one iteration, the next iteration is started with the updated occupation numbers. This process is repeated until the desired accuracy for $\Delta n_i/n_i$ or $\Delta b_i/b_i$ is achieved.

Due to the size of 3D calculations and the number of wavelength points required, using just a single process is not feasible for large calculations.

For each voxel, the occupation numbers for all levels n_I, n^*_I, the super line cross-sections α_{IJ}, the upward and downward radiative rates R_{IJ}, R_{JI} and operators R^*_{IJ}, R^*_{JI} for all super transitions, as well as the hydro structure of the grid and general equation of state data need to be stored. For a typical number of voxels in a productive model, the total memory consumption will, therefore, be overwhelmingly high due to the large amount of data that needs to be stored at all times.

Additionally, the radiative transfer problem needs to be solved for a sufficient number of wavelength points and with a sufficiently high number of solid angles to calculate the wavelength integrals in the radiative rate computation correctly, which results in a large computational effort.

For these reasons, both the radiative transfer solution, as well as the NLTE solver, were implemented using a hierarchical domain decomposition method as implemented by

Hauschildt and Baron [2014]. Each individual process is part of a domain decomposition group, where the entire computational domain is split over all processors within the group. Each process within the group, thus, only has to store the data for a subset of the voxel grid, as well as data that needs to be known throughout the group to solve the 3DRT problem for a given wavelength point.

The 3DRT solution is parallelized in solid angle space for each wavelength point. Each domain decomposition group calculates one part of the wavelength grid. In this way, the wavelength integrals are distributed over several domain decomposition groups to reduce the number of wavelength points each process has to calculate. The results of the partial rate integrals are communicated between all computational domains to assemble the full rate integrals.

Due to the way the domain decomposition has been set up, the number of domain decomposition groups is limited by the number of wavelength points in the wavelength grid. The number of processors in each group is limited by the number of voxels. Due to the fact that a high number of wavelength points is required and 3D calculation usually entail a high number of voxels, the calculation can be scaled to use a large number of processors efficiently.

4.2 The Wavelength Integration Problem

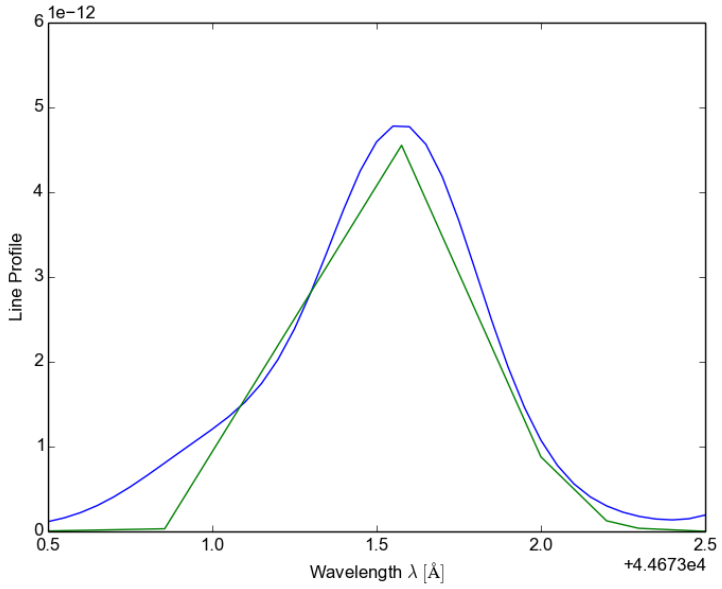

Figure 4.2: Construction of the Wavelength grid. The blue line is the calculated LTE high resolution line profile of a CO line, the green line shows the line profile as constructed by the wavelength grid used for the integration.

The simplest way to evaluate the wavelength integrals in equations 3.13 and 3.15 numerically, would be to sample the entire wavelength space with high resolution. However,

this would require a solution of the radiative transfer problem for an extremely large number of wavelength points, which is not feasible in 3D with currently available hardware. Fortunately, the integrals are in essence of the form

$$\text{const.} \cdot \int_0^\infty \phi(\lambda) J(\lambda) d\lambda \tag{4.1}$$

with $\phi(\lambda) = 0$ for all wavelengths points that are not close to a CO line that contributes to any super line profile. Thus, it is sufficient, to sample the line profiles of all CO lines with a high enough resolution to calculate the integral. This reduces the number of wavelength points compared to a full sampling of the entire wavelength space. Unfortunately, molecules tend to have a high number of lines, so that even only considering points close to the lines, the number of wavelength points will still remain high.

4.2.1 The Minimum Number of Wavelength Points

In this work, the line profiles of all CO lines have been approximated by a Gaussian, which is a reasonable assumption for the narrow lines within the $\Delta\nu = \{1, 2\}$ bands at least in regions of low pressure. To keep the number of wavelength points small and reduce the computational demands of the calculations, the Gaussian was approximated by only three points. In this way, both line depth, as well as line width were sampled for each line. This results in one wavelength point at the transition wavelength λ_{ij} and two wavelength points at the rims of the line for each transition. The bordering points were set up, to approximate the Gaussian function by a triangle as well as possible. This method was previously used in the 1D incarnation of the code [Schweitzer, 1999]. Figure 4.2 visualizes how each line was sampled to create this grid. Some additional wavelength points were added to account for strong lines and to better sample the continuum.

Currently the line list that is being used considers 18837 CO lines. This means that any calculation will require at least $\approx$ 60000 wavelength points for the bound-bound transitions of CO alone. This number can not be reduced by the super level algorithm, thus, it represents the minimum computational effort that will be required. The number of necessary wavelength point can change slightly, since some lines are super level internal and, thus, not included into the rate integrals. The number is increased by wavelength points necessary to sample the continua and possible lines of other species, if any are included.

At the moment, calculating a large number of wavelength points is computationally expensive but still feasible, even if barely so. For this reason, we chose not to introduce an additional approximation and retain the code's general flexibility and the benefits of direct opacity sampling.

A method to reduce the number of necessary wavelength points by using opacity distribution functions is described, e.g., by Anderson [1989]. For more complex molecules with an even higher number of lines, and aiming for direct application, the issue may have to be revisited.

4.2.2 First Order Correction using Planck Rates

With three wavelength points per line, the wavelength integrals will show errors due to the approximation of the line profiles. Even carefully selected wavelength points can only reduce but not eliminate these errors.

For this reason, a first order error correction was implemented following [Schweitzer, 1999]. This was done by calculating the radiative rates $\widehat{R}_{IJ}$ for a case of $J = B$. Assuming that the Planck function does not vary notably over the width of a line the Planck function $B(\lambda)$ can be approximated as constant, so that the wavelength integral can be evaluated analytically with $B(\lambda) = B(\lambda_{ij})$:

$$\widehat{R}_{IJ} = \int_0^\infty \sum_{i\in I}\sum_{j\in J} \frac{g_i}{Z_I} \exp\left(-\frac{E_i}{k_b T}\right) \frac{\lambda_{ij}^2 B_{ij}}{c} \phi_{ij} B(\lambda_{ij}) d\lambda \tag{4.2}$$

$$= \sum_{i\in I}\sum_{j\in J} \frac{g_i}{Z_I} \exp\left(-\frac{E_i}{k_b T}\right) \frac{\lambda_{ij}^2 B_i j}{c} B(\lambda_{ij}) \int_0^\infty \phi_{ij} d\lambda$$

$$= \sum_{i\in I}\sum_{j\in J} \frac{g_i}{Z_I} \exp\left(-\frac{E_i}{k_b T}\right) \frac{\lambda_{ij}^2 B_i j}{c} B(\lambda_{ij}) \equiv \widetilde{R}_{IJ} \tag{4.3}$$

The line profile ϕ_{ij} is normalized, so that the integral returns 1 in this case. For narrow lines, like most of the lines of CO in this case, the assumption is good enough.

The analytical result of equation 4.3, which is calculated a priori, is then compared to the numerically obtained integral resulting from equation 4.2. The numerical integral is evaluated on the same wavelength grid, so that the ratio of

$$\frac{\widehat{R}_{IJ}}{\widetilde{R}_{IJ}} \tag{4.4}$$

can be used to account for the error introduced by the numerical integration.

4.3 Tests of the Algorithm

The implementation of the super level algorithm and the stability of the solver was tested with a series of standard scenarios. These tests were setup in such a way that LTE should be restored in every test. Therefore, the departure coefficients and opacities could be tested against LTE conditions.

- If all departure coefficients are fixed to $b_I = b_i = 1.0$ and, therefore, according to equation 2.42 LTE occupation number $n_i = n_i^*$ apply for all levels, the opacity for each level must be identical to the LTE opacities. This is a test for the opacity and line profile calculations.

- If the atmosphere is dominated by collisional excitation and all radiative rates are zero ($C_{IJ} \neq 0 \bigwedge R_{IJ} = 0$) then LTE is the exact solution, and the solver should return $b_I = 1$ for all super levels. This is a test for the implementation of the collisional rates as well as the matrix solver.

- If the mean intensity in each voxel is exactly the Planck function ($J = B$), then LTE should be restored as well. The solver should return $b_I = 1$ for all super levels, as in the second test.

All three tests can be easily implemented by fixing b_I, R_{IJ} or $J(\lambda)$ to the necessary values. Due to the fact that the radiative rates are either calculated without respect for the opacities or even ignored all-together, the tests can be executed without need for more than one iteration.

4.3.1 Opacities for $b_I = 1.0$

While this test might seem trivial, any error in the opacities would have influenced the radiative transfer calculation and, henceforth, produced wrong radiative rates.

Results from the test showed that the LTE opacities are reproduced for all CO lines with an acuracy of 10^{-16}, so that we can expect a correct solution for the radiative transfer problem, at least as far as the opacities are concerned.

4.3.2 Solver Test without Radiative Rates

This test was done for a model with $T_{\text{eff}} = 2700\text{K}$ and $\log g = 5.0$. The super level setup used was the Head Energy method (see chapter 3.6.2). One iteration step was calculated, while only the collisional rate coefficients were fed into the rate matrix.

This test resulted in departure coefficients of $b_I = 1.0$ with full double precision accuracy for all super levels and, therefore, a restoration of LTE conditions as in $n_I = n_I^*$, which shows that the collisional rates were calculated correctly.

The same test was then repeated for the other super level definitions to ensure that the solver works correctly in all cases, which turned out to be the case.

4.3.3 Radiative Rates Test with $J = B$

Using the same test conditions as before, the radiative rate coefficients were now calculated using $J = B$, while the collisional rate coefficients C_{IJ} where omitted from the rate matrix.

Results of this test showed departure coefficients of $b_I = 1.0$ with full double precision accuracy for all super levels. The other two super level definitions produced similar results, confirming that the solver is working independent of the super level setup used.

This confirms that the rate integration, as well as the insertion of the radiative rates into the matrix are working properly. Thus, the solver has passed all standard tests.

4.4 Computational Demands

The super level algorithm was implemented to reduce the computational demands while solving the 3D NLTE problem for molecules. Several super level models have been set up with different numbers of super levels with different trade-offs between computational demands and accuracy.

To compare the different super level definitions described in section 3.6 with respect to their memory usage and computation time, we have used the same spherically symmetric test model with $T_{\text{eff}} = 2700K, \log g = 5.0$ and $(65 \times 33 \times 33) = 70785$ voxels. All

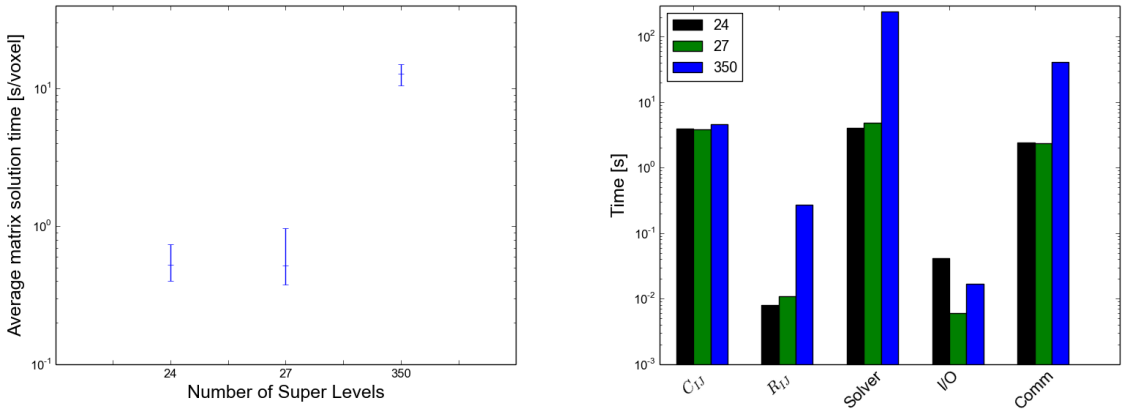

(a) Average time to solve matrix

(b) Total time

Figure 4.3: Timing for all three super level models with 24, 27 and 350 super levels. Shown are average solver times as well as total time for the different parts of the solution for an entire domain decomposition group.

calculations were carried out on a CRAY XE 30 supercomputer with 6144 processes on 256 computation nodes with 24 Intel Xeon Ivy Bridge cores at 2.4 GHz each. Each node has a memory of 64 GB (2.66 GB/core). Each domain decomposition group consisted of 48 processes for a total of 128 dd-groups.

Figure 4.3a shows the total time needed to solve the statistical equations for a single voxel for all three respective models. The average solution time for a randomly selected sample of 480 voxels as well as the highest and lowest solution time for a single voxel is shown.

In Figure 4.3b, the total times for the different tasks in an entire domain decomposition group are shown. This includes calculating the collisional rates C_{IJ} and inserting them into the rate matrix, inserting the radiative rates R_{IJ} and rate operators R^*_{IJ} into the rate matrix, the actual solution of the rate matrix as well as disk I/O and MPI communication time. As expected, the model with 350 super levels required more computation time, especially for the solution of the rate equations. Just building the matrix takes up more time as well, but compared to the solution time itself the time needed to build the matrix is insignificant.

However, solving the rate matrix, once the radiative rates have been obtained, still only takes up a fraction of the total time for the entire solution. Figure 4.4a shows the different components of the entire calculation for the different models. Since a direct comparison of the different calculations would be biased by the fact that slightly different wavelength grids were used to represent lines that are or are not super level internal, only relative times compared to the total time of each calculation are shown. Looking at the 24 and 27 super level models, the solution of the NLTE rate equations takes up only about 1% of the total calculation time, while the radiative transfer solution for more than 80000 wavelength points takes up the bulk of the computation time.

Using 350 super levels, the ratio of NLTE rate equation solver time to radiative transfer solution time is about 10%. In large calculations, this might already pose a constraint on

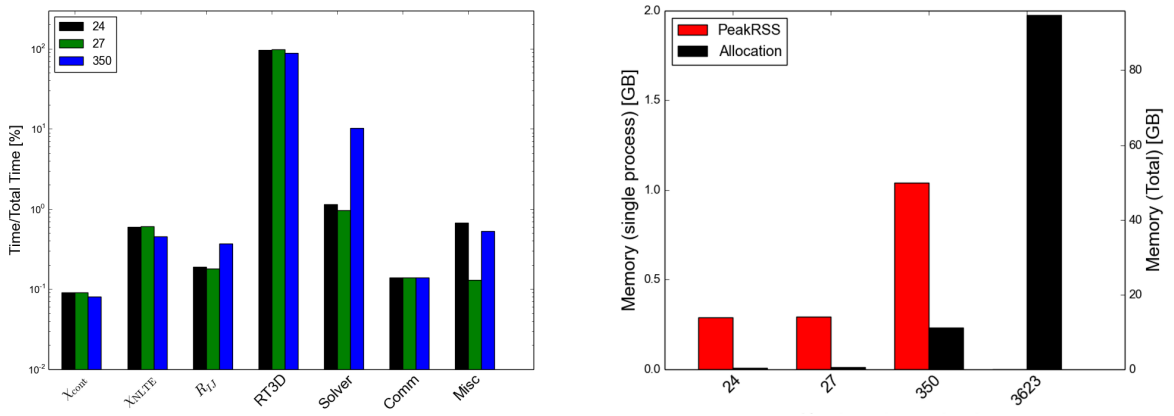

(a) Relative Calculation Time

(b) Memory Consumption

Figure 4.4: Timing and memory consumption for all three super level models with 24, 27 and 350 super levels. The memory consumption of a full-NLTE model (3623 levels) is shown for comparison of the allocated memory size, unfortunately the model exceeded the available memory, so that no comparison in timing or Peak RSS was possible.

using models like this, while it is feasible for small computational grids. In the end, it remains a trade off between accuracy and computational demands.

The memory requirements for the different models are presented in Figure 4.4b. The total size of all NLTE arrays, including radiative upward and downward rates and operators for lines and continua, super level occupation numbers and LTE occupation numbers, departure coefficients, super line cross-sections, normalization factors, Planck-rates, NLTE-opacity, NLTE-emissivity and super level partition functions, as well as the peak resident set size (RSS) of each process are shown. The right hand axis has been rescaled to show the single process memory consumption, while the left hand axis shows the real memory consumption while using domain decomposition.

Full NLTE The memory requirements of the full NLTE calculation with 3623 levels are shown for comparison. However, using the same setup as for the super level models, the calculation exceeded the memory limits of the computation nodes when calling the NLTE solver and was aborted. The peak RSS before the NLTE solver was 2.18 GB per node. Unfortunately, the solver has to allocate a solution matrix with a rank equal to the number of levels plus one. In the full NLTE case, the matrix has, thus, a size of $3624 \times 3624 = 13,133,376$, each requiring the allocation of a multi-precision (hereafter: mp) floating point number. Every mp-floating point number is, in fact, stored as an array of double precision floating point numbers (see, e.g., Bailey et al. [2002]), so that the mp-matrix alone exceeds the memory available on the computation nodes used. It was possible to solve this matrix in the 1D code, due to the fact that it uses only a double precision matrix, and the calculation was run on an pSeries 690 IBM AIX with 32 processors and 256 GB of total memory but less overall computation power.

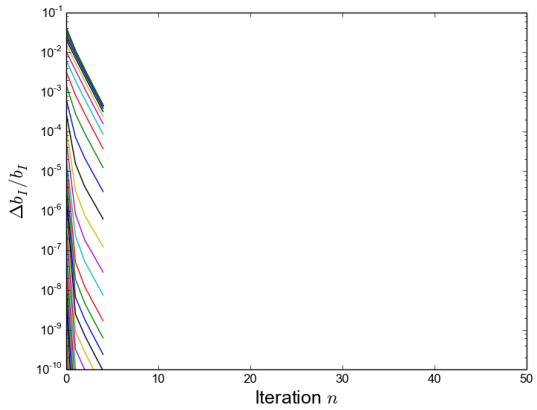

(a) 3D Quantum Model

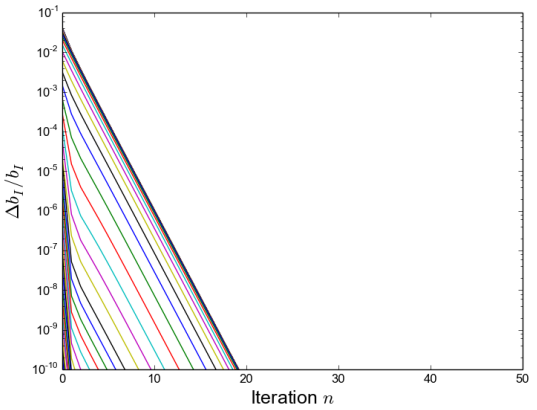

(b) 1D Quantum Model

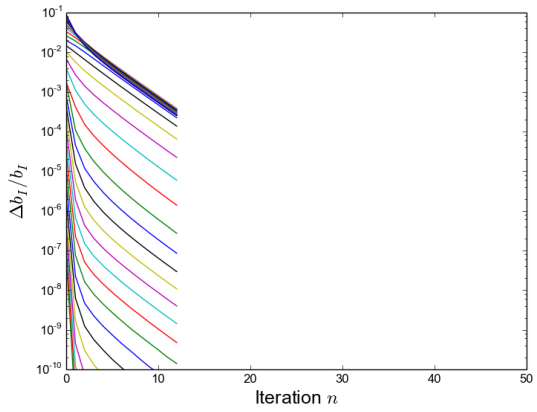

(c) 3D Head-Energy Model

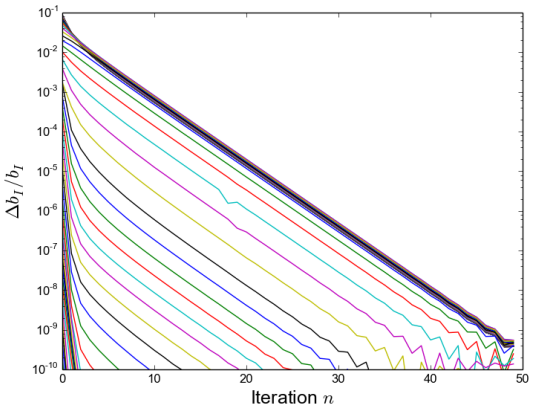

(d) 1D Head-Energy Model

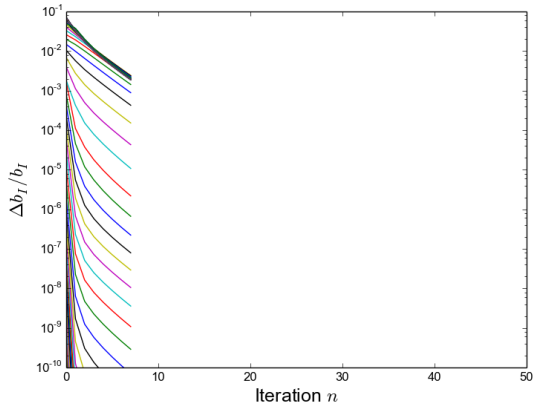

(e) 3D Energy and Quantum Model

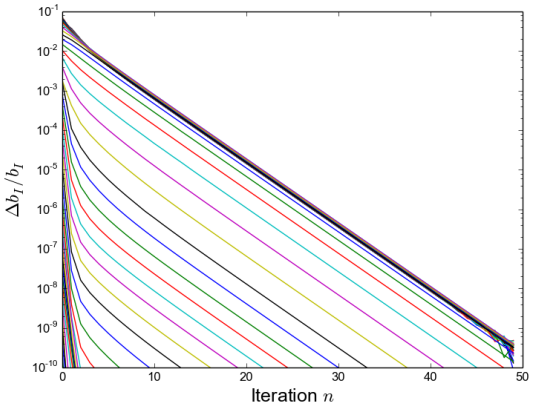

(f) 1D Energy and Quantum Model

Figure 4.5: Convergence Rates for all three super level models in 3D and 1D. Shown is $\Delta b_I^{(n,n+1)}/b_I^{(n)}$ for each iteration for the highest populated super level, usually the one containing the ground state. Each line represents a different voxel.

4.5 Convergence

4.5.1 Spherical Symmetric 3D Model

To test the convergence of each model, we have compared the relative change to the departure coefficients after each iteration between different models and to the respective 1D models. Since each iteration step is computationally expensive, the 3D models have only been converged to a point where it was possible to compare the results and the convergence rate to the 1D results.

Figure 4.5 presents the resulting convergence rates for the most highly populated super level of each model and all voxels in the computational domain, as well as the same convergence rates for each layer in the 1D code. The plots have been cut off at 10^{-10} due to the fact that this is the maximum precision of the 1D results which are limited by using double precision and ascii I/O.

The 3D models seem to reproduce the convergence behaviour that can be seen in the 1D models. Furthermore, the convergence rates show that the Quantum Number model converges notably faster than the other two models. The $\Delta b_I^{(n,+1)}/b_I^{(n)}$ of this model shrinks exponentially with each iteration, and the model converges up to an accuracy of 10^{-10} in only 20 iterations, while the other two models require 50 or more. However, the number of super levels seems to have no direct influence on the convergence rate for the latter two models, since the 27 super level model shows roughly the same convergence rate as the 350 super level model.

In this way, the Quantum Number model shows a much better computational performance due to a faster overall convergence time. The reason for this can be found in the accuracy of the model, which will be discussed in detail in chapter 5.1.

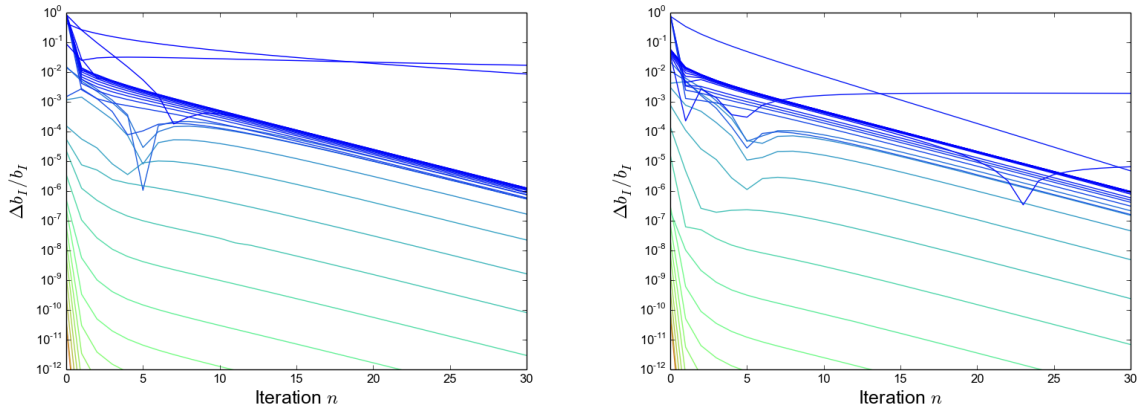

(a) Model A

(b) Model B

Figure 4.6: Convergence Rates for two different parametrized 3D models. $\Delta b_I^{(n,n+1)}/b_I^{(n)}$ for each iteration for the highest populated super level is shown, usually the one containing the ground state. Each line represents a different voxel and is color coded by electron temperature within the voxel.

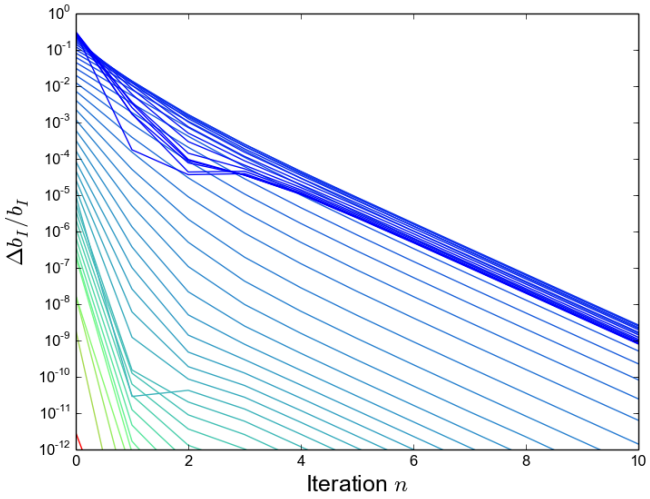

Figure 4.7: Convergence Rates for a parametrized 3D model within a G-Type star. $\Delta b_I^{(n,n+1)}/b_I^{(n)}$ for each iteration for the highest populated super level is shown, usually the one containing the ground state. Each line represents a different voxel and is color coded by electron temperature within the voxel.

4.5.2 Plane Parallel Models with Temperature Anomaly

Using the 27 super level model with a plane parallel setup with the same temperature structure as the spherical models, but including a temperature anomaly in the outer layers of the atmosphere, the convergence behaviour is more complicated. The convergence rates for two different temperature anomalies are shown in Figure 4.6. While most of the voxels show a similar convergence rate as in the spherical symmetric case, some voxels in the coolest parts of the anomaly show very poor convergence or are outright divergent. This is most likely due to the very low electron densities caused by the extremely low temperatures within the anomaly, which lead to extremely huge NLTE effects since the collisional rates are negligible.

In general, the convergence rate is better in voxels, where the NLTE effects are small or non existent due to high temperatures, pressures and electron densities which result in high collisional excitation rates that suppress the radiative excitation rates. This is shown especially by the convergence rates of a similar temperature anomaly in the atmosphere of a solar type star, shown in Figure 4.7. Here, the the temperature difference between the inside and the outside is steeper, but the lowest temperature is much higher than in the previous models. Thus, this model shows a far better convergence rates.

Chapter 5

Results

The new 3D implementation was used with a number of different atmosphere structures to test its function and capabilities. The spherically symmetric test case that was previously tested for LTE recovery under certain conditions, as discussed in chapter 4, was used to test the new implementation against the results of the 1D implementation for all three super level models to further ensure the correct working of the code. The results for this case were also tested against the 1D full NLTE solution without super level approximation to compare the viability of the different super level configurations.

To further investigate the effects that 3D temperature variations have on 3D NLTE radiative transfer, a small parametrized structure has been used.

5.1 Spherical Symmetric Model

As a final test for the new implementation, a spherical symmetric test case was set up, using the temperature structure of an M-dwarf with $T_{\text{eff}} = 2700\text{K}$ and $\log g = 5.0$. Solar element abundances, as given by Asplund et al. [2005], were used. M-dwarf atmospheres are both cool enough to form a large number of CO molecules, and have comparatively low electron densities so that strong NLTE effects are to be expected. The temperature structure has been generated with a Phoenix/1D model using LTE opacities. It was converged to attain energy conservation within the atmosphere using the temperature correction of Phoenix/1D.

This model is similar to one of the models used by Schweitzer et al. [2000] as a test for the 1D implementation of the super level method. Hence, the new 3D implementation could be tested against the results of the 1D code outside of the simple test conditions used before.

Additionally, the test models were drawn upon to investigate the different properties of the super level configurations, and their agreement with the full non-LTE results that were also obtained from the 1D implementation. The aim was to inquire which super level configuration shows the most reasonable ratio of accuracy and computational demands, as to decide which model should be used in future calculations.

To speed up the 3D calculation for this test, only CO lines were considered in the line selection both in 3D and in 1D. Other species were considered to be present in the solution of the equation of state, but did not contribute to the line opacities.

Unfortunately, in 3D each iterative step is computationally expensive, due to the need to replicate the same accuracy in the radiative transfer solution as in the 1D code.

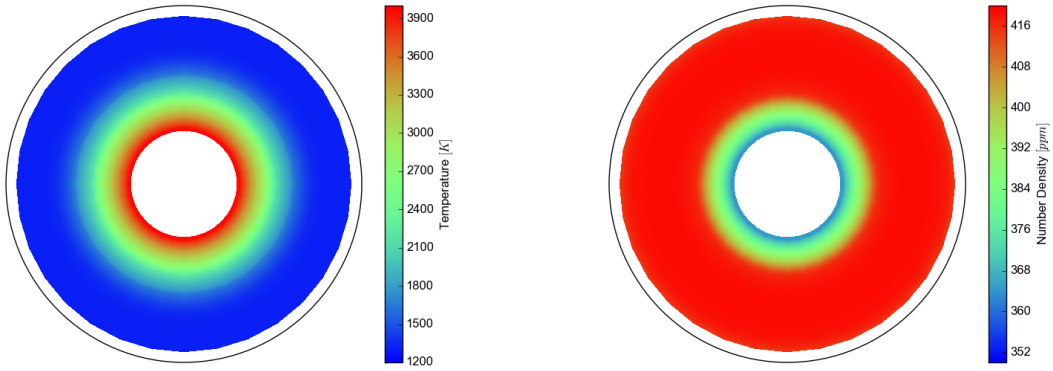

(a) Temperature T[K] (b) CO Density n_{CO}[ppm]

Figure 5.1: Spherical symmetric model: The temperature and CO number densities for each voxel color coded for a equatorial cut through the spherical grid are shown in the left and right panels respectively. Radial axis is not to scale, but shows voxels as equidistant since the atmosphere is only a very thin outer layer compared to the radius of the star.

Therefore, due to the limitations in available computation time, the 3D solutions were only partially converged for these tests. The 1D models that were used for comparison, however, where converged to full accuracy, wherever possible, as was already shown in the convergence tests for the implementation in chapter 4.5. It is, of course, not guaranteed that the 3D models would have continued to converge at the same rate, even though they show the same convergence behaviour as the 1D implementation in the iterations that were computed.

Figures 5.1, and 5.2 present the temperature structure, CO number density, electron number density, and pressure-temperature-relation for the model that was used. The calculation was done for a grid with 65 voxels in radial direction, and 33 voxels each in ϑ and ϕ. The radiative transfer was solved with a solid angle resolution of 72×72 angles to achieve the same accuracy as in the 1D solution. The corresponding 1D calculation was done for 64 layers, where each layer was mapped using the same radial grid as in 3D.

5.1.1 Departure Coefficients

The resulting departure coefficients b_I are shown in Figures 5.3 to 5.5 for each super level along a radial axis through the spherically symmetric structure. The converged results of the 1D calculations for the respective super level configurations are shown as dotted lines for the small models and a separate plot for the model using 350 super levels. The 1D calculations have been fully converged with 50 iterations each.

The departure coefficients from the 3D model reproduce the results from the 1D model very well. Small deviations can be explained by the fact that the 3D models have not been fully converged to reduce the necessary computation time (see section 4.5) and the limited resolution of the 3D model. However, these differences are small and mostly found for the lowly populated levels of high energy that also converge the slowest.

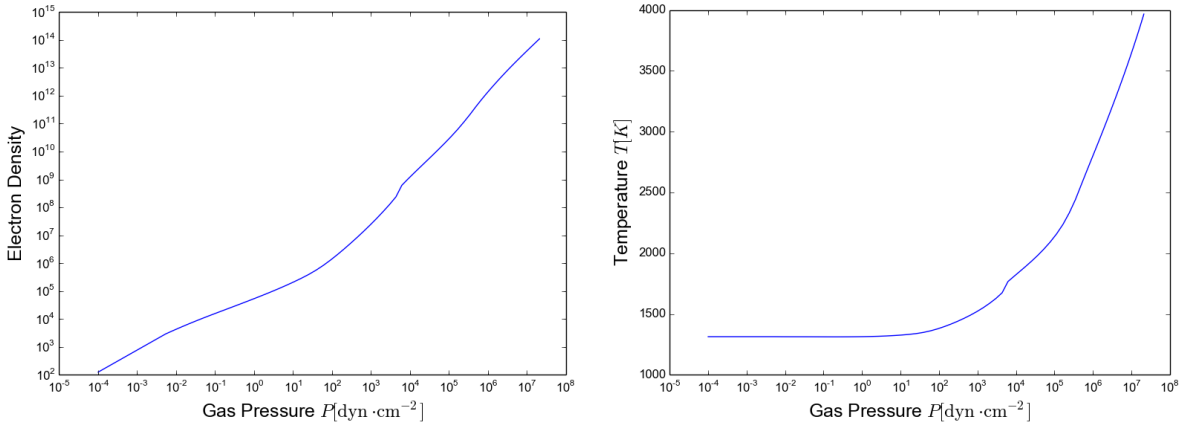

(a) Electron density

(b) Pressure-Temperature Relation

Figure 5.2: Relation between gas pressure P, electron density and Temperature T for a radial column of the grid.

In general, the results show that the NLTE effects are strongest in the optically thin outer parts of the atmosphere, where temperatures, pressures, and electron densities are low. Departure coefficients for all super levels remain at $b_I = 1.0$ up until a threshold of $T \approx 2000\mathrm{K}$ and $P_{\mathrm{Gas}} \approx 4.3 \cdot 10^4 \cdot \mathrm{dyn} \cdot \mathrm{cm}^{-2}$. The Quantum number Model (3.6.1) suggests an even lower threshold, where NLTE effects only appear at even higher levels of the atmospheres with temperatures below $T \approx 1600\mathrm{K}$ and pressures below $P_{\mathrm{Gas}} \approx 2.5 \cdot 10^3 \cdot \mathrm{dyn} \cdot \mathrm{cm}^{-2}$. At the outer boundaries of the atmosphere, all models show the largest deviations from $b_I = 1.0$ for all super levels, with b_I ranging from approximately 10^{-1} to 10^6 depending on the super level set up.

The overall structure of the resulting departure coefficients can not be explained merely by the presence of CO. The relative number densities for CO vary only by $\approx 10\%$ between the lower and upper boundary of the simulation grid, as can be seen in Figure 5.1b. However, while the temperature in the outer parts of the model atmosphere is fairly constant, pressure and electron density change rapidly, as can be seen in Figure 5.2. As electrons are currently the only species considered in the collisional rates, a low number of free electrons means that the collisional rates in these regions are equally low. In this way, the radiation field is dominant for the population of the levels here so that the NLTE effects are strong.

In LTE, where the population of all levels is tied solely to local temperature and pressure, the level population decreases exponentially with level excitation energy E_i so that levels of high energy are largely unpopulated in LTE. The radiation field's influence allows for population of levels that would have been originally almost unpopulated in LTE. Even if the absolute occupation numbers are still low, the departure coefficient showing only the degree of overpopulation can be very high due to the low n_I^*, reaching as high as $b_I \approx 10^6$.

Levels of lower energy that show a high population in LTE are depopulated accordingly

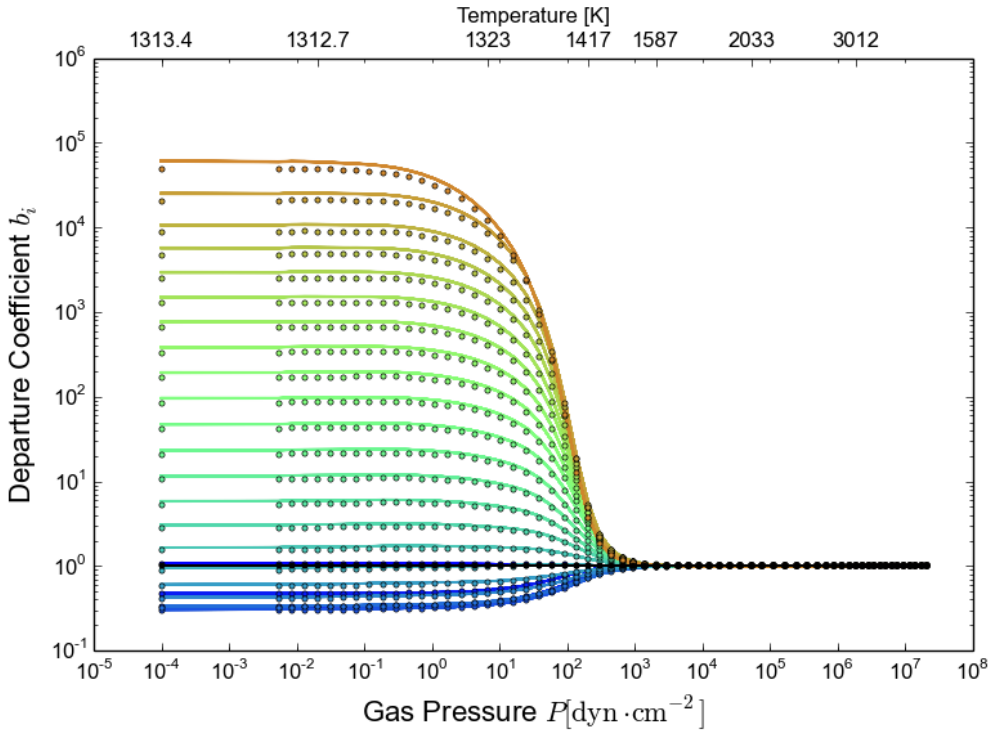

Figure 5.3: Spherical symmetric atmosphere, quantum-number-model (see chapter 3.6.1). Shown are the departure coefficients b_I of all super levels along a radial axis of the grid. Each line represents one super level of the 3D model, the color of the line represents the energy of the lowest level, which is part of the super level, where blue is the super level containing the ground state and black is the continuum (CO+ ground state). Dotted lines are the results of the converged 1D model with the same super level definition.

as additional upper states are occupied. While the absolute change is of course equal in number, the change compared to the LTE population density is of smaller magnitude resulting in departure coefficients between $b_I \in \{0.1, 1\}$.

Comparison between the different super level models suggests that the super level definitions using energy as a criterion for setting up the super levels (see chapter 3.6.2 and 3.6.3) are in closer agreement with the results of the full NLTE conditions, when comparing the magnitude of non-LTE effects. The difference is small near the outer boundary of the atmosphere, but the NLTE effects are much more limited to these outer layers in the quantum-number-defined model described in 3.6.1, than the full NLTE model suggests. This is counter intuitive, since the division by vibrational quantum number fulfils the requirement of strongly coupled levels within one super level to a greater extent. It suggests that a smaller range of energies for the levels associated with each super level is of greater importance, at least for this kind of calculation. However, it might also allude to the fact that the NLTE effects would have a strong effect on the temperature structure of the atmosphere, in particular in the line forming regions of the respective lines. Currently, this is not incorporated into these models as the 3D mode of PHOENIX does not support

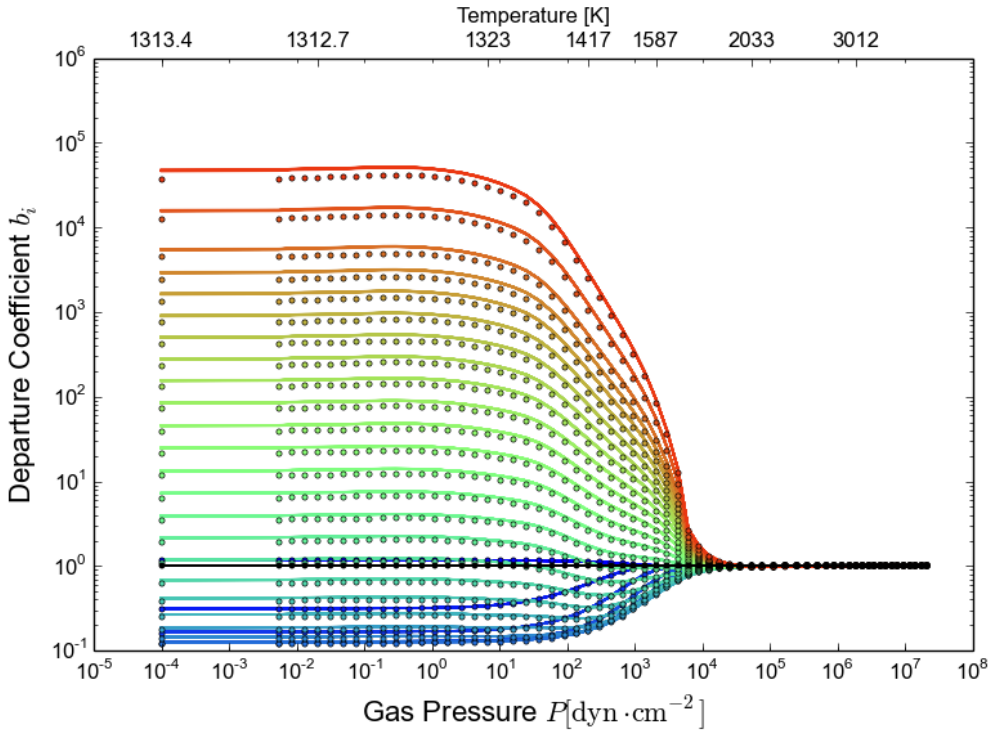

Figure 5.4: Spherical symmetric atmosphere, head-energy-model (see chapter 3.6.2). Shown are the departure coefficients of all super levels along a radial axis of the grid. Each line represents one super level of the 3D model, the color of the line represents the Energy of the lowest actual level within the super level, which is part of the super level, where blue is the super level containing the ground state and black is the continuum level (CO+ ground state). Dotted lines are the results of the converged 1D model with the same super level definition.

temperature correction yet.

All plots showing departure coefficients have been coloured, so that levels that were sorted into the same level in the energy defined super level models share the same line color. Since all levels within a super level share the same departure coefficient b_I, this allows for a limited comparison for the departure coefficients of individual levels i.

The full non-LTE results are shown in Figure 5.6, coloured to indicate to which super level each level of the head energy model described in 3.6.2 belongs to. Unsurprisingly, the departure coefficients of each actual level are spread out around the super level departure coefficient b_I, and follow a similar trend. This spread is smaller for higher temperatures, where non-LTE effects are not as pronounced, but there are also some super levels with levels of intermediate level energy E_i that overlap with levels that are part of a different super level. We expect the differences to the full non-LTE model to be larger here, due to the fact that the super level model can not reproduce this behaviour. Again, one should stress the fact that NLTE effects are sensitive to more than temperature, so that the quality of each model might have to be assessed very differently for vastly different temperature and pressure structures.

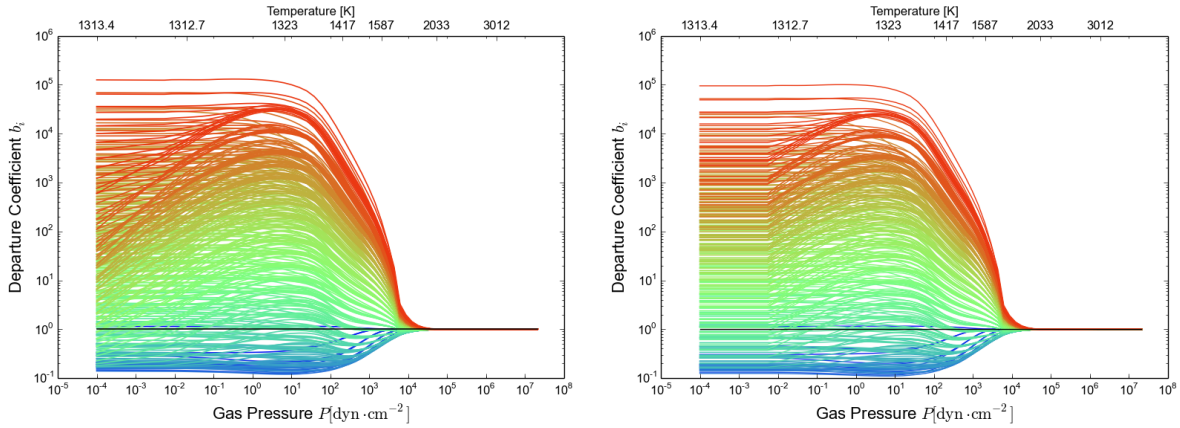

(a) 3D Model

(b) 1D Model

Figure 5.5: Spherical symmetric atmosphere, head-energy-and-quantum-number super level model (see chapter 3.6.3). Shown are the departure coefficients of all super levels along a radial axis of the grid. Each line represents one super level, the color of the line represents the super level of the Head Energy model, which this super level is a subset of and the black line is the continuum (CO+ ground state).

By construction, the model using 350 super levels is an intermediate step between the full calculation and the smaller models, showing a similar spread of super levels that constitute a super level in the small model. In general, all super level models seem to underestimate the non-LTE effect, especially for levels of high excitation energy. This is, primarily, due to the fact that the high departure coefficients result from the low LTE populations of these levels, which is reduced by the fact that several levels are summed up, especially in the quantum-number model, where each super level includes several levels of low energy which are always highly populated. This is, in part, compensated by the fact that the actual populations for each level are still calculated with consideration of the level energy.

5.1.2 Effects on the Opacities

The comparison between the opacity for two different CO lines in the $\Delta\nu = 1$ and $\Delta\nu = 2$ bands shown in Figures 5.8 and 5.9 reproduces similar differences between the models, which have already been found for the departure coefficients. The models that use level energy as criterion agree extremely well with little to no differences between the resulting line opacity. The quantum-number-divided model shows a different behaviour between 1400 K and 1600 K, where the differences in departure coefficient are strongest, while the departure coefficients themselves are no longer close enough to unity for the opacity to be unaffected. The differences between the models are stronger in the $\Delta\nu = 2$ band around 2.3 micron, but the absolute opacities are much smaller in this band.

Compared to the LTE opacities, represented in black dashed lines in the plot, the differences are, as expected, primarily between 1300 K and 1600 K, where the NLTE opacities are larger than the LTE opacities in the $\Delta\nu = 1$, band but smaller in the $\Delta\nu = 2$ band. In general, the resulting NLTE opacities of the quantum-number-divided

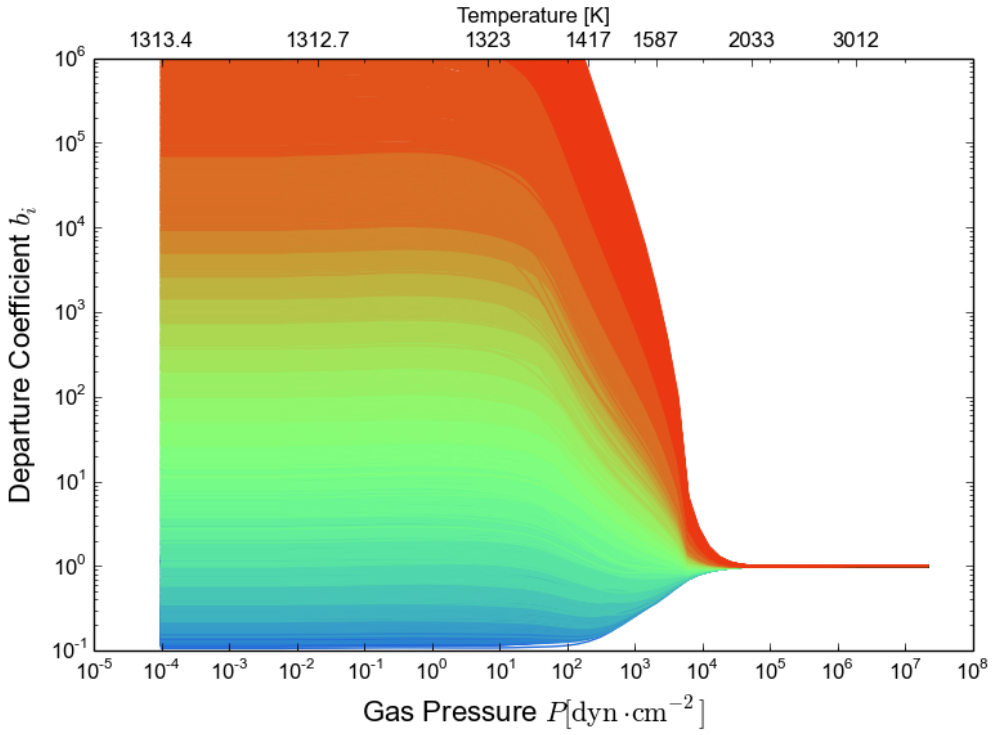

Figure 5.6: Spherical symmetric atmosphere, 1D results with 3623 levels in NLTE (See chapter 3.6.4). Shown are the departure coefficients of all actual levels along a radial axis of the grid. Each line represents one actual level, the color of the line represents the super level of the head-energy-model, which this level is a subset of.

model are much closer to LTE than their counterparts.

5.1.3 Effects on the Spectrum

Comparison of different super level models

Figures 5.10, 5.11 and 5.12 depict parts of the resulting spectrum. The black lines represent the outgoing flux $F_{r,\lambda}$ for all surface voxels of the 3D calculation. The spectra for different surface voxels are, of course, not completely identical, even though the model itself is spherically symmetric. This is explained by the fact that there is only a finite number of characteristics that have been used in the solution of the radiative transfer, so that not all surface voxels are sampled in exactly the same way. [see e.g. Hauschildt and Baron, 2010] As is evident, the spread is dependent on the magnitude of the flux, so that the effect is smaller at the center of spectral lines, where the overall Flux $F_{r,\lambda}$ is lower. This spread could be reduced by increasing the number of solid angles, which are used to compute the formal solution - in this case, $72^2 = 5184$ solid angles have been used.

The red and green dots mark the results of fully converged 1D calculations that have been used for comparison. While the red dots show the outgoing spectrum using the same super level definition, the green dots show the results of the full non-LTE calculation. For the two wavelengths regimes of the $\Delta\nu = 1$ and $\Delta\nu = 2$ CO bands shown here, the results

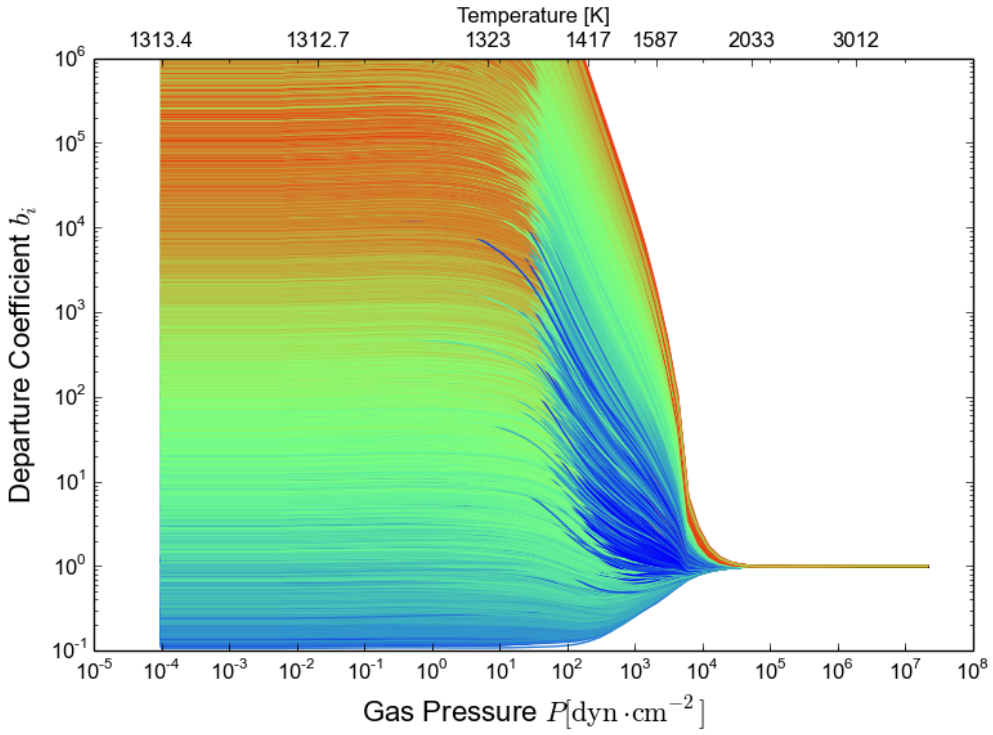

Figure 5.7: Spherical symmetric atmosphere, 1D results with 3623 levels in NLTE (See chapter 3.6.4). Shown are the departure coefficients of all actual levels along a radial axis of the grid. Each line represents one actual level, the color of the line represents the super level of the quantum-number-model, which this level is a subset of.

agree quite well with their 1D counterparts of the same model.

The $\Delta\nu = 2$ band around 2.3μm shows good agreement between all models as well as the full NLTE calculation. In the 4.4μm band, the full non-LTE model predicts stronger lines than all three super level models, with the difference being notably larger for the line at 44663 Å in the quantum number model. Here, the differences in occupation numbers for the deeper parts of the upper atmosphere show the greatest effect on the outgoing spectrum.

Comparison with LTE spectrum

Figure 5.13 shows the comparison between the resulting spectra for the head-energy-method 3.6.2 compared to a 1D calculation using LTE occupation numbers. The upper part of the figure shows several CO lines of the $\Delta\nu = 2$ band around 2.3 micron. In this band, all lines match with the corresponding LTE results and do not show any NLTE effect in any of the models. This is the reason for the good agreement of all models in this CO band. Since all lines are unaffected, and only a limited and in all models different number of lines is calculated without direct influence on the radiative rates due to limitations of the super level model, this suggests that this is indeed a physical effect.

The lack of NLTE effects in the $\Delta\nu = 2$ band can be explained by the optical depth for different wavelengths points, which is shown in Figures 5.14 and 5.15. For these lines

the optical depth of $\tau_\lambda = 1$ is reached in the lower parts of the atmosphere below the region where the NLTE effects are strong. This means, the atmosphere is optically thin in the region that shows departure coefficients different from $b_i = 1.0$ for this wavelength regime, and the lines are formed in a region, where a high rate of collisions has restored LTE conditions.

In contrast, the lines of the $\Delta\nu = 1$ band at 4.4 to 4.6 micron show a discernible difference to the LTE spectrum in several lines. The corresponding optical depth for these wavelengths reaches $\tau_\lambda = 1$ at a higher altitude, so that these lines form in a layer, where NLTE effects are already significant in the two energy separated models. However, this is also the region where the difference between the head-energy-model, the head-energy-and-quantum-number-model and the model sorted solely by quantum number is highest, explaining the differences between the models.

The differences to the full non-LTE calculations are rather small even though the super level models underestimate the strength of the non-LTE effect. The differences between super level models and full NLTE models dwindle with increasing temperature and are less important in the line forming regions of the atmosphere, while they are most pronounced at the optically thin edge of the atmosphere.

5.1.4 Conclusions

The results obtained from the spherical symmetric tests reproduce the results of the 1D code well. The head-energy-model and the head-energy-and-quantum-number model are reasonably close to the results of the 1D full NLTE model both in departure coefficients and, more importantly, resulting spectrum. However, the model using both energy and quantum number to determine level distribution into super levels has more than ten times as many super levels as the simpler model using only energy. The model shows a wider range of departure coefficients that match the results of the full NLTE model more closely. Nevertheless, the resulting NLTE opacities and outgoing spectra of both models are almost identical both slightly underestimating the line depth shown by the full NLTE results.

In this way, the head-energy-model is the best choice out of the available models, since the solution of the rate equations is performed about ten times faster and uses only a quarter of the memory of the energy and quantum divided model, due to a low number of super levels, but still shows reasonably good results. Furthermore, due to the high number of super level internal transitions, this model also requires the fewest wavelength points as transitions within super levels do not contribute to the rate integrals and, thus, do not need to be sampled for each NLTE iteration. Sampling these lines is only necessary when producing output spectra once the model is converged or when additional features that require a sampling of the entire wavelength regime such as temperature correction are used. Thus, this model is overall less computationally expensive. However, the difference between both models might be larger for vastly different atmospheric structures.

The model using only the quantum number as a sorting criterion shows only very small NLTE effects in the optically thin parts of the atmosphere, where the influence on the outgoing spectrum is small. The problem of the wide ranges of level energies within each super level seem to outweigh the benefit of the strongly coupled levels, at least in this

case, especially since the full NLTE departure coefficients are clearly favouring a grouping of levels by energy, as is obvious from the comparison of Figures 5.6 and 5.7, showing the departure coefficients of the full NLTE solution coloured to show the matching levels in the head-energy, as well as the quantum-number-model.

This also explains, why this model shows a much better convergence rate. The resulting spectrum is close to the LTE solution, since the departure coefficients remain close to $b_I = 1$ in every region but the optically thinnest. The optically thin outer layers, in turn, have only a limited influence on the radiation field. For this reason, this model converges much faster than the other two models, as the starting conditions are closer to the to the final result, requiring fewer iterations than the other two models, where NLTE effects have a stronger influence.

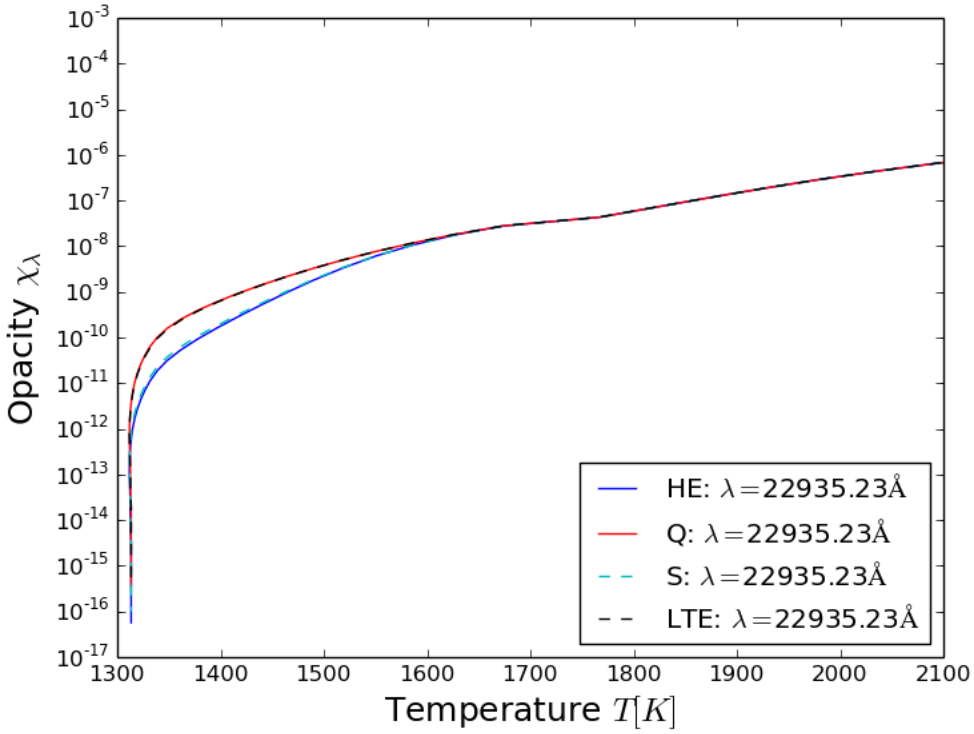

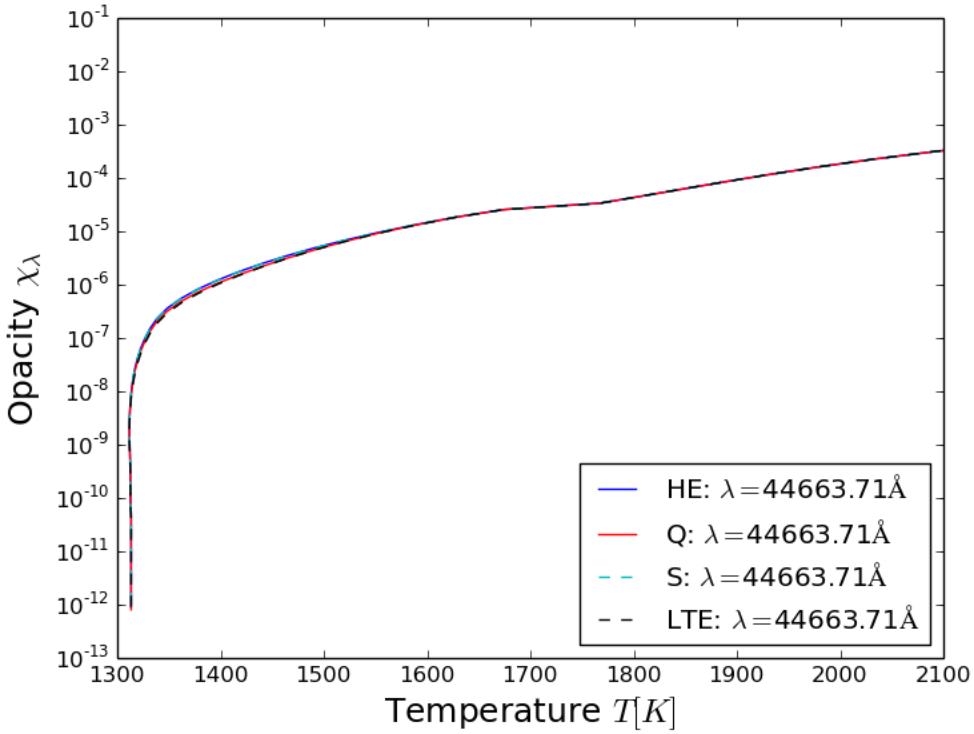

Figure 5.8: Opacities χ_λ for a $\Delta\nu = 2$ line at $\lambda = 22935.23$Å and a $\Delta\nu = 1$ line at $\lambda = 44663.71$Å plotted over temperature T for all models as well as LTE opacities. Q: quantum-number-model 3.6.1, HE: head-energy-model 3.6.2 S: energy-and-quantum-number-model 3.6.3.

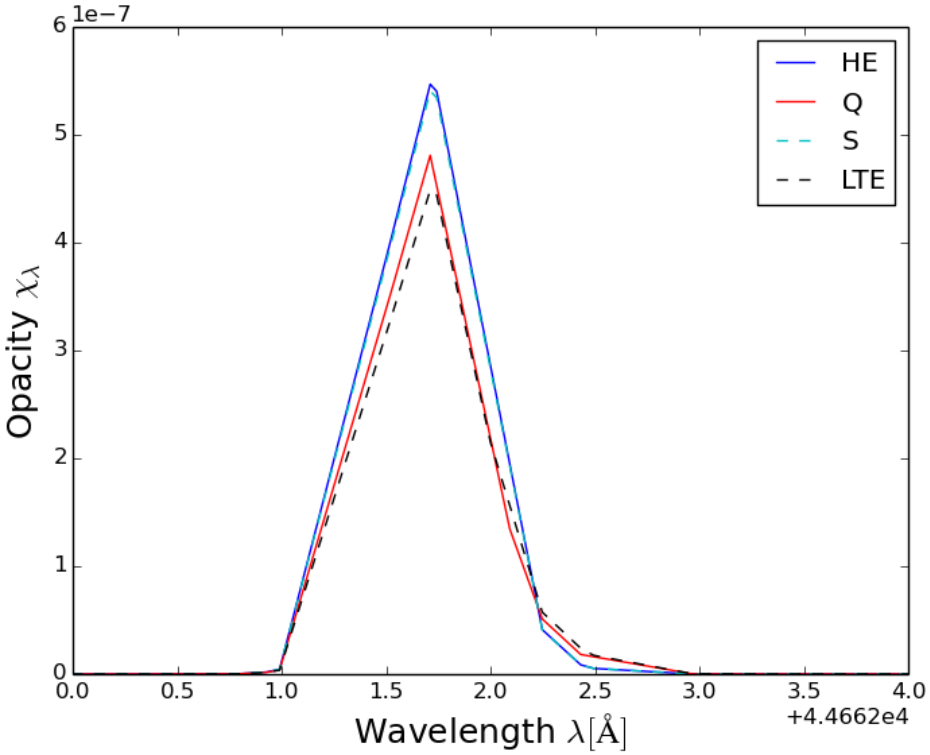

(a) T = 1361 K

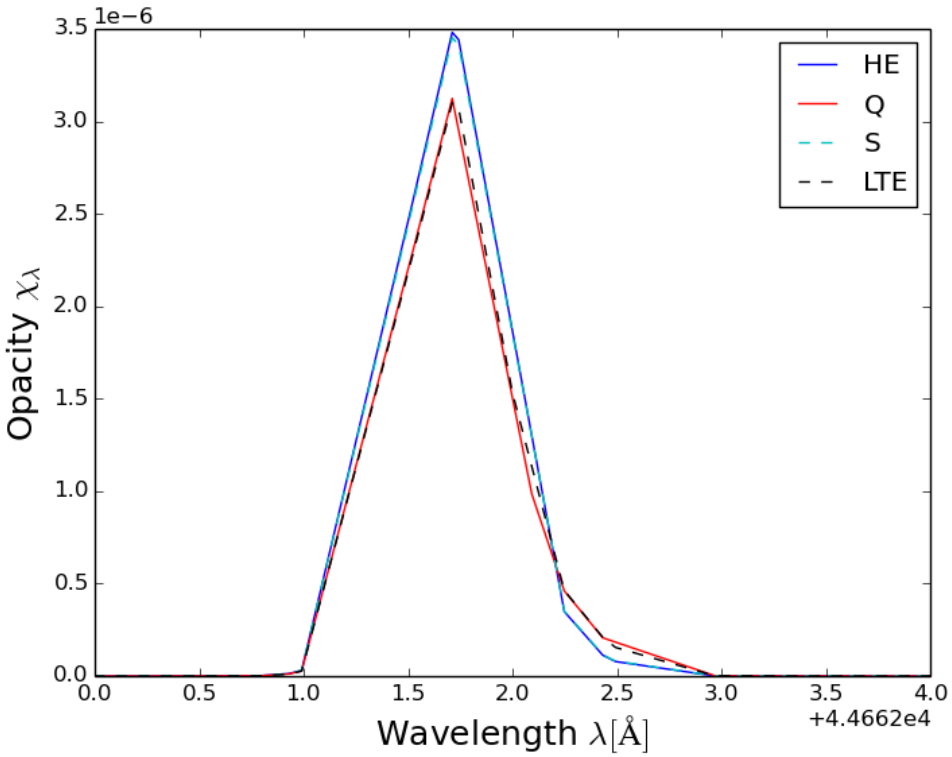

(b) T = 1464 K

Figure 5.9: Spherical symmetric model, opacity for one line in the $\Delta\nu = 1$ band. Shown are all three super level models, as well as LTE opacities for two different layers of the atmosphere.

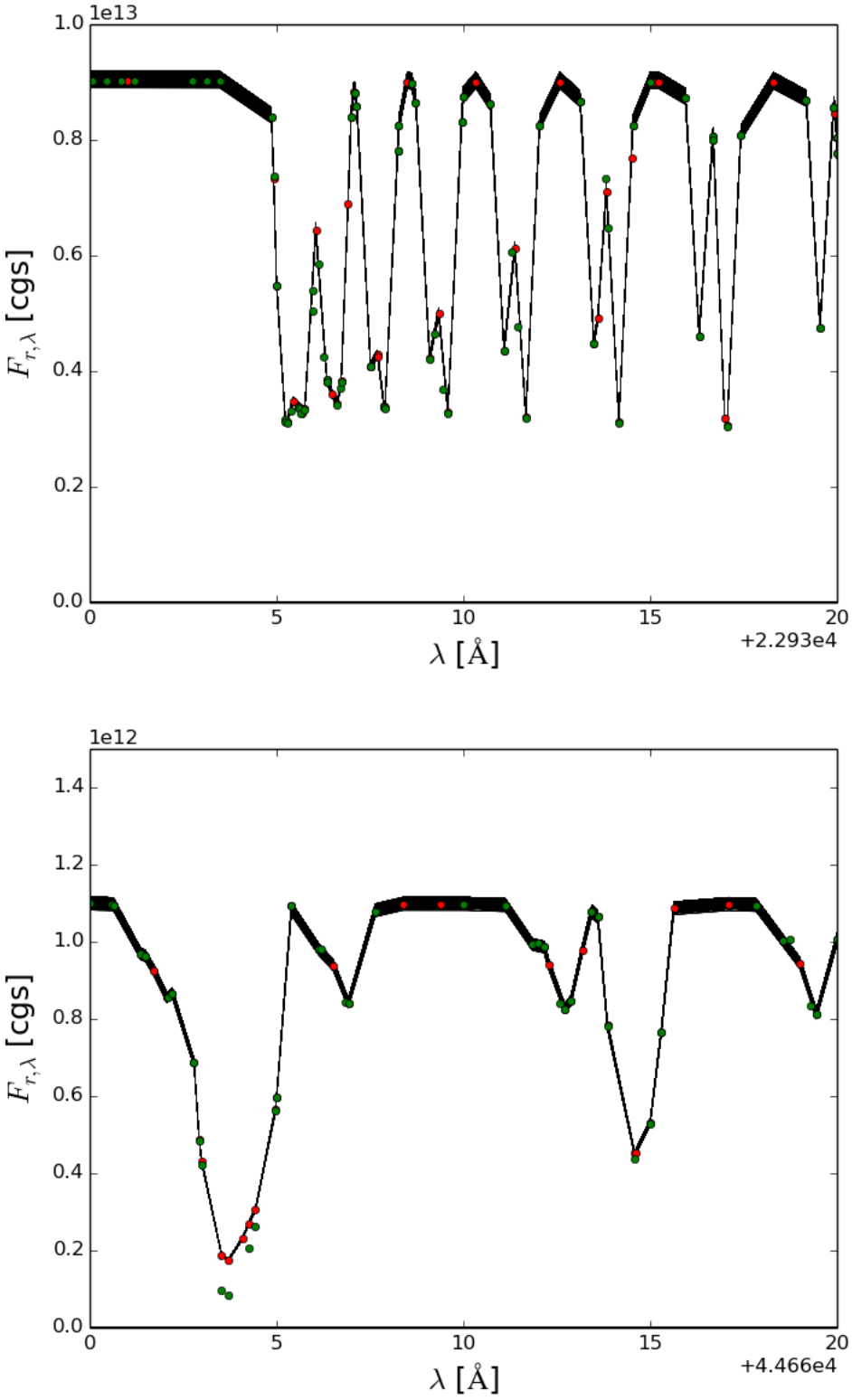

Figure 5.10: Outgoing flux for all surface voxels (black) compared to 1D models for same super level definition (red) as well as full NLTE model (green). Quantum-number-model 3.6.1.

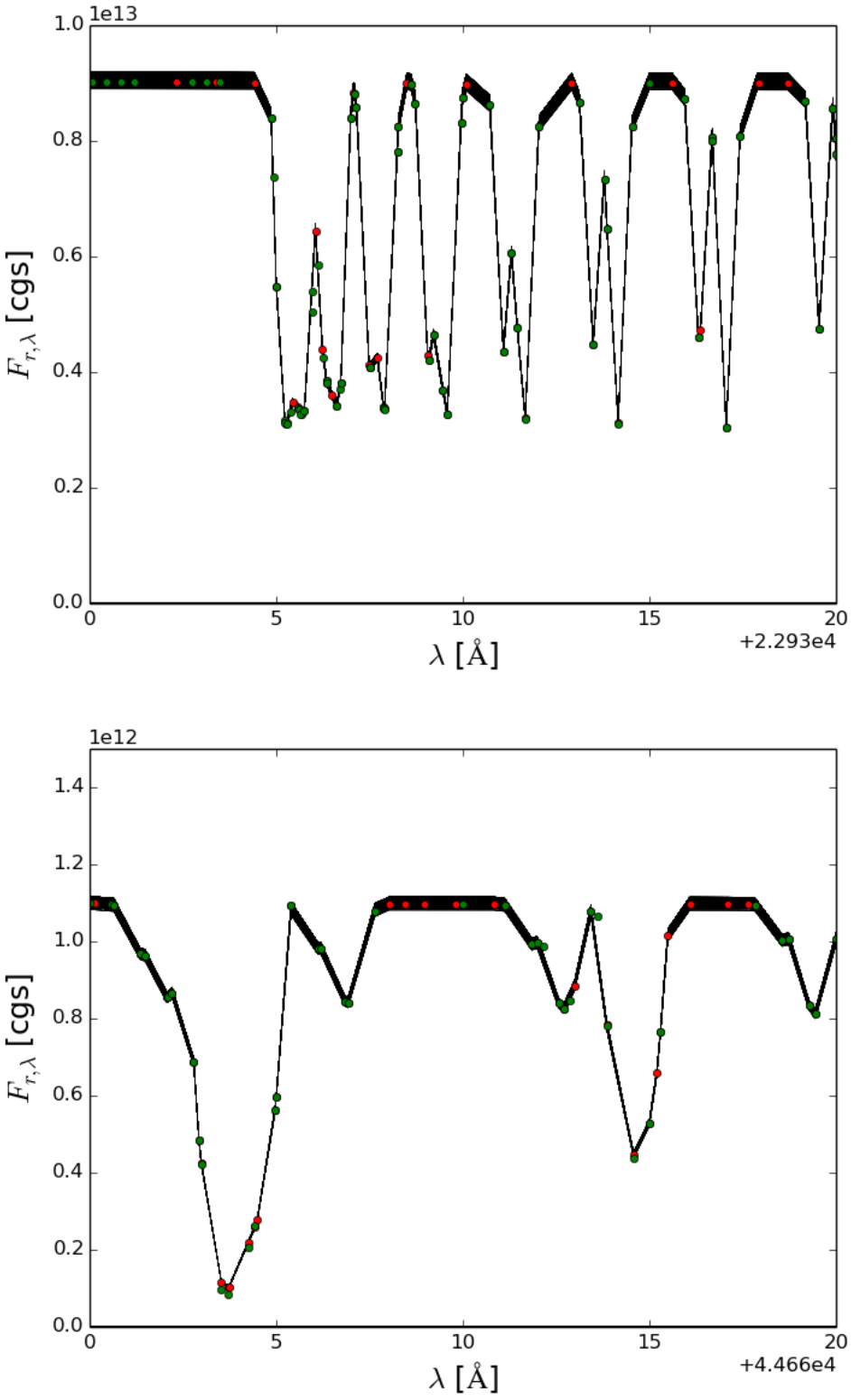

Figure 5.11: Outgoing flux for all surface voxels (black) compared to 1D models for same super level definition (red) as well as full NLTE model (green). Head-energy-model 3.6.2.

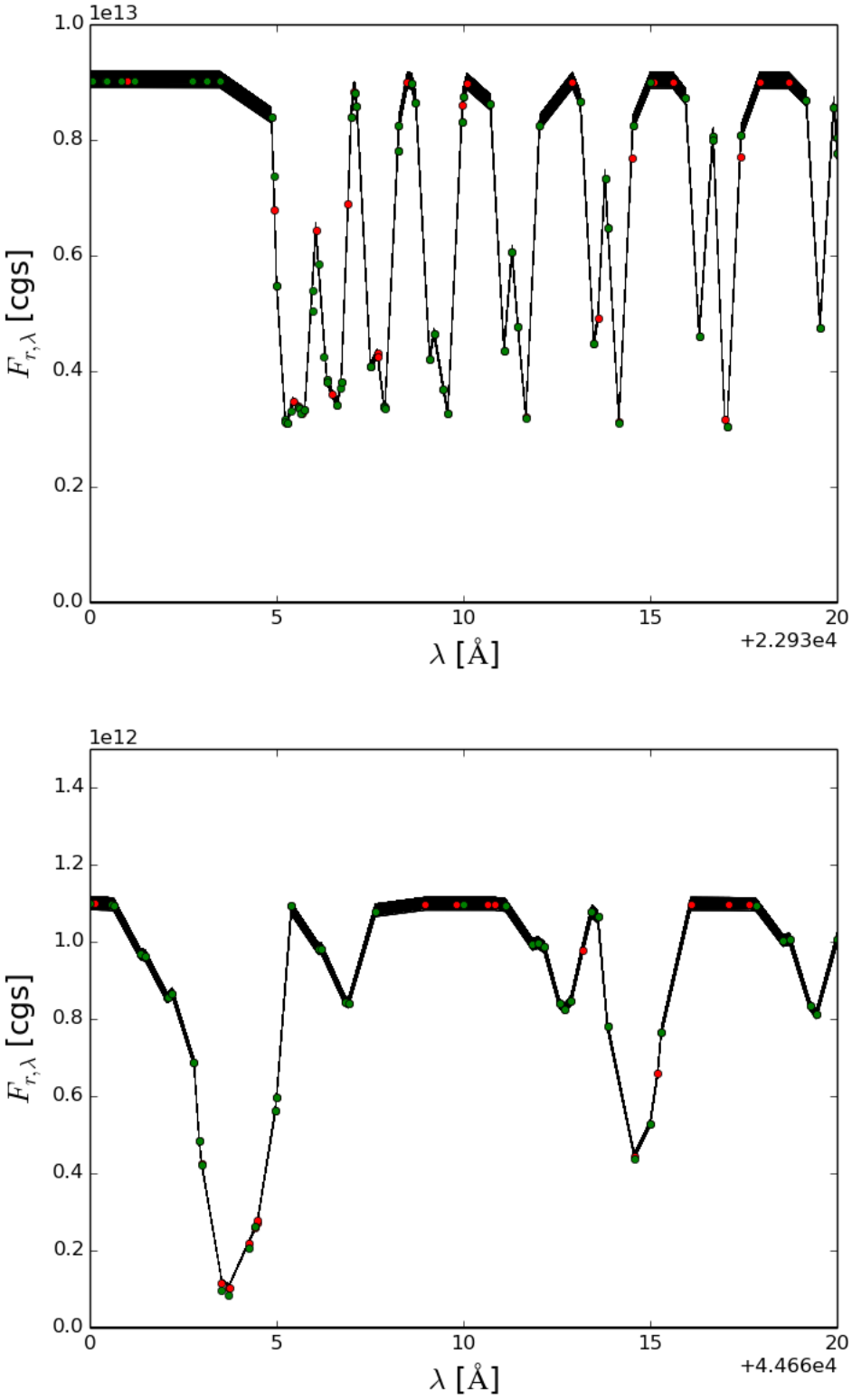

Figure 5.12: Outgoing flux for all surface voxels (black) compared to 1D models for same super level definition (red) as well as full NLTE model (green). Head-energy-and-quantum-number-model 3.6.3.

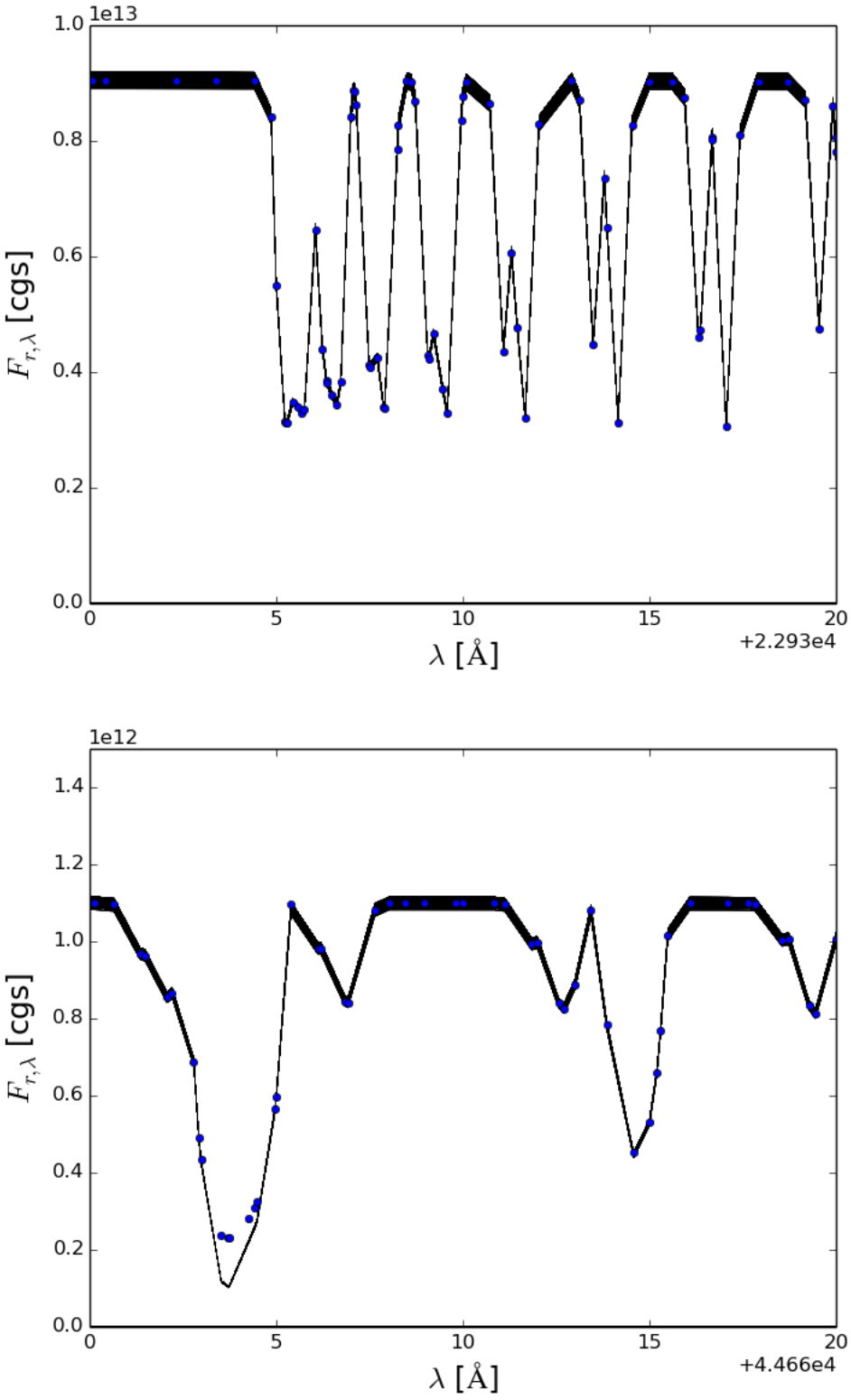

Figure 5.13: Outgoing flux for all surface voxels (black) compared to 1D model using LTE occupation numbers (blue). Head-energy-model 3.6.2.

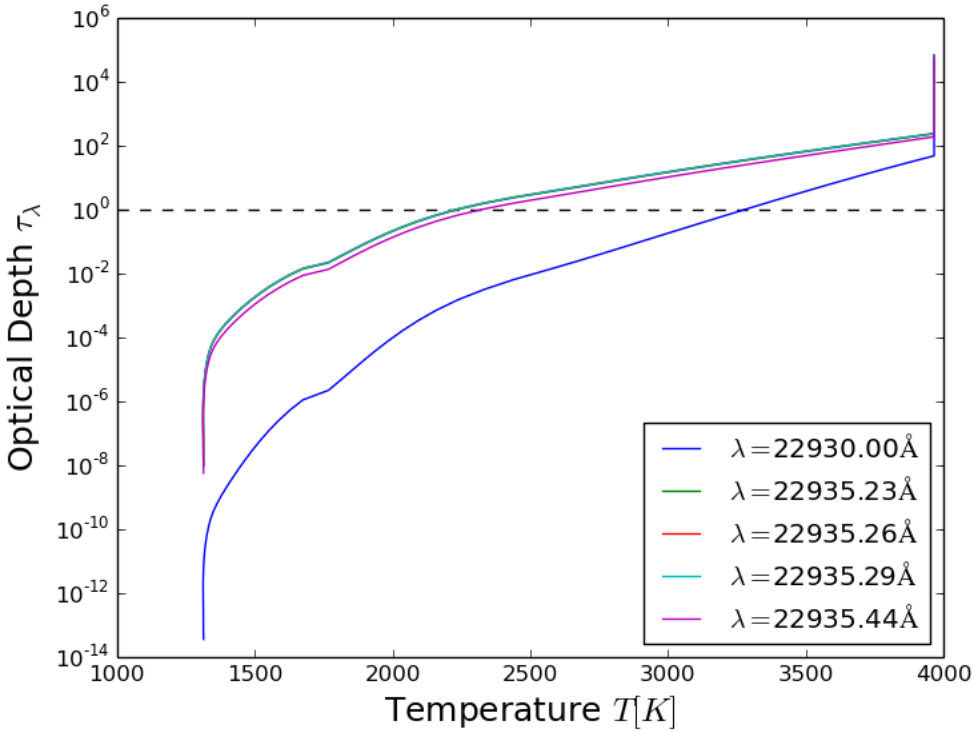

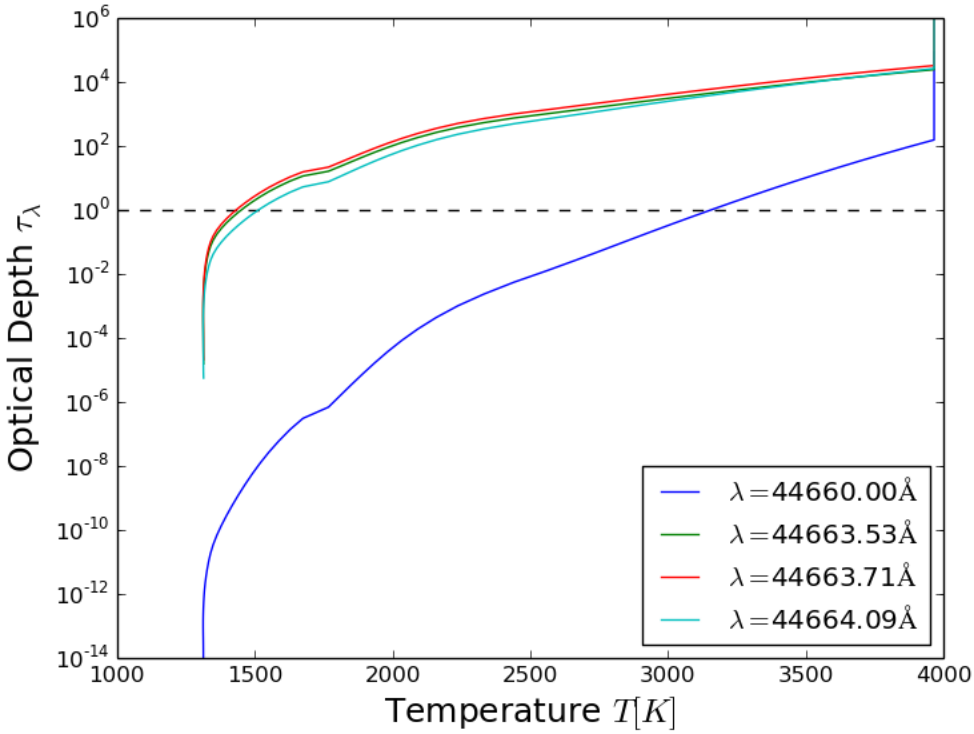

Figure 5.14: Optical Depth τ_λ calculated for each wavelength λ plotted over temperature to show the line forming regions for different CO bands, here using the resulting opacities for the quantum-number-model 3.6.1. Dark blue line represents a continuum wavelength point just outside the line.

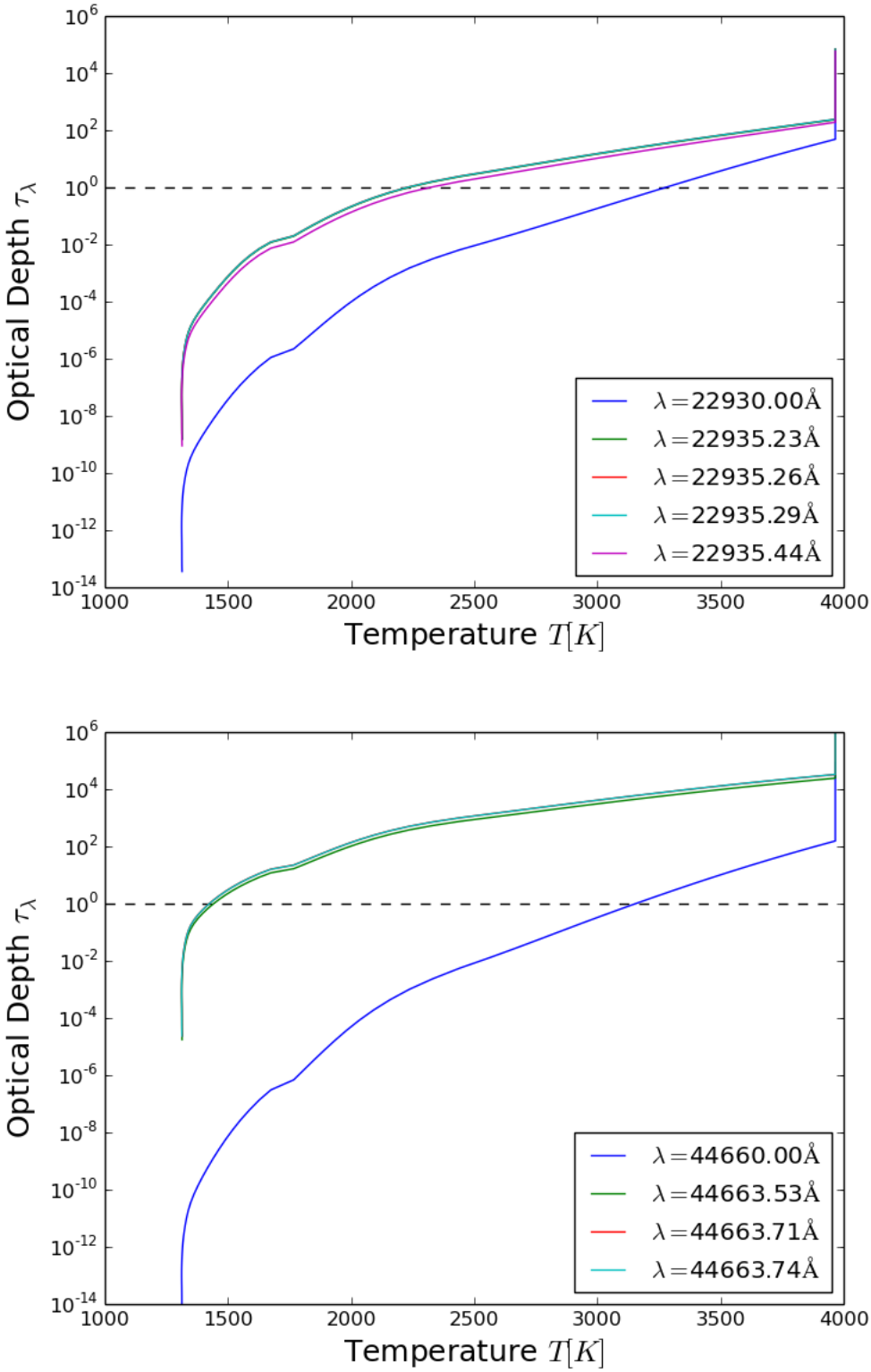

Figure 5.15: Optical Depth τ_λ calculated for each wavelength λ plotted over temperature to show the line forming regions for different CO bands, here using the resulting opacities for the head-energy-model 3.6.2. Dark blue line represent continuum a wavelength point just outside the line.

5.2 Parametrized 3D Model

Using the same base model structure for $T_{\text{eff}} = 2700K, \log g = 5.0$ as in the spherically symmetric models on a plane parallel grid, a small zone of locally reduced temperature was introduced to test how a 3D temperature structure would be affected by NLTE effects. This anomaly could represent several different phenomena with temperature variations within stellar atmospheres, stellar pores and starspots, caused by variations in the local convection being just one of the many possibilities. Another possibility that would lead to strong temperature variations, albeit leading to a hot spot, would be irradiation caused by a companion.

In this work, we chose a fairly regular and localized cool structure, as to better be able to separate the effects caused by the structure itself and the additional NLTE effects. For the first calculations, the pressure structure was left unchanged to simplify the models.

The parametrization model described by Berkner et al. [2013] was used to introduce the temperature anomaly. The calculations were performed for $33 \times 9 \times 9 = 2673$ voxels on a Cartesian grid with periodic boundary conditions. 64×64 solid angle points were used for the formal solution. The head-energy super level set-up was used in all cases, as it has shown the best performance of all three super level models (see previous section).

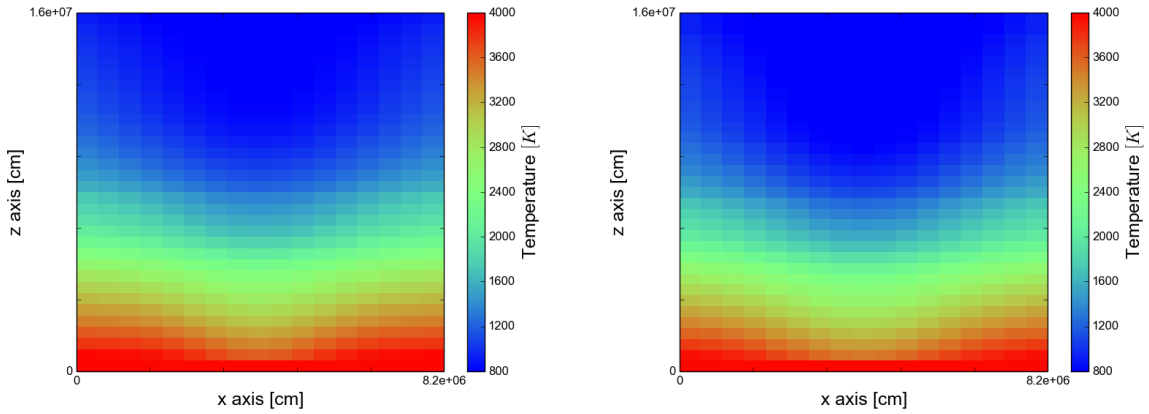

(a) Model A: $r_0 = 6 \cdot 10^6$cm
$z_0 = 2 \cdot 10^7$cm, $z_{\text{scale}} = 3 \cdot 10^7$cm
$\Delta T_0 = -600$K

(b) Model B: $r_0 = 5 \cdot 10^6$cm
$z_0 = 4 \cdot 10^7$cm, $z_{\text{scale}} = 4 \cdot 10^7$cm
$\Delta T_0 = -700$K

Figure 5.16: Temperature structures using a parametrized 3D model. Shown is a vertical slice of the voxel grid through the core of the cylindrical symmetric temperature anomalies.

The calculation was done for two different parametrization models using different anomaly sizes and core temperatures. In *Model A* the anomaly was chosen to be wide but shallow, with a core temperature difference of $\Delta T_0 = -600$ K, a radius of $r_0 = 6 \times 10^6$ cm, a lower boundary of $z_0 = 2 \times 10^7$ cm and a scale depth of $z_{\text{scale}} = 3 \times 10^7$ cm.

The *Model B* anomaly is slightly narrower and has a lower floor and a steeper temperature profile due to the lower core temperature, with $\Delta T_0 = -700$ K, $r_0 = 5 \times 10^6$ cm, $z_0 = 4 \times 10^7$ cm and $z_{\text{scale}} = 4 \times 10^7$ cm.

The resulting temperature structures are shown as vertical slices through the grid in Figure 5.16. The resulting relative density of CO calculated by the standard equation of

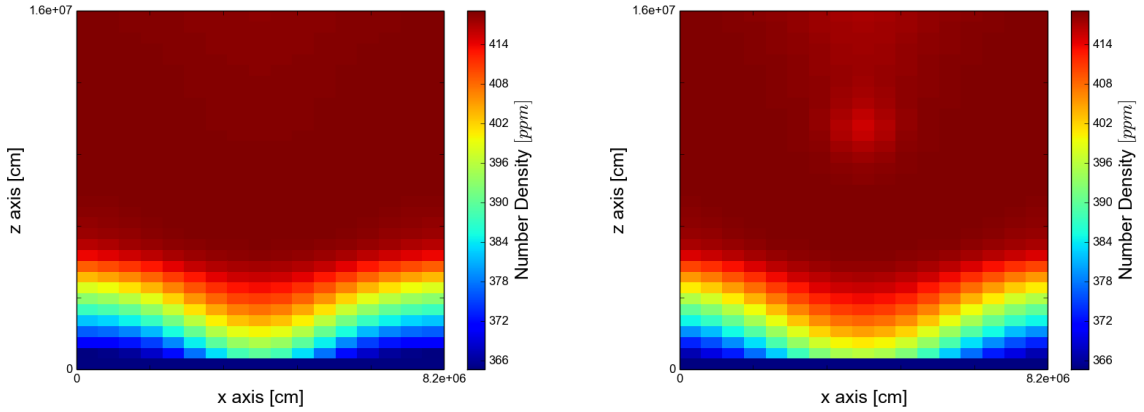

(a) Model A (b) Model B

Figure 5.17: Relative CO number density using a parametrized 3D model. Shown is a vertical slice of the voxel grid through the core of the cylindrical symmetric temperature anomalies.

state is shown in Figure 5.17 and the electron density in Figure 5.18. As can be seen, the relative CO density is actually lower in the cool parts of the anomaly, compared to the surrounding atmosphere. This suggests a lower threshold depending on temperature and pressure, where other carbon based molecules become dominant compared to CO.

The electron density drops with temperature and is rapidly cut off at in the lower parts of the anomaly. This is partly due to the low temperatures and even magnified by the fact that the pressure was left unchanged to simplify the model so that the pressure is comparatively high, which further reduces the number of free electrons.

5.2.1 Resulting Departure Coefficients

Since the atmospheric structure underlying the anomaly is similar to the structures used in the previous section, we expect NLTE effects in the upper atmosphere, as well as within the even cooler anomaly. This is confirmed by Figures 5.19 and 5.21 showing the departure coefficients for vertical slices of the voxel grid. Each individual sub-figure represents the departure coefficients b_I for one super level. Unsurprisingly, the 3D departure coefficients follow the temperature closely and are confined to the region of low electron density, mirroring the results of the spherical symmetric atmosphere. NLTE effects are strongest in regions where the temperature is low and LTE is restored towards the bottom of the grid.

The difference between both models are best seen in the super levels consisting of levels with low excitation energy. Model A shows a more or less even degree of under-population for the levels of lowest energy for the entire structure, where the rim of the structure is still in LTE. At higher excitation energies, the levels tend to be overpopulated compared to LTE, while the effect spreads from the zone of lowest temperature outwards to higher temperature.

In model B, the under-population of levels of low energy is limited to the rim of the structure, while the zone of lowest temperature is overpopulated for almost all levels

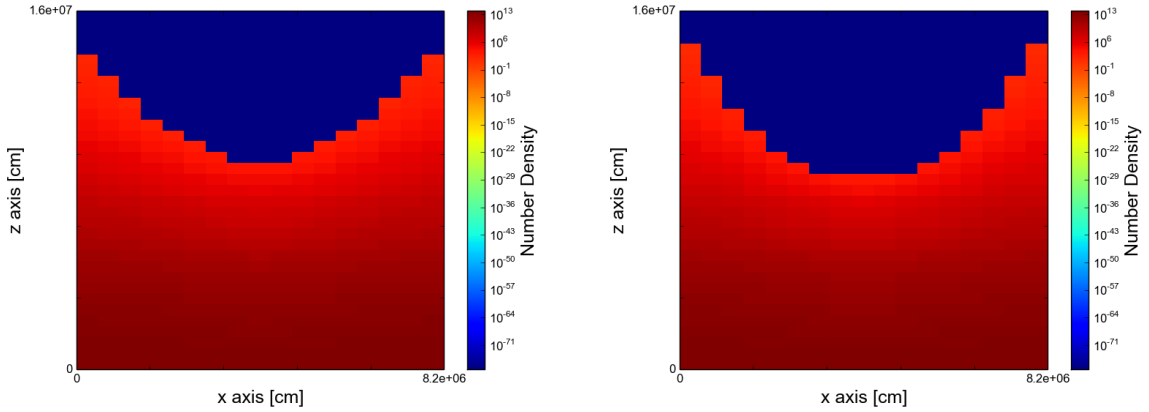

(a) Model A (b) Model B

Figure 5.18: Electron Density. Shown is a vertical slice of the voxel grid through the core of the cylindrical symmetric temperature anomalies.

besides the super ground state. This shows that the strength of the NLTE effects are highly sensitive to temperature, especially for levels of low excitation energy. These levels tend to be underpopulated until the temperature drops below a certain threshold, which is met in Model B, but not in Model A.

To allow for a more direct comparison of both models, Figure 5.23 shows the departure coefficients for two vertical columns of the grid. One column was chosen from the center of the temperature anomaly, while another was taken from the very edge of the grid, as far away from the anomaly as possible.

Model B, using a steeper temperature structure with a more localized anomaly, shows a greater difference between both columns, with lower over population of highly energetic super levels on the outside and a much stronger degree of super excitation in the center of the structure. On the other hand, the zone of under population is limited to the lower parts of the temperature anomaly, while there is almost no under population of any state besides the super ground state in the outermost layers of the anomaly, in the voxels with the lowest temperature.

The NLTE effect is strongly localized within the anomaly, which is due to the fact that there are almost no free electrons within this region, so that the corresponding collisional rates will be close to zero and population and depopulation is dominated by the radiation field originiating from different layers of the atmosphere. This allows for extremely strong deviations from LTE and is consistent with the results of the previous section.

As can be seen, the departure coefficients of both structures differ even at the very edge of the grid. While this might in part be due to the influence of the radiation that passed through the anomaly itself, it is certainly also due to the fact that the temperature structure is not completely identical, as the edge of the grid is not that far away from the anomaly, as the grid was kept as small as possible to reduce the computational requirements of the calculations.

In Figures 5.20 and 5.22 the absolute occupation numbers for NLTE and LTE are compared directly. As was already shown by the resulting departure coefficients, the NLTE

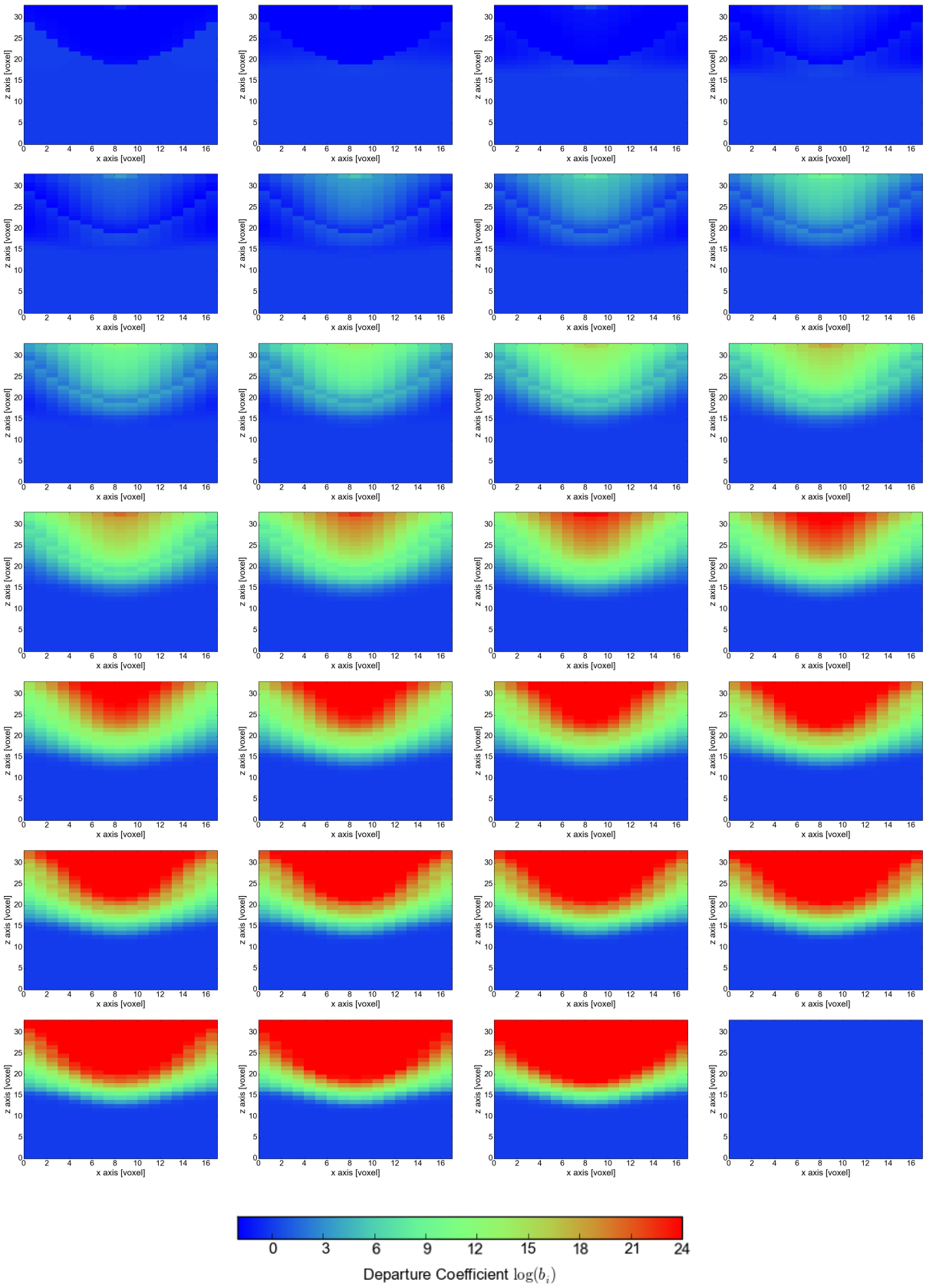

Figure 5.19: **Model A**: Departure coefficients for all 27 super levels shown as a color coded vertical slice through the center of the voxel grid and the anomaly. Upper left corner is super level containing ground state, lower right corner is continuum level.

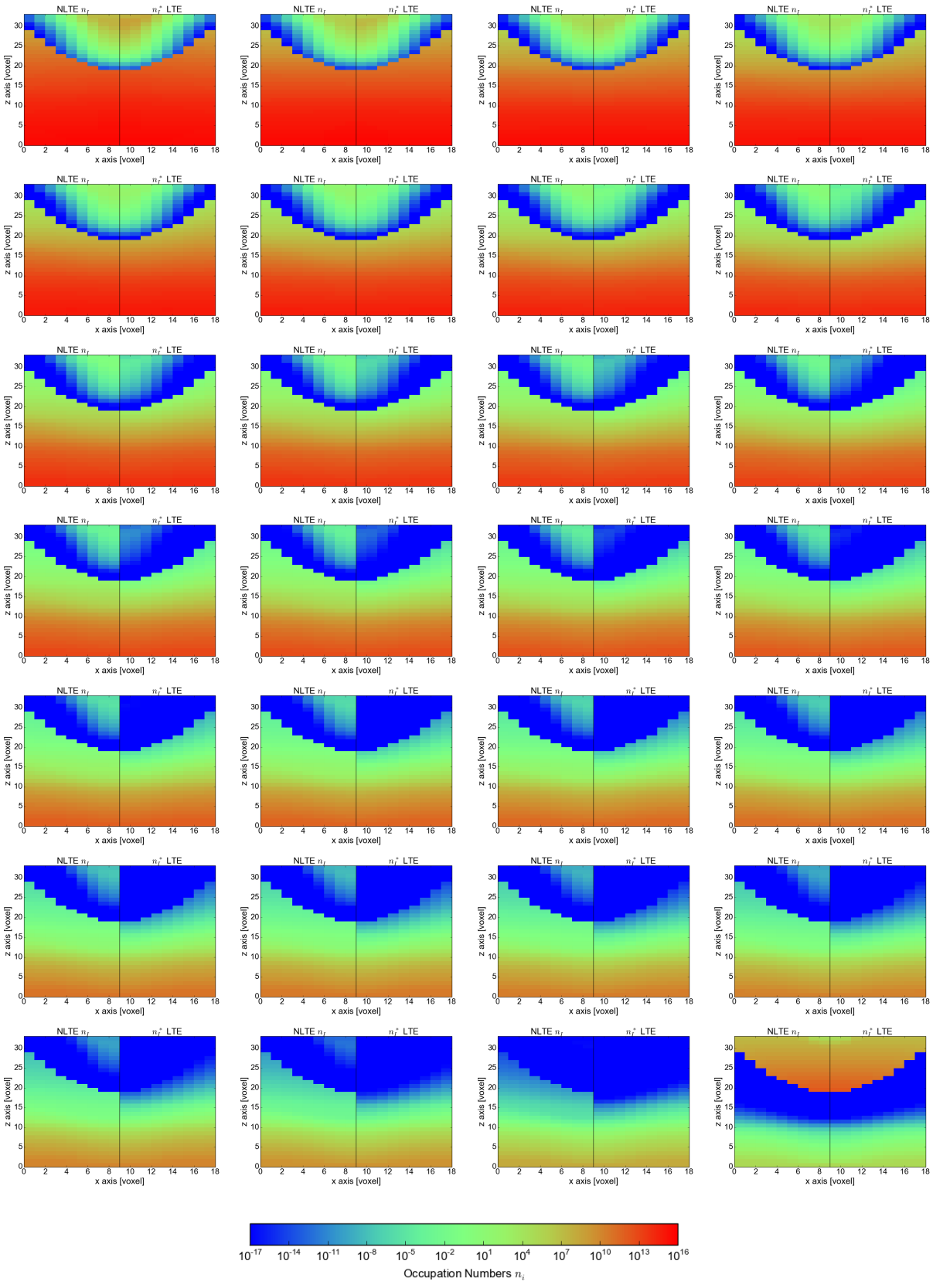

Figure 5.20: **Model A**: NLTE occupation numbers n_I compared to LTE occupation numbers n_I^* for all super levels. Left half of plots is NLTE, right half is LTE. Upper left corner is super level containing ground state.

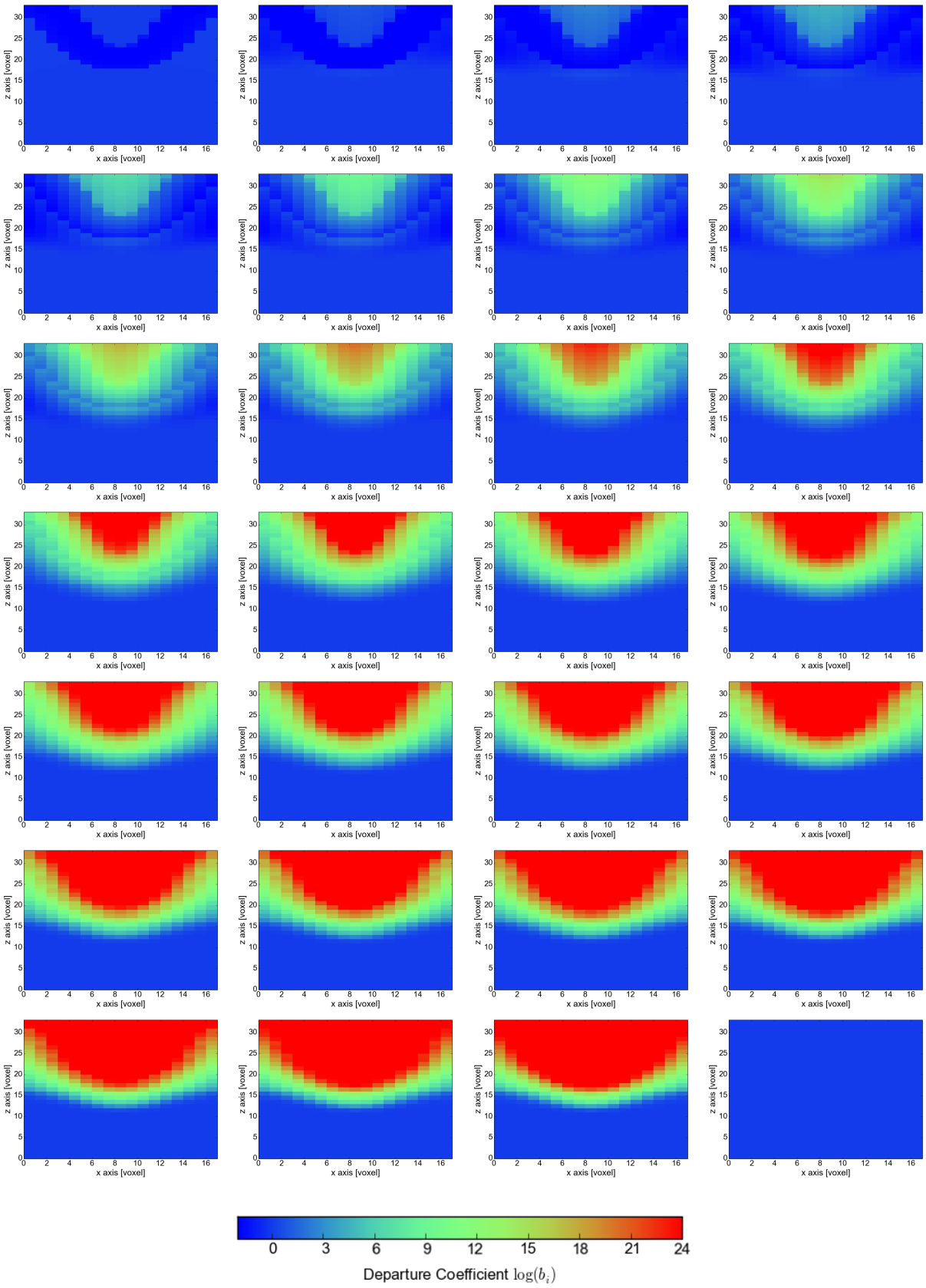

Figure 5.21: **Model B**: Departure coefficients for all 27 super levels shown as a color coded vertical slice through the center of the voxel grid and the anomaly. Upper left corner is super level containing ground state, lower right corner is continuum level.

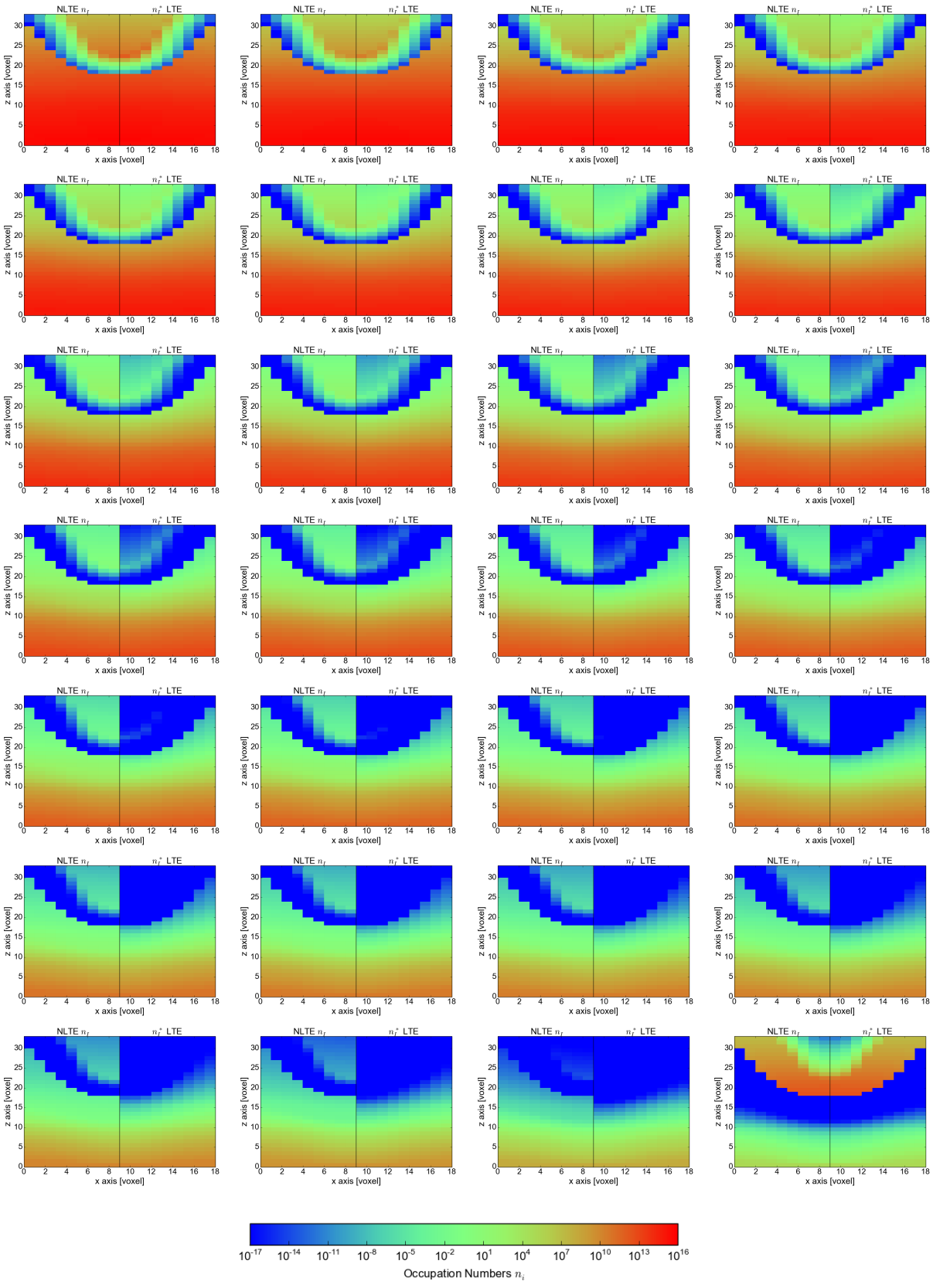

Figure 5.22: **Model B**: NLTE occupation numbers n_I compared to LTE occupation numbers n_I^* for all super levels. Left half of plots is NLTE, right half is LTE. Upper left corner is super level containing ground state.

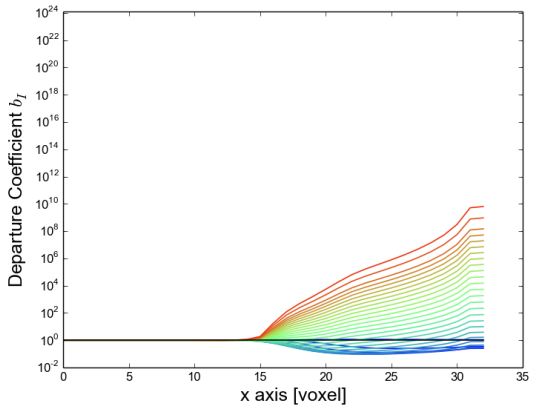

(a) Model A: grid corner

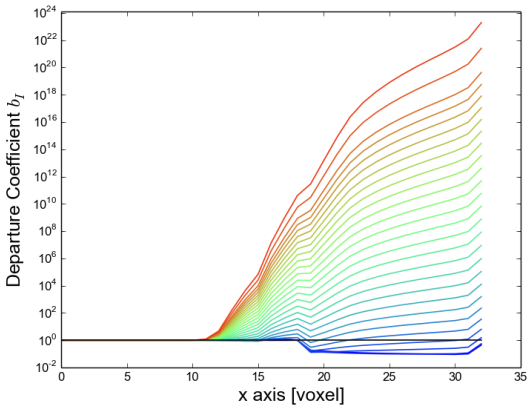

(b) Model A: center

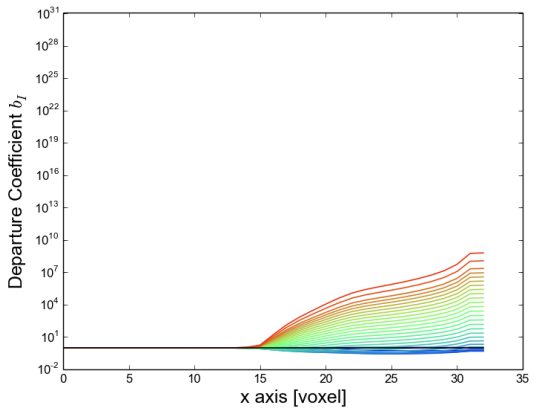

(c) Model B: grid corner

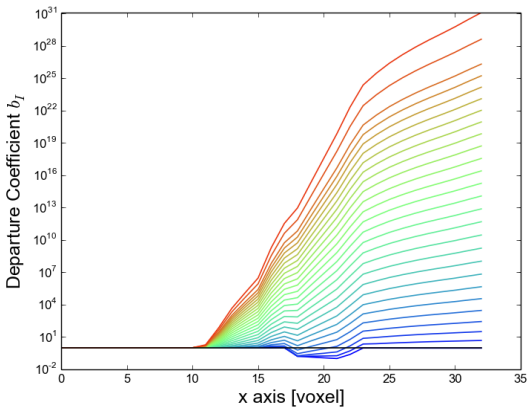

(d) Model B: center

Figure 5.23: Departure coefficients for a vertical column of voxels located within the center of both anomalies as well as at the very corner of the grid in both cases, as far away from the anomaly as possible.

effects are strongest for levels of high excitation energy, which show a higher population in the NLTE results.

In LTE, levels of higher energy are almost unpopulated in the cool regions of the atmosphere, where the local ambient temperature is not high enough to excite the CO molecules to these levels. In NLTE, however, the occupation numbers for all levels are determined both by the temperature and by the radiation field. As the temperature anomaly resides within an optically thin region of the atmosphere the local conditions have only a limited influence on the radiation field. The radiation field is dominated by radiation from deeper, hotter layers of the atmosphere. Thus, the mean intensity is high enough to excite the CO molecules to levels that would be nearly unpopulated without the radiation field's influence.

This effect is strongest in the coldest regions of the temperature anomalies, where the ambient temperature causes the lowest possible population of these levels. This can be seen by comparing Models A and B. While the upper levels are depopulated in LTE in both models, Model B also shows a depopulation within the anomaliy's core that is not seen in Model A with its higher core temperature.

5.2.2 3D Opacity Structure and Optical Depth

The changes to the occupation numbers of each level leads to different opacities accordingly, which are shown in Figures 5.24 and 5.25 for several wavelengths points for one of the CO lines of the $\Delta\nu = 1$ band at $\lambda_{\text{line}} = 48192.46$Å for both models. The left sides of the figures show the LTE opacities while the right sides show NLTE opacities obtained with the head-energy distributed super level method after 30 iterations.

In general, the opacities depend strongly on local temperature in both models. The temperature anomaly is clearly visible as a zone of reduced opacity in the upper half of the voxel grid, at wavelength points that are close to the center wavelength of the CO line, while the influence on the opacity is negligible at the rim of the line. Comparing the NLTE opacities to the LTE opacities, we find that the strongest changes are in the very core of the temperature anomaly. In this region, the temperature is lowest, and the departure coefficients are highest.

While the line opacities decrease in the outer region of the anomaly, they increase in its center. In NLTE, this effect is even stronger, especially in Model B, where the core temperature is even lower and the anomaly has a greater depth. The transition from the inside region to the outside region becomes sharper and less washed out for the rim wavelength points of the line. Model B also shows an increased opacity for the second rim point of $\lambda = 48193.24$Å, which is not seen in the LTE opacities. In this way, not only the line depth, but also its width and possibly its shape are affected.

Model A shows something similar, as the increased opacity at the core of the anomaly also fades at the center wavelength, but the effect is not as pronounced, so that we can still see the general shape of the anomaly, but no opacity increase at its core at $\lambda = 48193.24$Å.

The optical depth of $\tau_\lambda = 1$ has been marked as a black line in the plots. Here, the optical depth has been calculated for characteristics that are perpendicular to the surface of the grid with an inclination angle of $\vartheta = \pi$, $\varphi = 0$ and, thus, $\mu = \cos(\vartheta) = -1$.

As can be seen, the apparent surface marked by the $\tau_\lambda = 1$ line mirrors the opacity

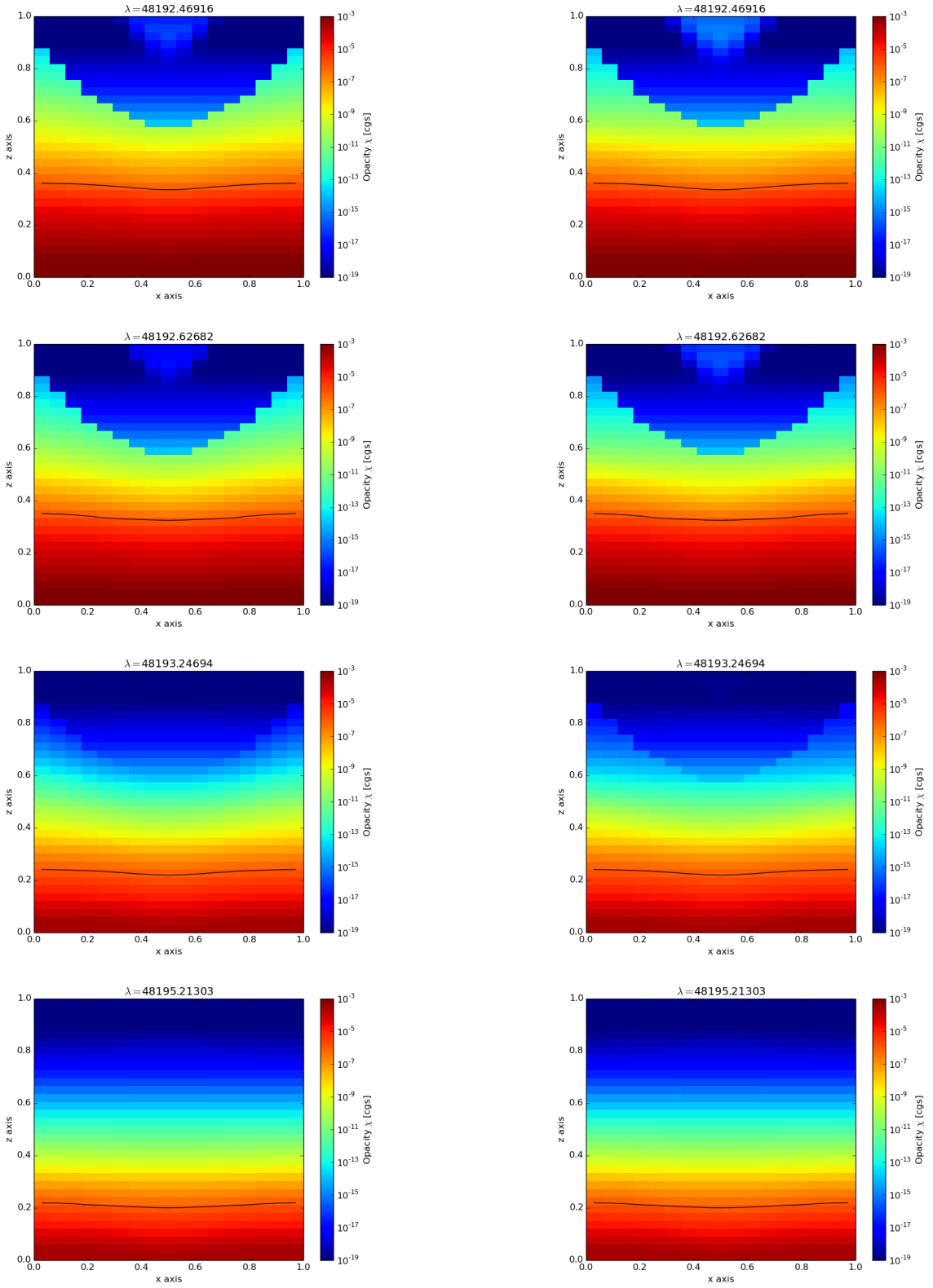

(a) LTE

(b) NLTE

Figure 5.24: Opacities for **Model A** for a CO line of the $\Delta\nu = 1$ band and the surrounding continuum. The black line marks the optical depth of $\tau = 1$ for characteristics of $\mu = 1$.

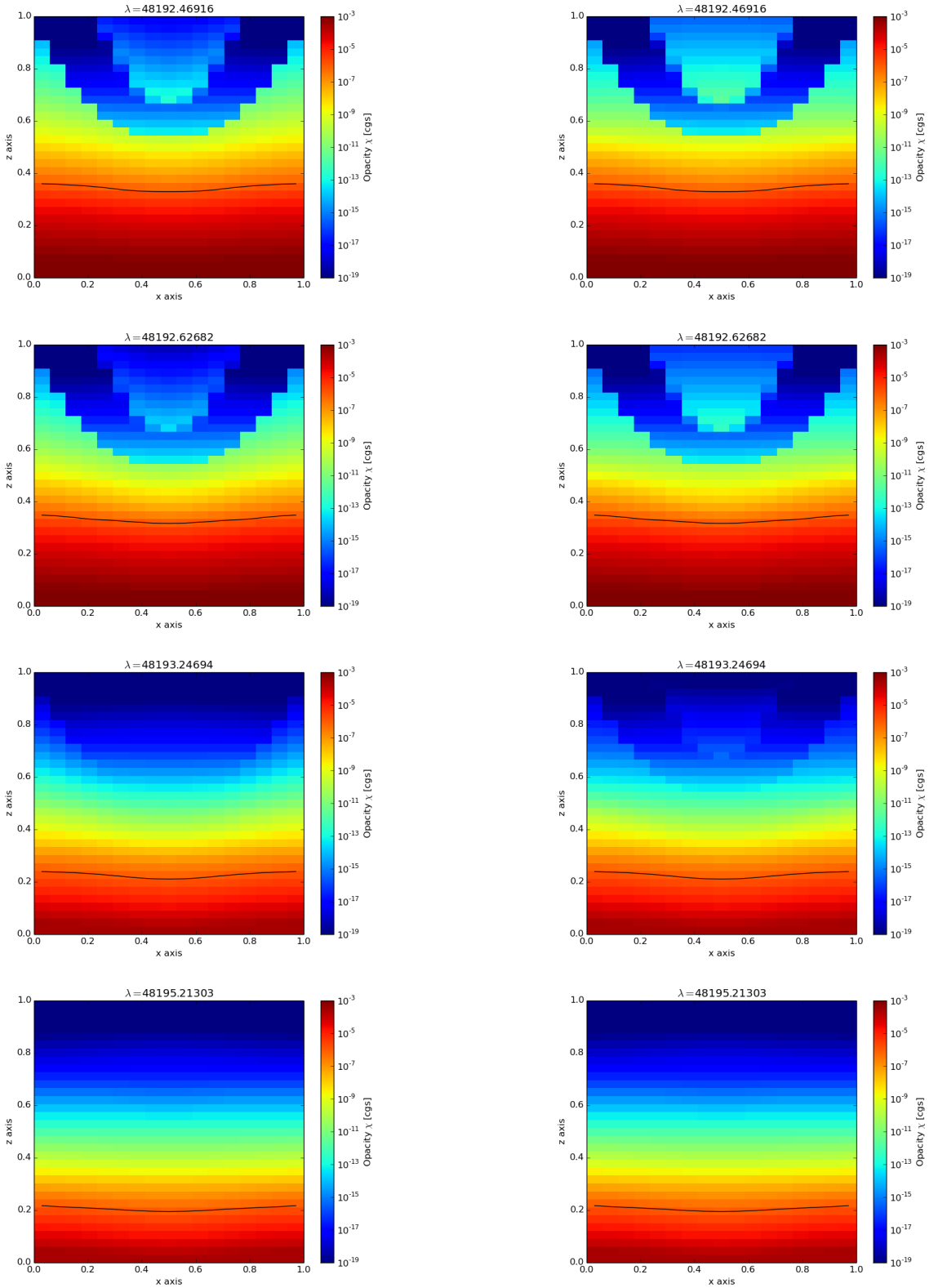

(a) LTE (b) NLTE

Figure 5.25: Opacities for **Model B** for a CO line of the $\Delta\nu = 1$ band and the surrounding continuum. The black line marks the optical depth of $\tau = 1$ for characteristics of $\mu = 1$.

structure. The strongest influence is the zone of reduced opacity at the rim of the temperature anomaly, so that $\tau_\lambda = 1$ is reached at a deeper level inside the atmosphere in regions directly below the core of the anomaly, compared to regions that are below the rim of the atmosphere, where the anomaly is shallower.

The exact shape is, by virtue of the wavelength-dependent changes of the opacity, equally wavelength dependent. In the center of the anomaly of Model B, below the region of increased opacity, the effect is somewhat limited so that the profile has a more or less constant area. Varying regions of increased as well as decreased opacity above form a plateau level that is not seen of other wavelengths, were the core of increased opacity does not exist. However, the profile varies only very slightly between LTE and NLTE opacities, since most of the NLTE effects are found in the optically very thin regions of the atmosphere.

In Model A, the central region of increased opacity is missing due to the higher core temperature, so that no plateau forms.

Outside of the line wavelength, the opacity is lower in general, and the continuum opacity is less sensitive to temperature, so that the $\tau = 1$ line recedes deeper into the atmosphere. The effects on opacity are much less pronounced here, so that the profile of the $\tau = 1$ line is, while still curved, not as distinct. The continuum is not affected by NLTE effects, since no NLTE continuum opacities are included in the simulation. Small effects seen are due to adjacent CO lines.

5.2.3 3D Effects to the Flux within the Atmosphere

The flux is redirected into the temperature anomaly and follows the temperature profile of the spot. Radiative energy flows from hotter regions to cooler regions. The magnitude of the flow is, therefore, affected by the opacity structure of the anomaly, which can be seen by the way the flux behaves differently for different wavelength points and for the different temperature and opacity structures of models A and B. This effect was shown in detail for instance in Berkner [2011] and Berkner et al. [2013].

This effect is shown in Figures 5.26a and 5.27a, where the x and y components of the flux in a xy-plane is depicted at about two thirds of the grid's height, in the lower region of the temperature anomaly for both models at $z = 20$. Each vector shows the horizontal flux within one voxel, where all vectors of each plot have been scaled, so that the largest flux within the plane is equal to a vector length of the width of one voxel. In this way, the vector length in each plot can not be compared directly, but only shows the qualitative differences of the flux for different wavelengths points.

In Model A, the flux is redirected most strongly in the center of the anomaly. Due to the fact that the temperature differences to the outside are already very small at this level of the atmosphere, this is not overly surprising. Furthermore, this effect increases for wavelength points close to the line center, where the changes in temperature also cause a different opacity structure. The effect is also seen for wavelength points outside the center of the line. However the redistribution of flux into the anomaly is not that much stronger in the center of the anomaly, compared to its rim.

In Model B the anomaly is still larger at this level, so that the redirection is evenly spread over the entire grid and the changes between different wavelength points are not as evident.

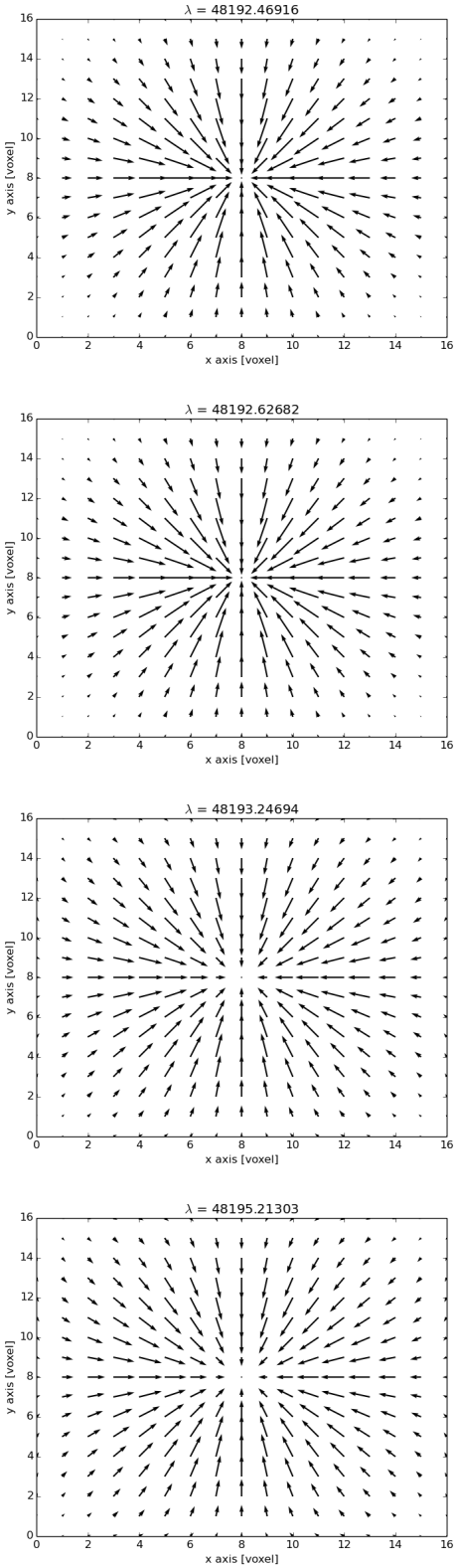

(a) NLTE Flux $\vec{F}_{\mathrm{NLTE}}$

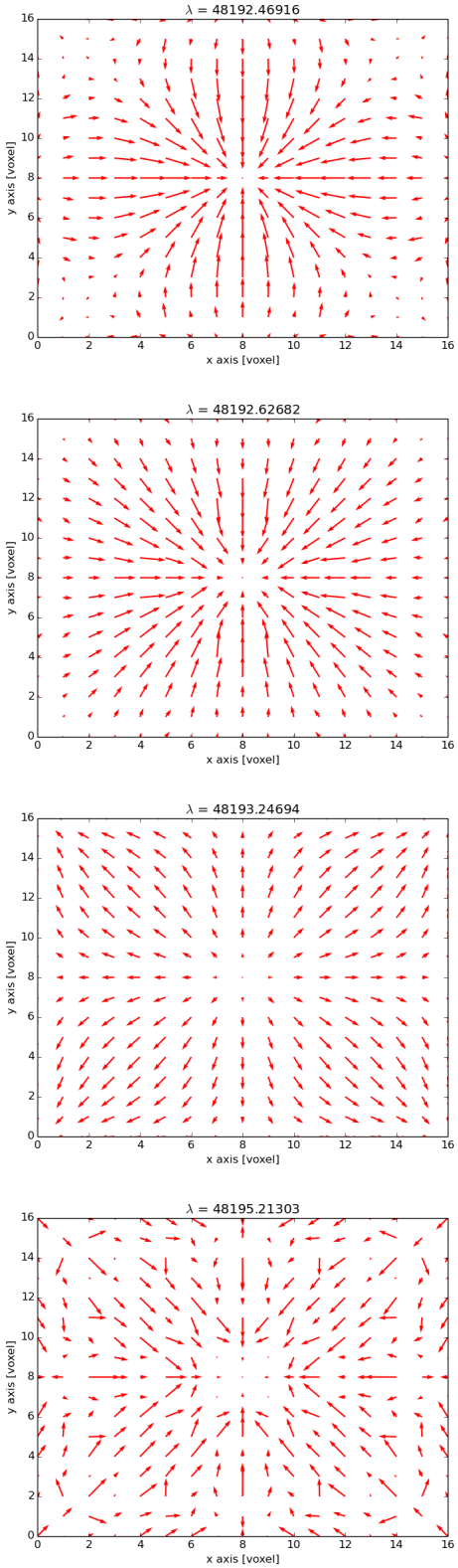

(b) Difference to LTE $\vec{F}_{NLTE} - \vec{F}_{LTE}$

Figure 5.26: **Model A** Horizontal Components of the Flux F_{xy} for super level NLTE calculation as well as difference between NLTE and LTE. Vectors have been scaled for each part of the figure separately.

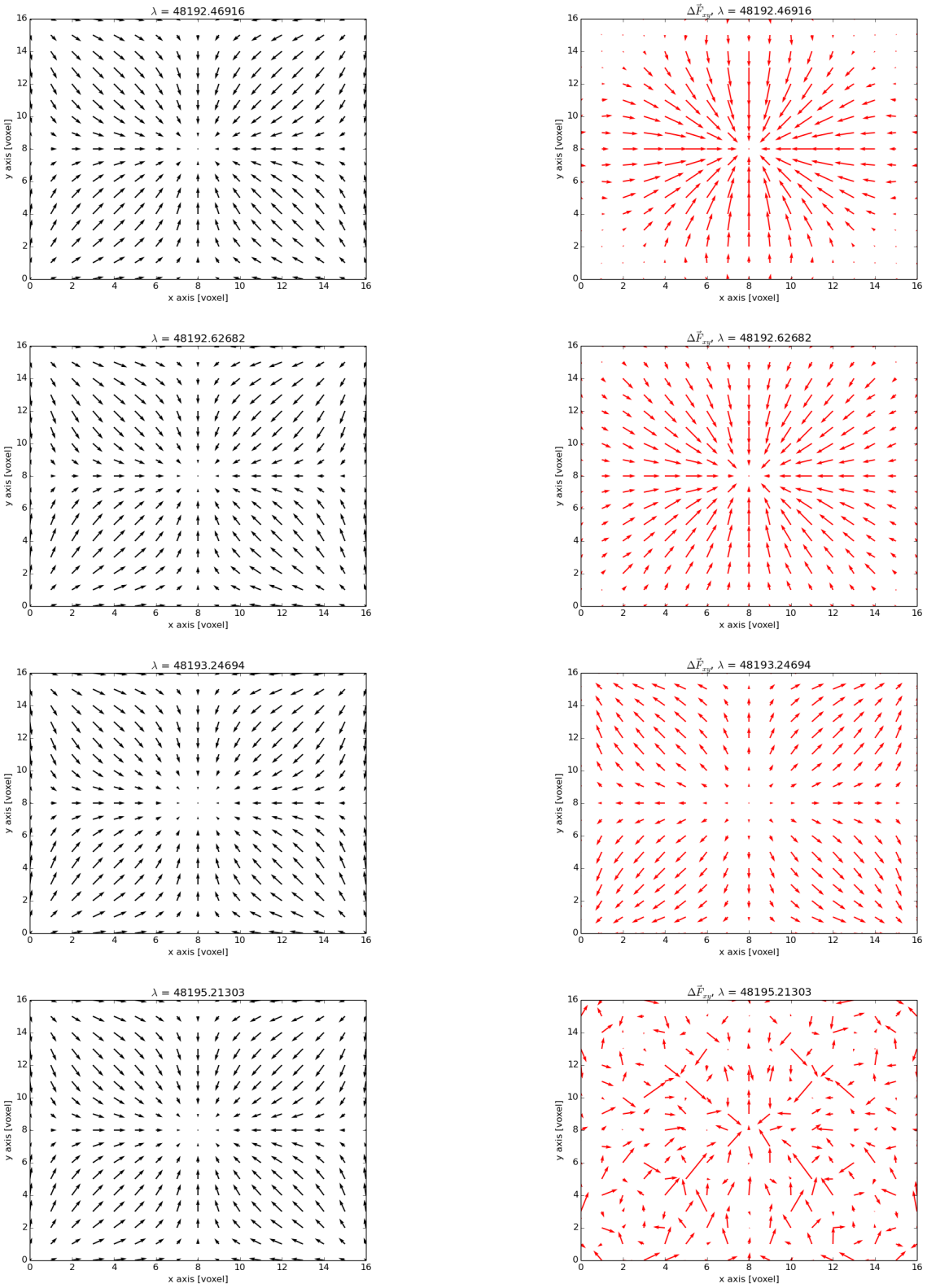

(a) NLTE Flux $\vec{F}_{NLTE}$

(b) Difference to LTE $\vec{F}_{NLTE} - \vec{F}_{LTE}$

Figure 5.27: **Model B** Horizontal Components of the Flux F_{xy} for super level NLTE calculation as well as difference between NLTE and LTE. Vectors have been scaled for each part of the figure separately.

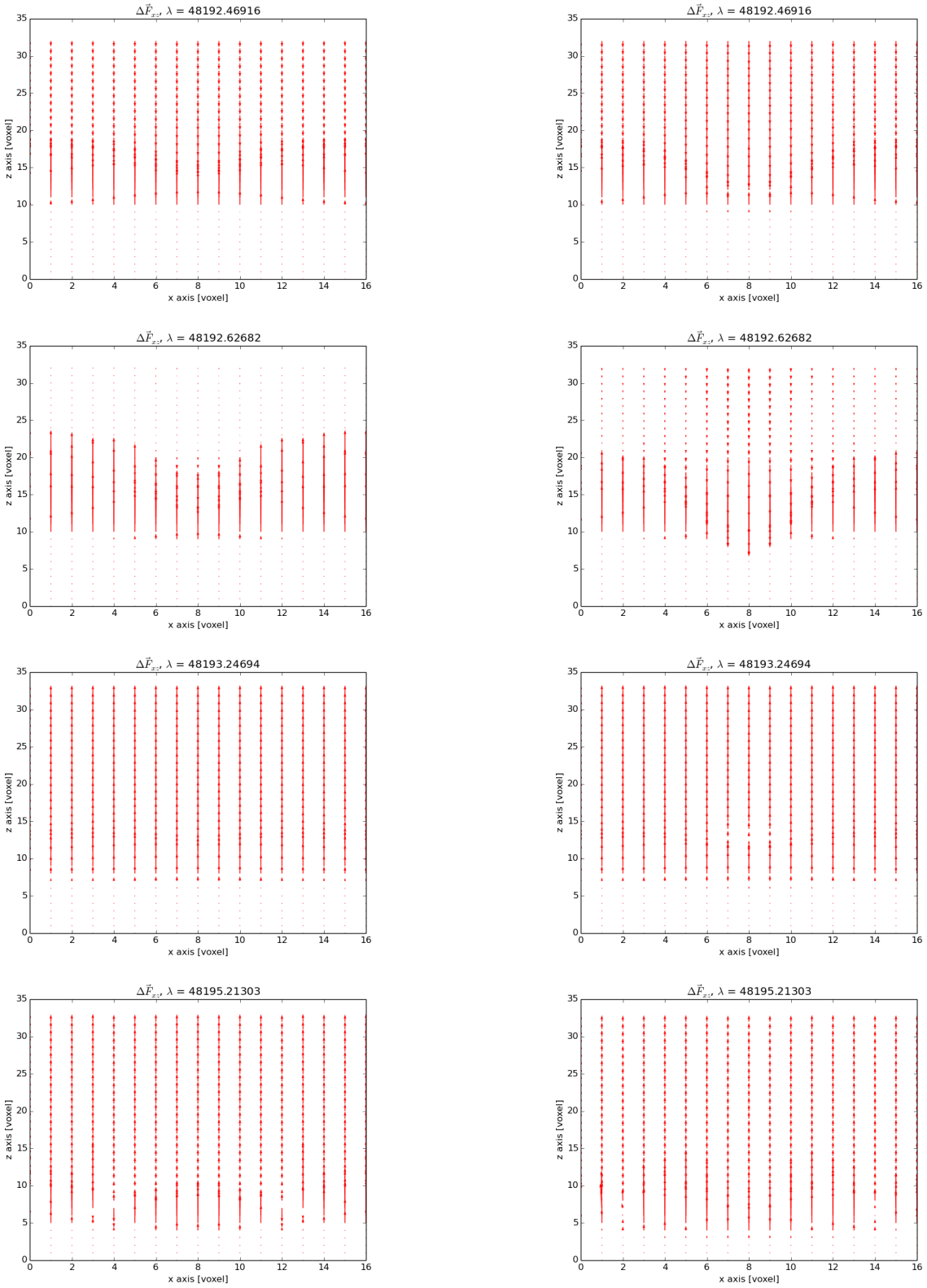

(a) Model A (b) Model B

Figure 5.28: Difference in horizontal and vertical Flux F_{xz} between NLTE and LTE for both Models. Length of Vector is scaled for largest vector in each figure.

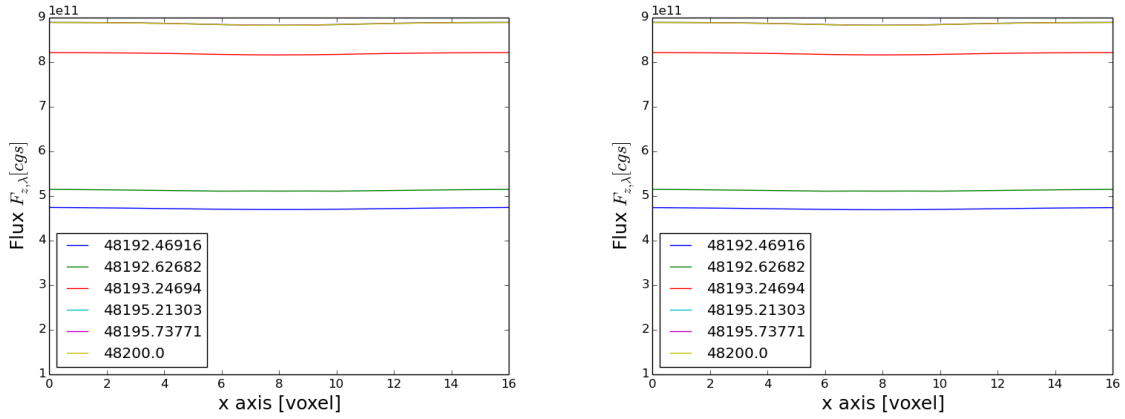

(a) LTE (b) NLTE

Figure 5.29: **Model A** Outward flux for different points of the surface of the grid shown for different wavelength along a profile through the center of the anomaly.

It is useful to compare the NLTE Flux to the LTE Flux, which is shown in Figures 5.26b and 5.27b for the lateral flux, as well as in Figure 5.28 for the vertical flux. The NLTE effects change the direction of the flux, at least to some degree, though both the flux and the change to the flux are still primarily directed outward.

All wavelengths points that are close to the central line wavelength show an increased redistribution of flux into the spot that is stronger in the core of the anomaly and almost non existent at the rim. This leads to an increase of the vertical flux below the spot compared to LTE conditions, but a decrease within the spot. In Model A, this effect is strong at the central line wavelength, but the differences in flux are confined to an increased flux below the spot at the wavelength point at the rim of the line.

Model B shows a small decrease in flux in the core of the anomaly even outside the line wavelength and a small zone were the outward flux is reduced even below the lowest reaches of the spot.

For the wavelength points between CO lines, the changes to the flux are orders of magnitude smaller than inside the lines, and the direction of the redirection is more or less erratic in the horizontal direction. Most of the changes seen are caused by numeric noise. The NLTE effects for those wavelength points are still there, due to the two distantly overlapping CO lines in the vicinity, but the opacity at this point is hardly affected at all, so that no clear structure forms. The vertical flux is increased slightly for most voxels, but the effect is smaller than for the center line wavelength.

Unfortunately, the resulting fluxes show an influence of the periodic boundary grid, making it obvious that the anomaly is too close to the rim and thus interacts with itself. However, to circumvent this completely, the simulation grid would have to be considerably larger than the spot, which would severely increase the computational demands or limit the spatial resolution within the grid.

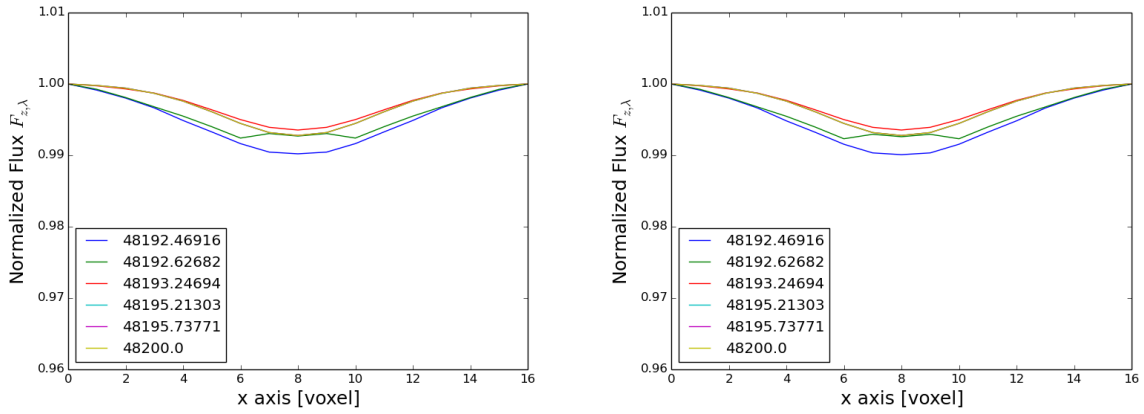

(a) LTE (b) NLTE

Figure 5.30: Outward Flux profile for Model A. Each line represents a different wavelength point. The Flux has been normalized to the Flux at the rim of the grid for each wavelength point.

5.2.4 Resulting Spectrum

The resulting surface profile for several different wavelengths points of Model A are shown in Figure 5.29 for both LTE and super-level NLTE. Here, line wavelengths are affected differently, than continuum wavelengths. However, the changes between LTE and NLTE are quite small. In general, the lines are deeper in the LTE results, but the contrast between inside and outside of the spot is smaller in the NLTE calculations. This is even more apparent if the surface profile is normalized to the outward flux at the rim of the grid, as to better show the influence of the anomaly, which is shown in Figure 5.30.

The surface flux profile is highly dependent on wavelength. For individual line center wavelengths, the profile is deeper and wider, so that the overall anomaly has a higher contrast compared to the outside. For wavelength points at the rim of the line, the surface profile of the flux shows an inversion. The darkest parts of the anomaly do not coincide with the lowest temperature, but are situated at the rim of the core. This is caused by a combination of the 3D temperature structure of the spot and the radiation forming region marked by the $\tau = 1$ line. While the $\tau = 1$ line is deeper inside the atmosphere, this also means that it recedes below the maximum depth of the spot, where the temperature is higher, compared to the regions that are seen at the rim of the anomaly.

The results for Model B are shown in Figures 5.31 and 5.32. The higher temperature difference at the core of the anomaly produces a higher contrast between points directly above the structure and the rim of the grid. Apart from the increased size due to the larger and cooler anomaly, NLTE effects are quite similar to those of the other model. The line depth is increased primarily at the center of the strongest line, but at the same time, the contrast between the inside and the outside of the anomaly is lost. In this way, the NLTE effects act as an equalizer, redistributing the total effect of the temperature variation over a wider area.

The main difference between the flux profiles of both models is the fact that the center of the anomaly shows the greatest contrast to the outside at all wavelength points in Model

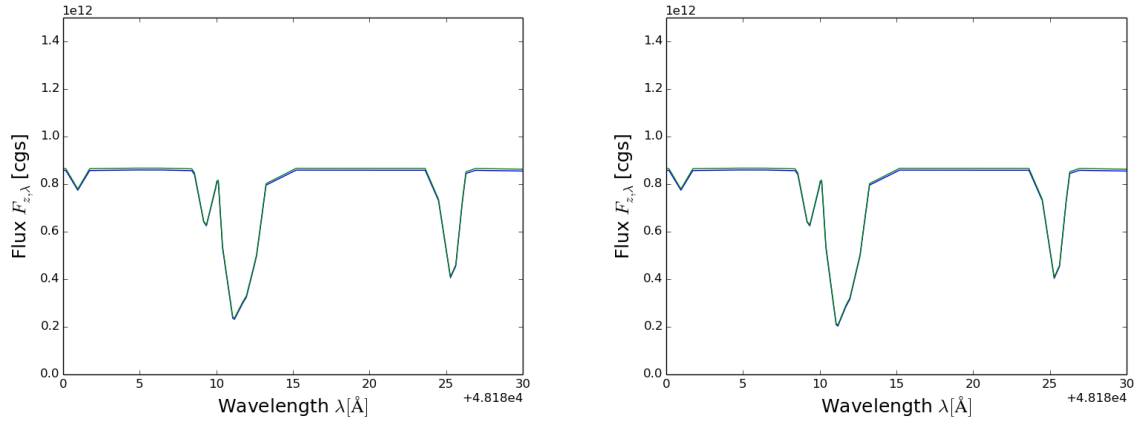

(a) LTE (b) NLTE

Figure 5.31: Outward Flux for part of the $\Delta\nu = 1$ CO band. Blue line is outward Flux in the center of the grid over the core of the anomaly of Model B, green line is outward flux at the rim of the grid, far from the anomaly.

B - the reversal in the center of the profile, as seen in Model A, no longer appears. This is an effect of the different temperature structure and increased maximum depth of the spot. Instead, a ring of constant flux forms at the edge of the anomaly caused again by the combination of temperature profile, opacity, and $\tau = 1$ depth for different parts of the atmosphere.

5.2.5 Conclusions

The results show very high departure coefficients caused by a strong radiation field and small collisional rates within the parametrized temperature anomaly, which is consistent with the results of the previous calculations. However, these effects are mostly limited to the optically thin region of the atmosphere, as far as the wavelength bands for the CO lines is concerned.

Nevertheless, the super level NLTE results show a redirection of flux into the cooler part that is not seen in the LTE calculation, at the same time spreading the darkening of the stellar surface over a wider area. Additionally, several CO lines are changed in depth and shape as different lines and different wavelength are affected depending on the CO levels they are coupled to. The effective change to an observable spectrum might be small, but it stands to reason that a large number of small temperature variations can add up to a significant NLTE influence on the spectrum, which is not possible to simulate otherwise.

Furthermore, even though the direct influence on the outgoing spectrum is small, the fact that NLTE effects act as an equalizer between the inside and the outside region is a much more significant result. These results have been obtained with a static atmosphere structure, however, stellar atmospheres are ever changing. If it were possible to include these results into a radiation hydrodynamics simulation, the influence could be significant as the changes to the flux within the atmosphere influence the temperature structure

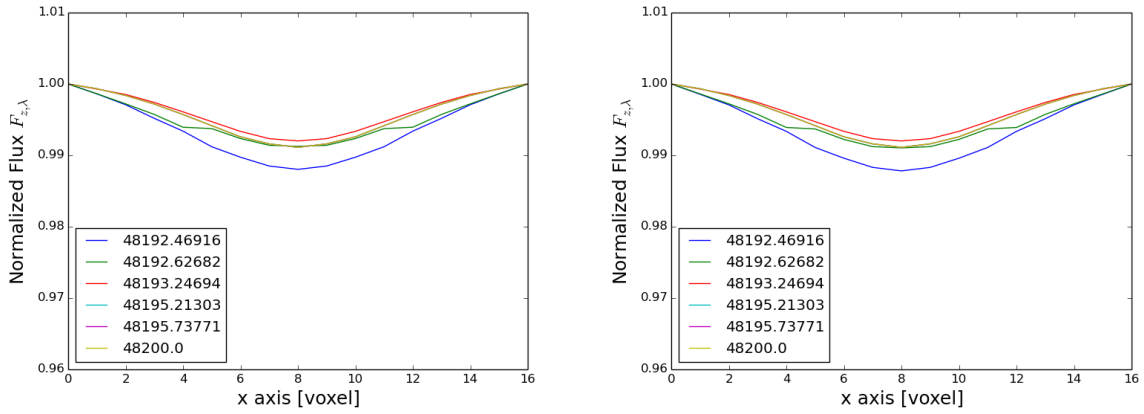

(a) LTE (b) NLTE

Figure 5.32: Outward Flux profile for Model B. Each line represents a different wavelength point. The Flux has been normalized to the Flux at the rim of the grid for each wavelength point.

itself.

A zone of reduced temperature always results in a flow of energy into the cool zone that will, sooner or later equalize inside and outside temperatures, at least to some degree, depending on the physical reason for the zone of low temperature that acts against this process. The NLTE effects shown here spread the effect of the low temperature zone over a larger volume but reduce the magnitude of its influence on each individual voxel. Thus the size of the anomaly is changed for all radiative effects and the differential between the inside and the outside is lessened. In this way, NLTE effects might act as one of the forces supporting the presence of the anomaly and slowing down its possible dissipation.

5.3 Parametrized Model for Temperature and Pressure

So far, only changes to the temperature within a designated part of the stellar atmosphere were considered. However, in most cases, a change in temperature usually coincides with a change in pressure. The most noticeable effect of changes to the pressure structure should be the changes to electron density and collisional rates, where high collisional rates will force a return to LTE conditions.

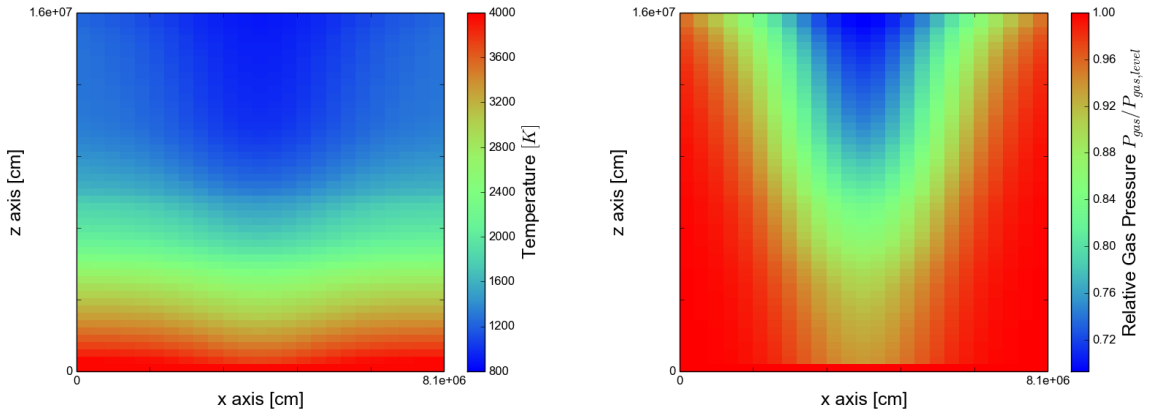

(a) Temperature

(b) Relative Gas Pressure

Figure 5.33: Temperature and pressure structure for **Model C**. Gas pressure is shown as normalized to the gas pressure at the same level without the pore.

To test, how the pressure structure influences the NLTE conditions, Model C was set up. The model uses the same basic atmosphere structures as Models A and B, but the horizontal size of the parametrized temperature structure has been reduced to decrease the boundary problems that were seen and the pressure was reduced with the same factor as the temperature. The resulting temperature and pressure structure is shown in Figure 5.33. Model C, thus, uses a core temperature difference of $\Delta T_0 = -500$ K, a radius of $r_0 = 3 \times 10^6$ cm, a lower boundary of $z_0 = 9 \times 10^7$ cm and a scale depth of $z_{\text{scale}} = 1.4 \times 10^8$ cm. The model was also calculated with an increased spatial resolution for $25 \times 25 \times 49 = 30625$ voxels and 48×48 solid angle points for the radiative transfer solution.

As can be seen in Figure 5.34, the CO density shows a similar structure compared to the previous models, where the differences can be explained by the difference in temperature structure. However, while the electron density is still extremely small within a zone below a certain temperature, where the temperature is too low for the existence of free electrons, this zone is smaller than in the previous models and is limited to the coolest parts of the anomaly, while the electron density is merely reduced in its outer parts.

The resulting departure coefficients for this model can be seen in Figure 5.35. The departure coefficients show a similar behaviour, as in the two previous models, where most changes can be explained by the differences in the temperature structure.

The departure coefficients deviate from unity where the electron density is lowest, and in the region that was shown to be devoid of free electrons, the departure coefficients of super levels consisting of levels of higher excitation energy are still extremely high, showing an extreme overpopulation, similar to the previous models. This is, of course, caused by

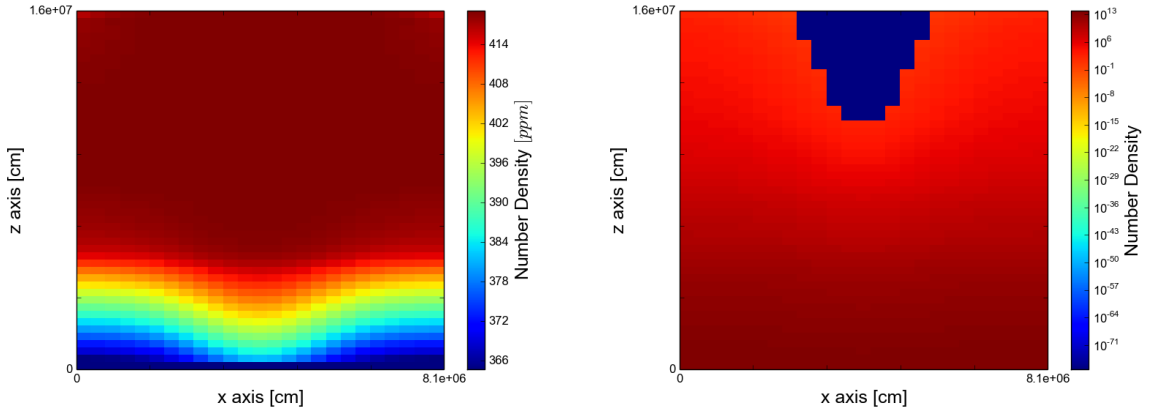

(a) CO Density

(b) Electron Density

Figure 5.34: Electron and CO number densities for a parametrized structure for temperature and pressure.

the collisional rates, which are linear in electron density and, thus, are almost zero in regions where the electron density is very low. The level populations are determined by radiative processes. As the region is also optically thin, the radiation field connects spatially distant regions of the atmosphere, in particular, the cool regions within the anomaly with the hot regions outside and below so that strong NLTE effects are seen. These effects are stronger for higher energy levels, as they would be almost unpopulated in regions of low temperature in LTE.

This suggests that to adequately calculate molecular NLTE opacities in regions of very low temperature, it is not advisable to limit the calculation of the collisional rates merely to electron collisions. Here, electron collisions will be scarce due to the low number of free electrons. As such, it would be necessary to treat collisions with hydrogen and heavier atoms as well to simulate zones of very low temperatures correctly. This is undoubtedly the case in general, but in regions with low electron density it is particularly obvious. Furthermore, this alludes to the fact that ionization needs to be treated correctly as well as this will have an influence on the electron densities.

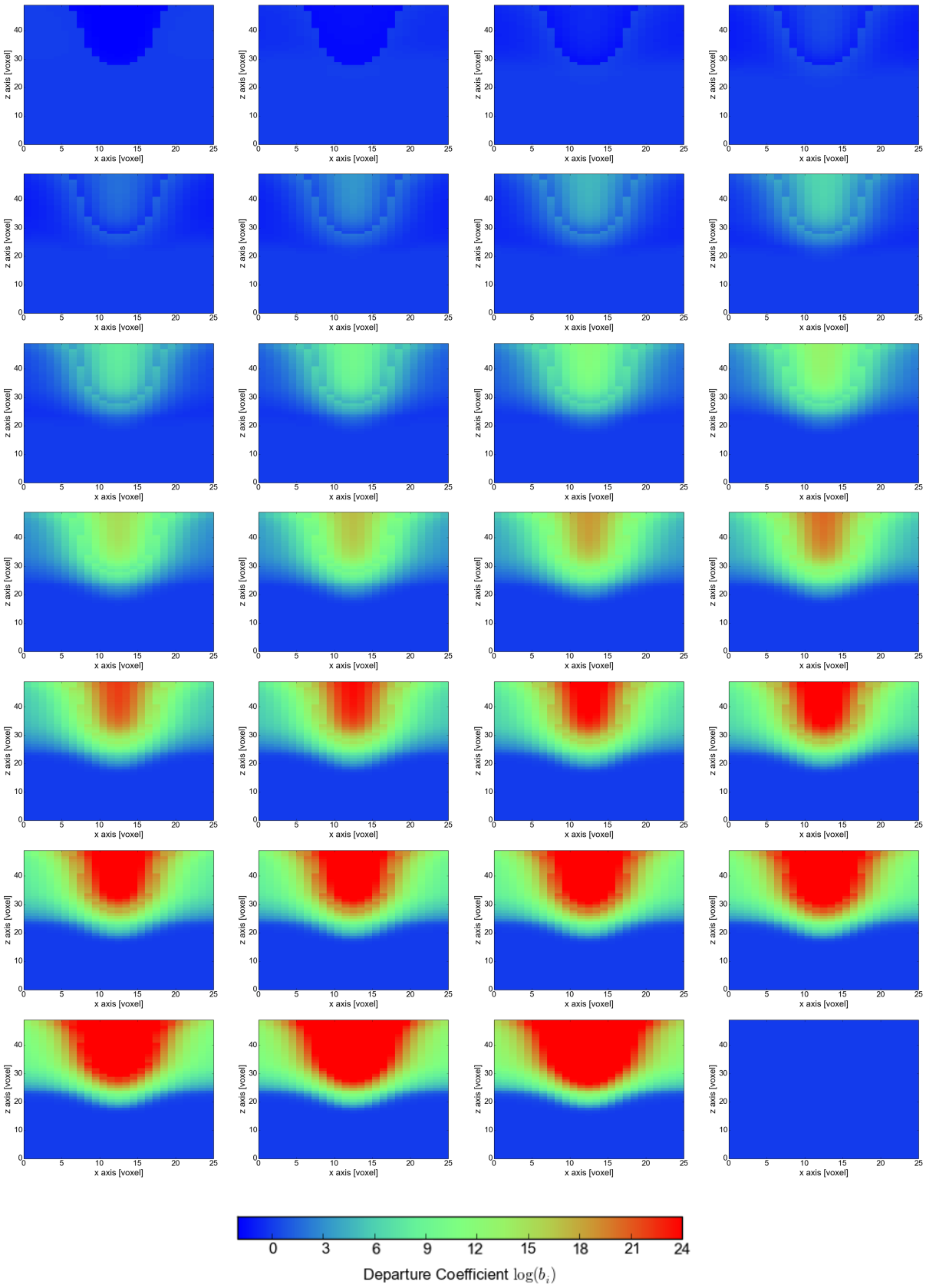

Figure 5.35: **Model C** Departure Coefficients for all 27 super levels shown as a color coded vertical slice of the voxel grid. Upper left corner is super level containing ground state, lower right corner is continuum level.

5.4 Solar Pore Model

For the fourth model, different atmospheric conditions were used. Thus far, all models were temperature anomalies within a cool stellar atmosphere. The upper region of these atmospheres already feature strong NLTE effects even without the presence of the temperature anomaly, as seen in the spherical symmetric tests. The atmosphere structure for the fourth model was chosen so that the NLTE effects without the anomaly would be comperatively small so that a strong difference between the outside and the inside is expected. Even in LTE, this type of atmosphere strongly reacts to the inclusion of a cool region as the opacities change and, thus, the optically thin region of the atmosphere is shifted to a shallower depth at affected wavelengths.

In this way, this model can be used to investigate, how strong NLTE effects within a very limited region of a stellar atmosphere affect the global structure of the atmosphere. This model uses a stellar atmosphere that would be consistent with a solar-like G-type star, with $T_{\text{eff}} = 5700\text{K}$ and $\log g = 4.5$, where, usually, no strong NLTE effects for CO are expected in the photosphere.

The temperature anomaly included could be, for instance, a solar pore or a very small solar spot. The temperature difference compared to the quiet atmosphere has been chosen very high to create a strong flux into the atmosphere. The temperature structure was again taken from Berkner et al. [2013], with the following parameters: $\Delta T_0 = 2000\text{K}$, $r_0 = 3.5 \cdot 10^8\text{cm}$, $z_0 = 2 \cdot 10^9\text{cm}$, $z_{\max} = 1.8 \cdot 10^9\text{cm}$. However, as in the previous model, the pressure was adjusted with the same ratio as the temperature for each voxel.

The model was calculated for $25 \times 25 \times 49 = 30625$ voxel and 48×48 solid angle points for the radiative transfer solution. The resulting pressure and temperature structures are shown in Figure 5.36.

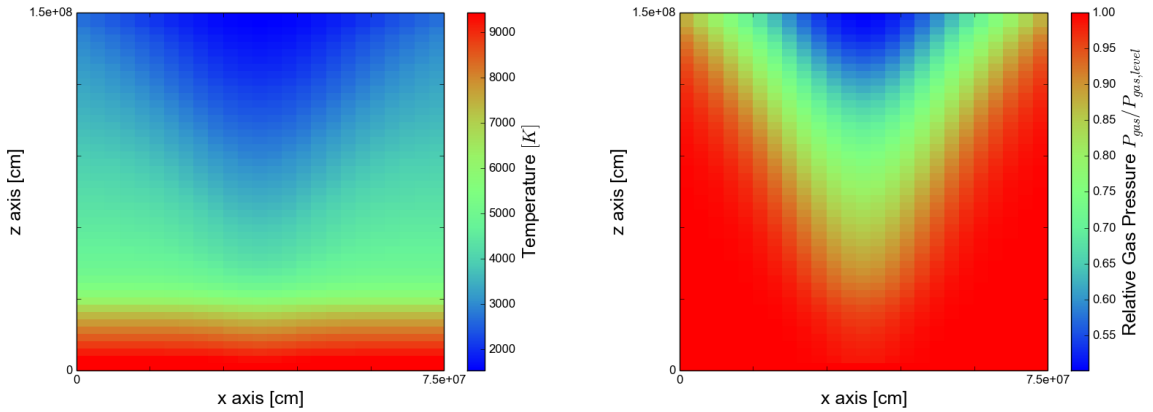

(a) Temperature

(b) Relative Gas Pressure

Figure 5.36: Temperature and pressure structure for a solar pore like structure in an G-Type stellar atmosphere. Gas pressure is shown as normalized to the gas pressure at the same level without the pore.

The CO and electron density are shown in Figure 5.37. Compared to the earlier models, the CO density is strongly influenced by the presence of the anomaly, due to the fact that

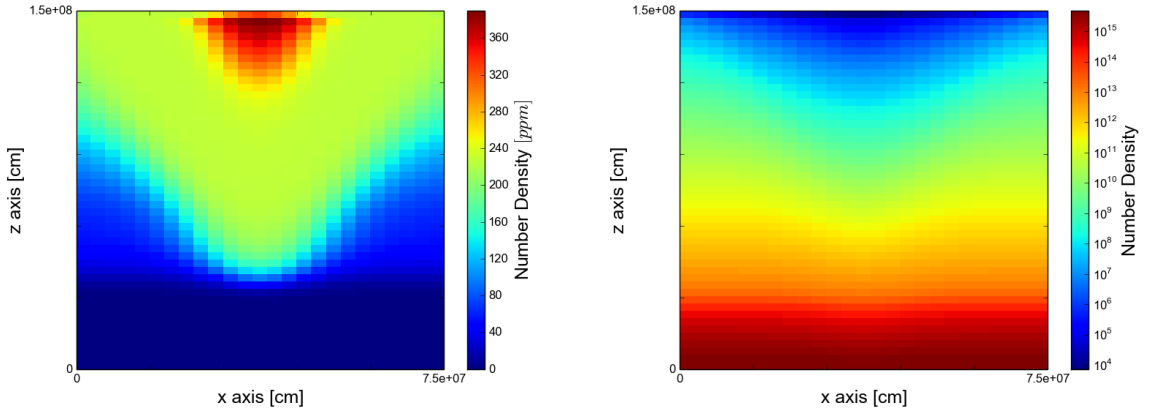

(a) CO Density

(b) Electron Density

Figure 5.37: Electron and CO number densities for a solar pore like structure in an G-Type stellar atmosphere.

the temperatures outside of the anomaly favour a fast dissociation[1] of CO, in particular in the lower layers of the atmosphere. However, even in the coolest parts of the anomaly, the CO density is lower than in the cooler atmosphere that was used in the previous models. The electron density closely follows the temperature and pressure profiles of the anomaly, which produces a zone with a comparatively low number of electrons in the core of the anomaly. However, there are free electrons in every part of the atmosphere as there is no zone where the free electron density vanishes completely.

5.4.1 Departure Coefficients

Figure 5.38 shows the departure coefficients for two vertical columns of the voxel grid - one situated in the center of the anomaly, where it has its lowest temperatures, and one at the edge of the grid, where the temperature anomaly has close to no influence on the temperature structure.

As can be seen, the departure coefficients in both columns are vastly different. Inside the anomaly, levels of lower energy are slightly depopulated while levels of high level energy are strongly overpopulated. This behaviour is very similar to the structure seen both in the spherical symmetric models of cooler atmospheres, as well as in the previous models with anomalies. However, compared to the cooler anomalies, there is no zone of strong depopulation of the lower levels. This can be explained by the fact that the electron densities do not drop as profoundly within this model so that the collisional rates are always unequal to zero and have some stabilizing influence.

Outside the anomaly, the temperatures are much higher than in the previous models. This leads to very different departure coefficients. First of all, the NLTE effects are confined to a slightly higher altitude compared to the region within the anomaly. Also we do not see the pattern of depopulated levels of low energy and overpopulated levels of high energy. In fact, quite the opposite is the case. Here, the super level containing the ground state is very slightly overpopulated with a maximum departure coefficient of $b_I = 1.37$

[1] currently not treated in NLTE

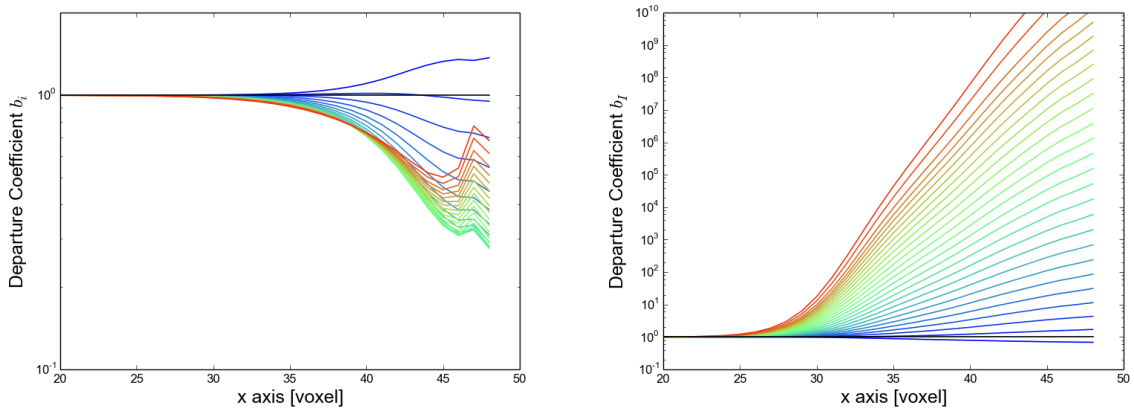

(a) Outside of Anomaly

(b) Inside the Anomaly

Figure 5.38: Departure coefficients b_I in a vertical column of the grid. The lowest parts of the grid have been omitted since there are no NLTE effects there.

at the top of the atmosphere, while all higher levels are slightly underpopulated with departure coefficients ranging between ≈ 0.2 and ≈ 0.95. In the intermediate levels, the levels of highest energy are underpopulated the most compared to LTE. However, in the upper reaches of the photosphere, the result is not quite as clear cut. While super levels of low and intermediate level energy show an increase in depopulation while approaching the upper boundary of the atmosphere, the levels of highest energy are depopulated less and show even a reversal of their departure coefficient, so that they are not depopulated as much as super levels of lower energetic levels.

Figure 5.39 shows the departure coefficients of all super levels for a vertical slice of the voxel grid. The NLTE effects again clearly follow the temperature and electron density in a similar way as before, where the departure coefficients are high in regions of low temperature and electron density and in general close to unity outside the temperature anomaly, while the lower levels are only slightly under populated.

A high resolution colourization of the super ground state is shown in Figure 5.41, where it is possible to see how the ground state is actually overpopulated, even if ever so slightly, outside of the anomaly, while it is underpopulated within its core. This zone of overpopulation is pushed deeper into the atmosphere below the sides of the spot, but vanishes completely below its core. Thus, the lower temperatures gradually insert NLTE effects deeper into the atmosphere and also reverse the effect from an over-population of lower states outside, to an under-population where higher super levels are over populated.

The super level occupation numbers shown in Figure 5.40 expand on this picture. As was obvious from the departure coefficients, NLTE effects have only a small influence on the highly populated levels of lower energy. The higher energetic super levels, however, show something else. While the level population decreases in LTE, as is shown in the right hand side of the plots for each level, since the temperature is no longer high enough to populate the level, this is not true in NLTE. The radiation field connects spatially separated parts of the atmosphere and equalizes the population densities between the inside and the outside of the anomaly. In this way, while the temperature profile of the

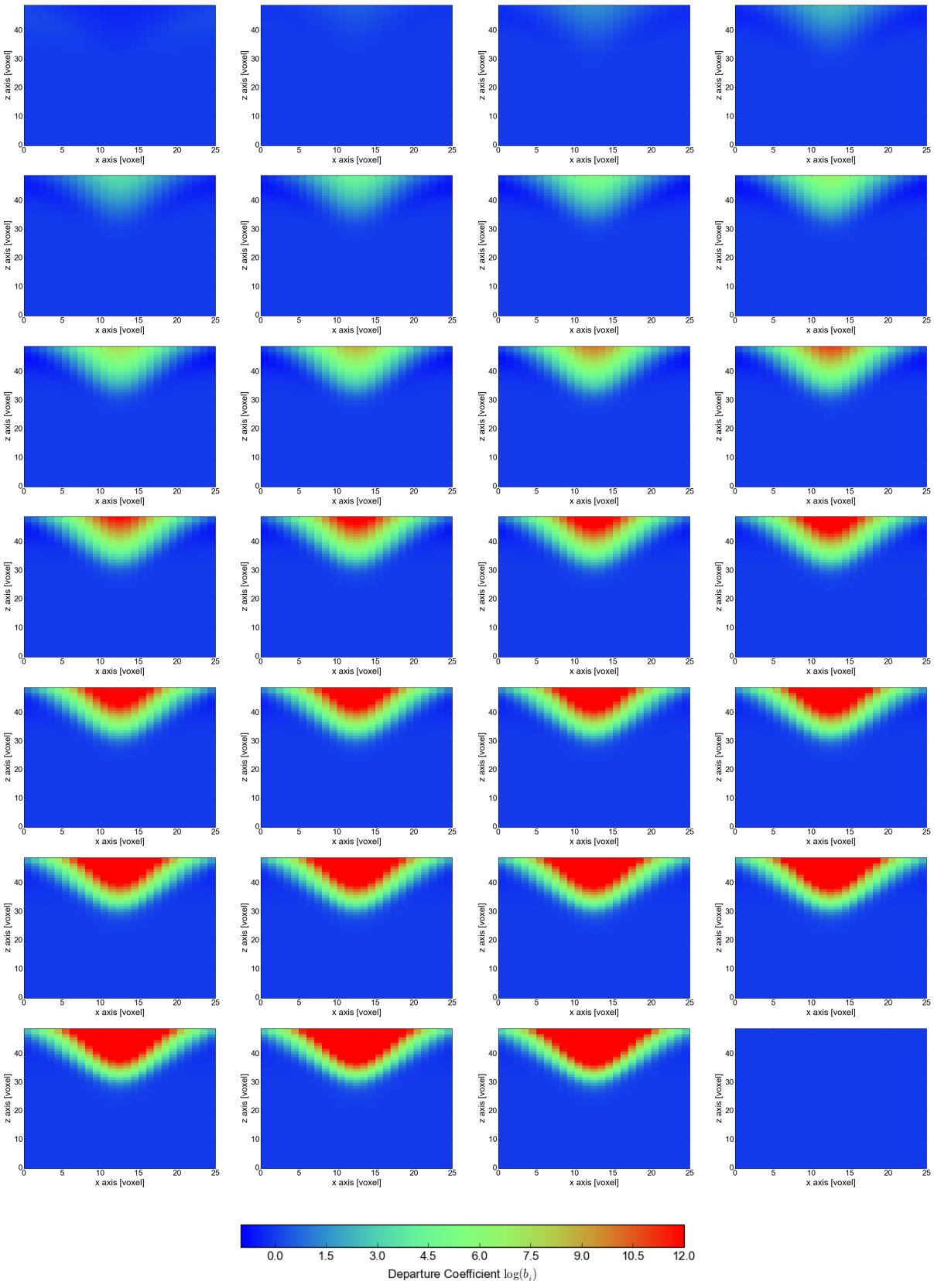

Figure 5.39: **Solar Model** Departure coefficients for all 27 super levels shown as a color coded vertical slice of the voxel grid. Upper left corner is super level containing the ground state, lower right corner is continuum level.

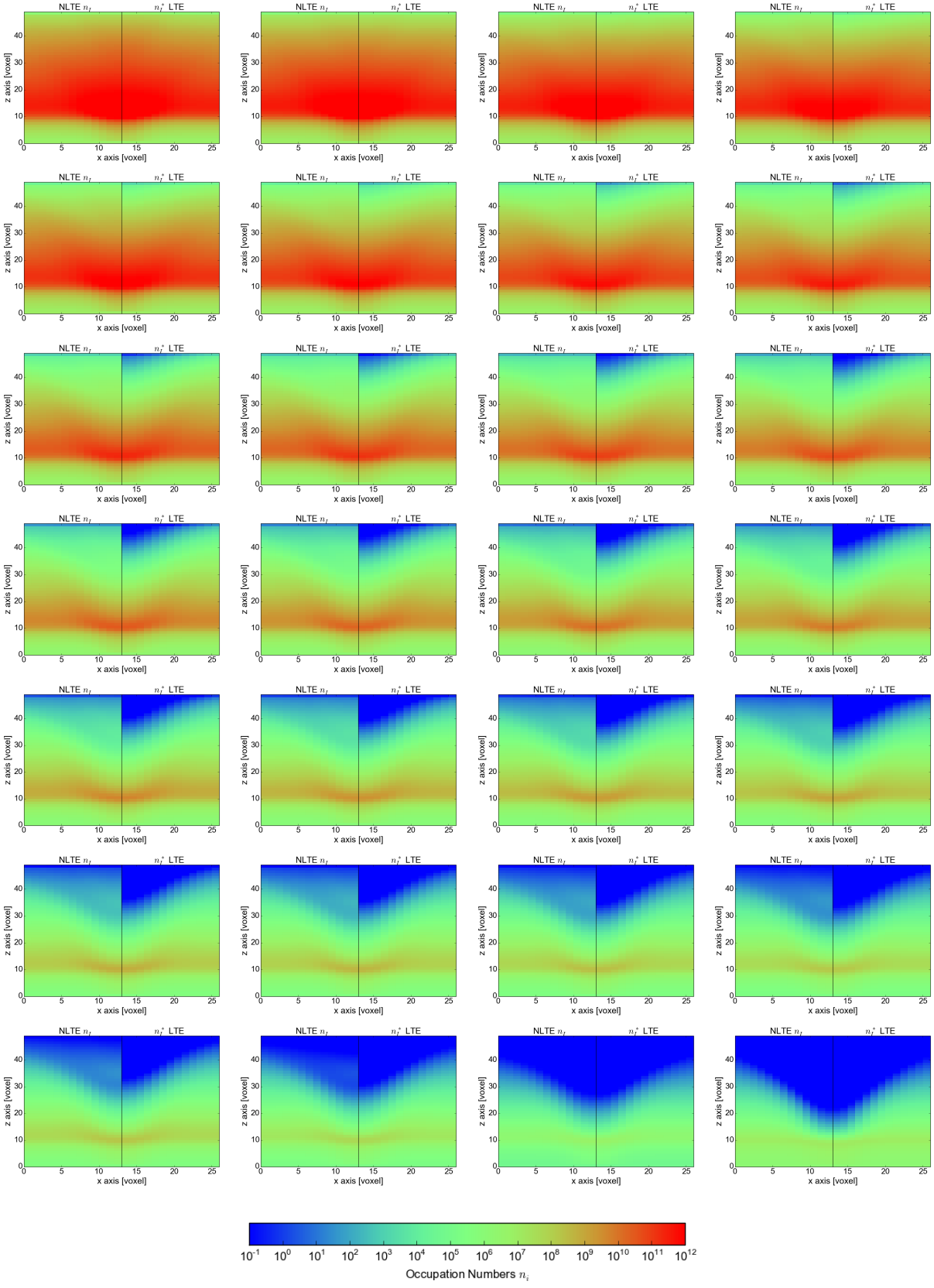

Figure 5.40: **Solar Model**: NLTE occupation numbers n_I compared to LTE occupation numbers n_I^* for all super levels. Left half of plots is NLTE, right half is LTE. Upper left corner is super level containing the ground state.

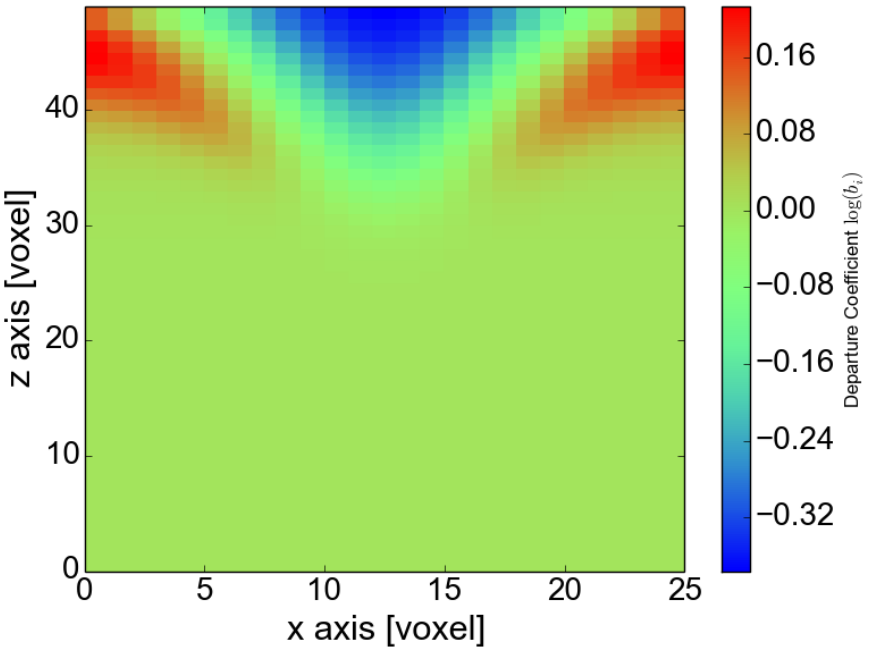

Figure 5.41: Departure Coefficient for the super ground state shown as a color coded vertical slice of the voxel grid.

anomaly is not completely overwhelmed in the NLTE occupation numbers, it is smoothed out, especially for intermediate levels. This effect also explains the zone of depopulation, which is seen outside of the region affected directly by the anomaly.

The effect is weaker in the lower reaches of the atmosphere, where it is counteracted by the temperature dependent collisional rates.

5.4.2 Effects on Opacity

The changes in temperature structure result in different opacities for all wavelengths both directly and indirectly through changes to the number densities of all atoms and molecules. The NLTE occupation numbers for each level cause additional changes to the line opacities for each CO line. The resulting opacities for a line wavelength, a wavelength point at the rim of a CO line, as well as a continuum point in the same wavelength regime are shown in Figure 5.42 for both LTE and NLTE.

For continuum wavelengths, the lower temperatures produce a zone of reduced opacity that follows the temperature profile of the anomaly and results in a slightly deeper $\tau = 1$ profile within the atmosphere, so that slightly deeper levels are dominant for the outgoing radiation. However, these deeper levels are still affected by the temperature structure, so that they are of roughly the same temperature as the region outside of the anomaly. In this way, it can be expected that the influence on the continuum is close to non existent.

Moving into the line, the opacity becomes dominated by the changes to the CO number densities, so that we see strong increases to opacity at the lower end of the anomaly, where there is almost no CO outside. The high CO density in the region of lowest temperature at the upper core of the spot-like structure creates another region of strongly increased

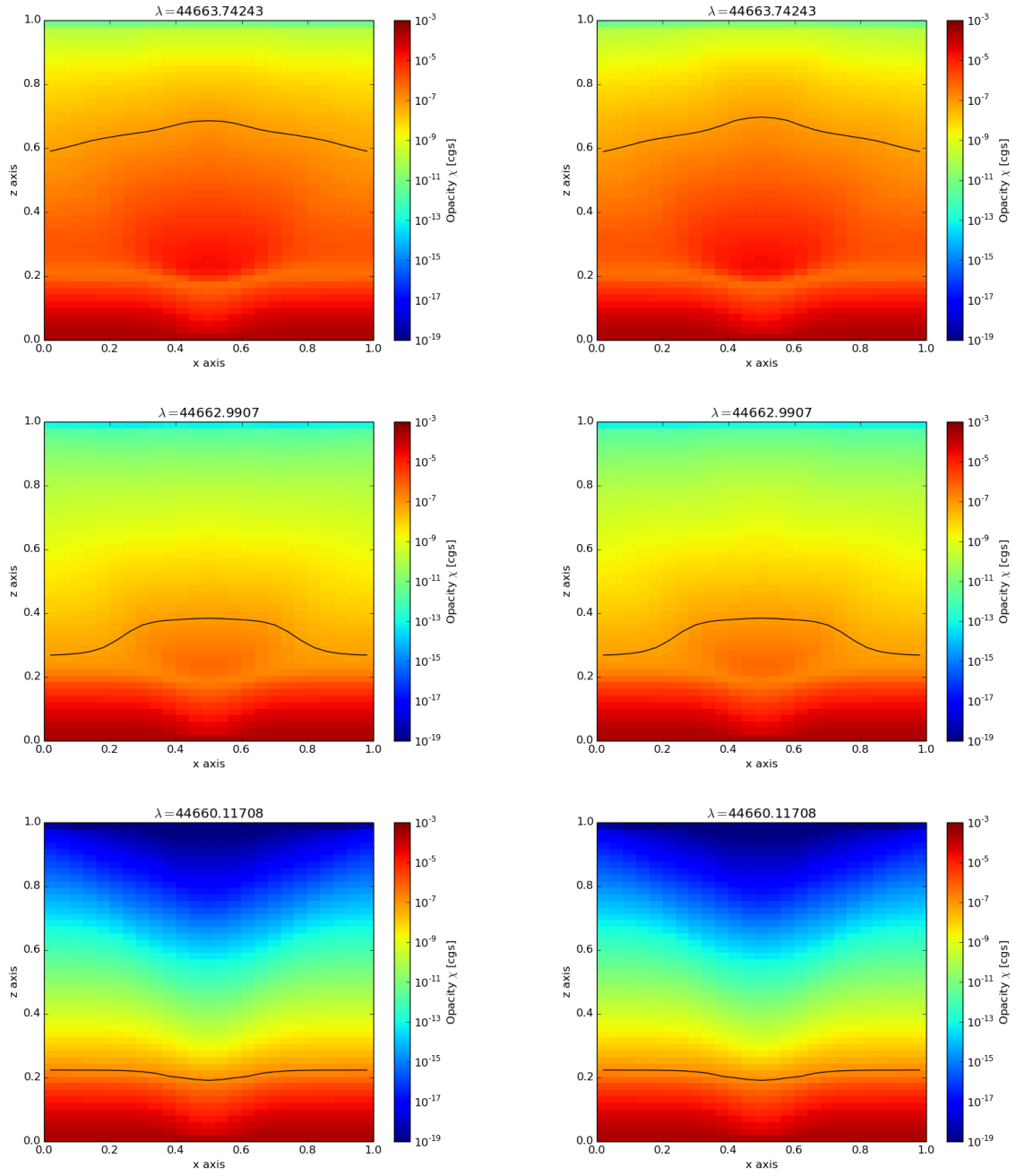

(a) NLTE Opacities

(b) LTE Opacities

Figure 5.42: Opacities for the Solar Pore Model for a CO line of the $\Delta\nu = 1$ band and a surrounding continuum point. The black lines marks the optical depth of $\tau = 1$ for characteristics of $\mu = 1$.

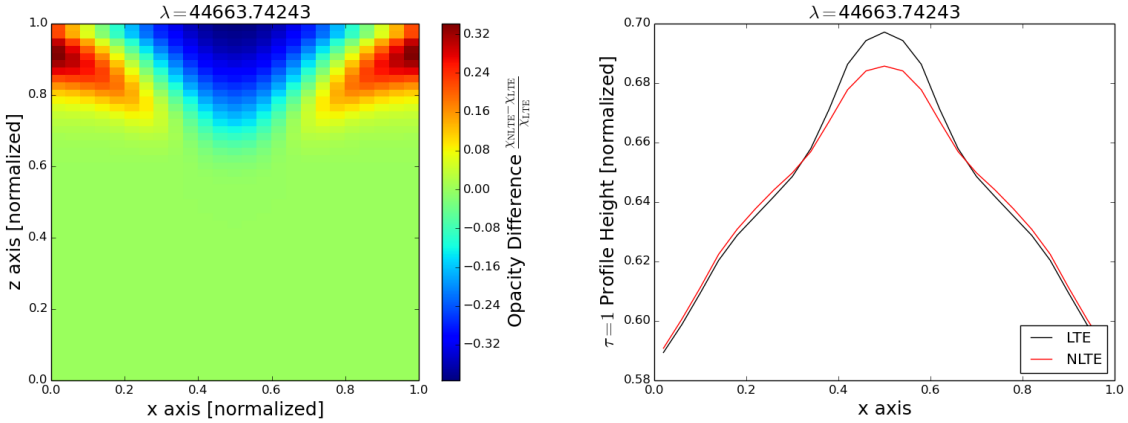

(a) Opacity Difference

(b) $\tau = 1$ Profile

Figure 5.43: Opacity Difference $\frac{\chi_{\mathrm{NLTE}}-\chi_{\mathrm{LTE}}}{\chi_{\mathrm{LTE}}}$ and $\tau = 1$ profile for NLTE and LTE for the CO line at $\lambda = 44663.74$Å.

opacity at the line center wavelength, which is mitigated by the reduced opacities of the underlying continuum for the rim wavelength point.

As expected, the $\tau = 1$ profiles for both line wavelengths are at a shallower depth, compared to the continuum. Both are affected by the difference in opacity, so that the $\tau = 1$ profile recedes even farther into the outside regions of the atmosphere in the center of the anomaly. At the rim point, this effect is again somewhat subdued by the influence of the underlying continuum, so that there is no distinct peak in the profile but a almost constant plateau over the center region of the anomaly. In both cases, the reduced depth of sight shifts the region dominant for the outgoing radiation to cooler parts of the atmosphere, so that a deepening of the lines can be expected.

The NLTE occupation numbers however, somewhat mitigate this effect. Of course, there are no NLTE effects outside of the line, but at line wavelength, the opacity does not increase as much in the upper center of the anomaly. This effect can be seen in detail in Figure 5.43a. The difference in opacity closely follows the departure coefficients of the super ground state shown in Figure 5.41, which this line is coupled to.

The $\tau = 1$ profile is less peaked accordingly, as seen in Figure 5.43b. The depth of sight is greater in the central area of the anomaly, where the opacity is smaller, but is decreased by a small amount outside of the anomaly. The NLTE effects again act as an equalizer, redistributing the effects of the temperature anomaly over an area beyond the boundary of the temperature profile itself.

However, this effect strongly depends on which levels the transition in question is coupled to. As can be seen from the difference in opacity and $\tau = 1$ profile for a different CO line at $\lambda = 44674.57$Å shown in Figure 5.44. This line is not directly coupled to the super ground state and, thus, shows an opacity profile more akin to one of the upper levels, where the opacity increases strongly in the upper parts of the atmosphere, were the over population is highest. Here, the increased opacity within the coldest parts of the temperature structure cause a shallower $\tau = 1$ profile in the center, while the rim of the profile is largely unaffected as the opacity difference is fairly localized. The opacity changes are more localized than for the line coupling to the ground state, but their overall

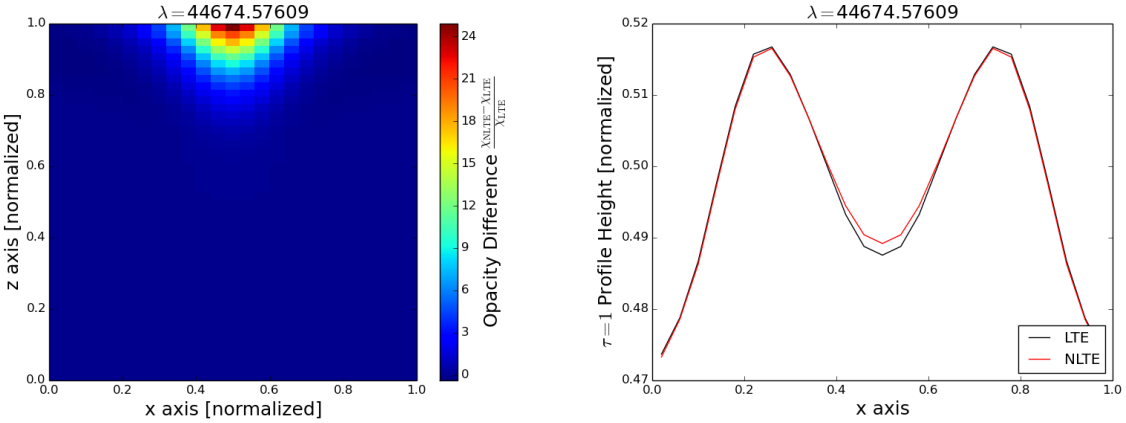

(a) Opacity Difference (b) $\tau = 1$ Profile

Figure 5.44: Opacity Difference $\frac{\chi_{NLTE}-\chi_{LTE}}{\chi_{LTE}}$ and $\tau = 1$ profile for NLTE and LTE for the CO line at $\lambda = 44674.57$Å.

magnitude is higher, due to the fact that the departure coefficients for super levels of higher energy are larger as well.

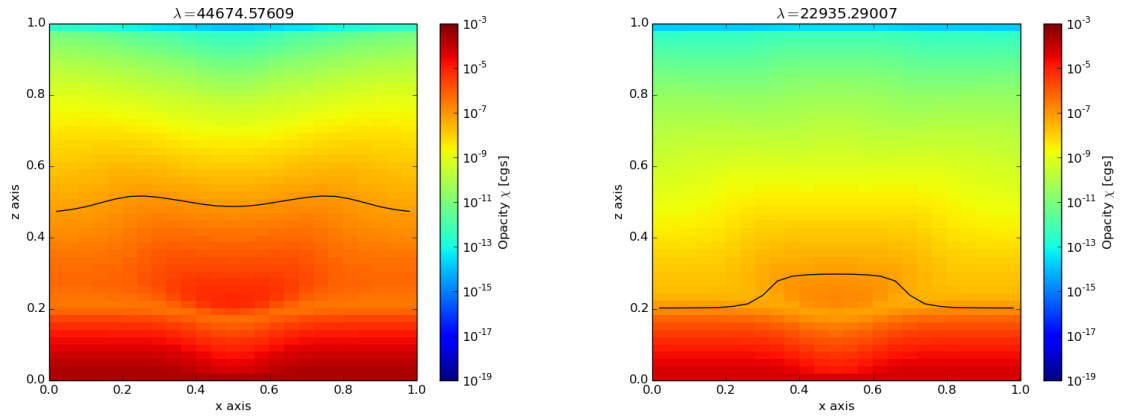

(a) $\Delta\nu = 1$ (b) $\Delta\nu = 2$

Figure 5.45: Opacity for a CO lines coupled to an upper super level and a line of the $\Delta\nu = 2$ band. Black line is level of $\tau = 1$ for a view directly from above.

The overall change to this line differs as well, as can be seen in the LTE opacities for this wavelength shown in Figure 5.45a. The opacity structure in the lower part of the grid is similar, but the upper region shows a decrease in opacity in the coolest parts of the temperature anomaly, which leads to a $\tau = 1$ profile that has its peaks below the flanks of the anomalies structure rather than directly below. This is a result of the LTE occupation numbers that are differently affected for different levels, as they depend on temperature, where upper levels are depopulated with decreasing temperature.

5.4.3 Flux Redirection

The inclusion of a temperature anomaly causes the radiative flux $\vec{F}$ to be partially redirected into the cooler part of the atmosphere. The redirection follows the largest temperature gradient and its magnitude is further determined by the opacity structure of the atmosphere. This effect is strong for line wavelengths, but weak for continuum wavelength points, where the anomaly is mostly optically thin, as can be seen for the xz- and xy-components of the flux in Figures 5.46a and 5.47a.

The flux is redirected directly into the anomaly for the two line wavelengths, albeit to different degrees as both lines differ in opacity structure. At the continuum wavelength point, the magnitude of the redirection is much smaller and the pattern is not as clear-cut. Here, the flux is redirected primarily into the rim of the anomaly.

The changes to the opacity structure discussed in the previous section show once again in the redirection of the flux, as can be seen in the differences between LTE flux and NLTE flux shown in Figures 5.46b and 5.47b. For the strong line coupling to the super ground state for $\lambda = 44663.74$Å, the redirection of the flux into the cooler parts of the atmosphere is reduced. At the same time, the z-component of the flux outside of the core of the structure is decreased, while the outward flux within the coolest parts of the anomaly is increasing. Evidently, as was already seen in the $\tau = 1$ profile, NLTE effects act as an equalizer, spreading the effect of the reduced temperatures over a larger area, but lessen the overall effects in the center of the structure. This will result in a larger area affected by darkening on the surface but a smaller maximum contrast between the inside and the outside.

The transition coupling to an upper state is affected differently. Here, the redirection of flux is increased within the core of the temperature structure itself, where a strong increase in NLTE opacity compared to LTE was found. However, the rim of the structure is almost unchanged in flux, while the redirection in the outer parts and outside of the confines of the anomaly itself is actually reduced. In this way NLTE effects sharpen the core of the anomaly but in turn reduce its perceived size. The vertical changes show an equal decrease of outward flux in the entire upper layer of the atmosphere. In the core of the anomaly, this reduction reaches deeper, while there is an increase of flux below the wings of the temperature structure.

The continuum once again shows changes that are several orders of magnitude smaller and are probably caused by the far wings of lines that are in the vicinity of the chosen wavelength points as well as numerical noise. Also, we still see effects of the periodic boundary conditions, meaning the simulation grid is still too small for the size of the anomaly.

The resulting surface profiles of the flux are shown in Figure 5.48. For the continuum, there is little overall variation in surface brightness. Here, the region where the anomaly resides is optically thin for the most part, so that only its lowest reaches affect the outgoing radiation in a meaningful manner.

For line wavelengths, there is a visible contrast between the rim of the profile and its core. The changes to NLTE opacities and, thus, the depth of sight, ensue a change to the flux profiles of both lines. The stronger line, coupling to the super ground level, shows

a stronger effect that is caused by the strong opacity changes immediately beneath the surface. The contrast between the inside and the outside is reduced, as the effect of the temperature anomaly is spread beyond its size. The rim of the structure is noticeably darker, while the core itself is almost unaffected.

For the other line, the change is, as expected from the resulting diversion of the flux, more uniform in nature and less pronounced overall.

5.4.4 Resulting Spectrum

Figure 5.49 shows the resulting outward flux spectrum $F_z(\lambda)$ for two different points of the surface of the grid. One point was chosen to be above the center of the temperature structure, the other is at the corner of the grid as far from the temperature structure as possible.

The reduction in temperature causes a reduction in outward flux that is especially strong at line wavelengths, caused by the aforementioned additional opacity effects. The continuum is less affected. However, this is wavelength dependent as well, as the continuum near the $\Delta\nu = 2$ band shows a larger difference, compared to the continuum close to the $\Delta\nu = 1$ band of CO lines, though this might just be caused by the overall higher flux in the 23000 Å regime.

The NLTE effects that were seen in the opacities are seen in the lines of the $\Delta\nu = 1$ band, where the spectrum taken from the edge of the grid shows a small degree of shallower lines compared to the LTE case, while the spectrum at the center of the structure is less affected. This is again the effect of equalization. NLTE effects connect spatially distant regions of the atmosphere and cause the overall effect of the reduced temperature to be spread over a larger region, smearing out its profile. The small NLTE effects on the lines, which are in contrast to the opacity changes in the upper atmosphere, can be explained by the fact that most of the NLTE effects are are in an optically very thin region.

In the $\Delta\nu = 2$ band, the CO lines show no significant NLTE effects. As was already seen in the spherically symmetric test cases, and is indicated by the $\tau = 1$ profile in Figure 5.45b, these lines originate from a deeper region of the stellar atmosphere. They are still affected by the presence of the temperature anomaly, as is evident from the reduced flux above the structure, but NLTE effects in the upper atmosphere are of limited consequence, as this region is optically thin for this wavelength.

5.4.5 Conclusions

The introduction of a cool zone into the otherwise hot atmosphere has created a region, where strong NLTE effects are possible. And the influence of the radiation field has spread the darkening effects of the cool zone beyond its physical limits. In this way, NLTE effects act as an equalizer between hot and cool regions, decoupling the resulting surface fluxes from the local temperature in the atmosphere below. In this way, the NLTE effects would act to support the cooling mechanism that creates the spot, as less energy can be transported from hotter regions into the spot, so that its dissolution would be slowed. In general, this means that NLTE effects may have an influence on the lifetime of temperature variations in the photosphere.

The strongest influence is caused by changes to the opacities that shift the regions that are dominant for the outward radiation either upward or downward depending on the local opacity structure for a given wavelength. This effect is dependent on a number of factors, one of them being which levels each transition couples to. In this, it becomes even more important that the super level set up reflects the physical conditions adequately so that only levels that show similar departure coefficients structure are combined. This is important, as the structure of the opacity changes is determined directly by the structure of the departure coefficients.

It was determined that the changes to the opacity struxture in the upper atmosphere are only of limited relevance to the outgoing radiation, as the atmosphere is already either optically thin, as in the $\Delta\nu = 2$ band, or in the process of becoming optically thin. In this way, small scale structures will most likely not have an influence on the overall outgoing spectrum of a star, unless the surface of the star can be resolved, so that individual brightness variations might be deducted. Nevertheless, NLTE effects can not be dismissed out of hand, since even if small scale temperature variations might not be detectable without resolving the surface, the fact that the effect of a temperature variation is spread over a larger area and might, thus increase in influence over the total outgoing spectrum, is still relevant, especially if global temperature variations in the entire atmosphere are considered.

Particularly, due to the fact that molecular lines are strongly affected by molecular NLTE in cool regions of the atmosphere, individual lines might be affected by global temperature variations and show changes, even if the continuum does not.

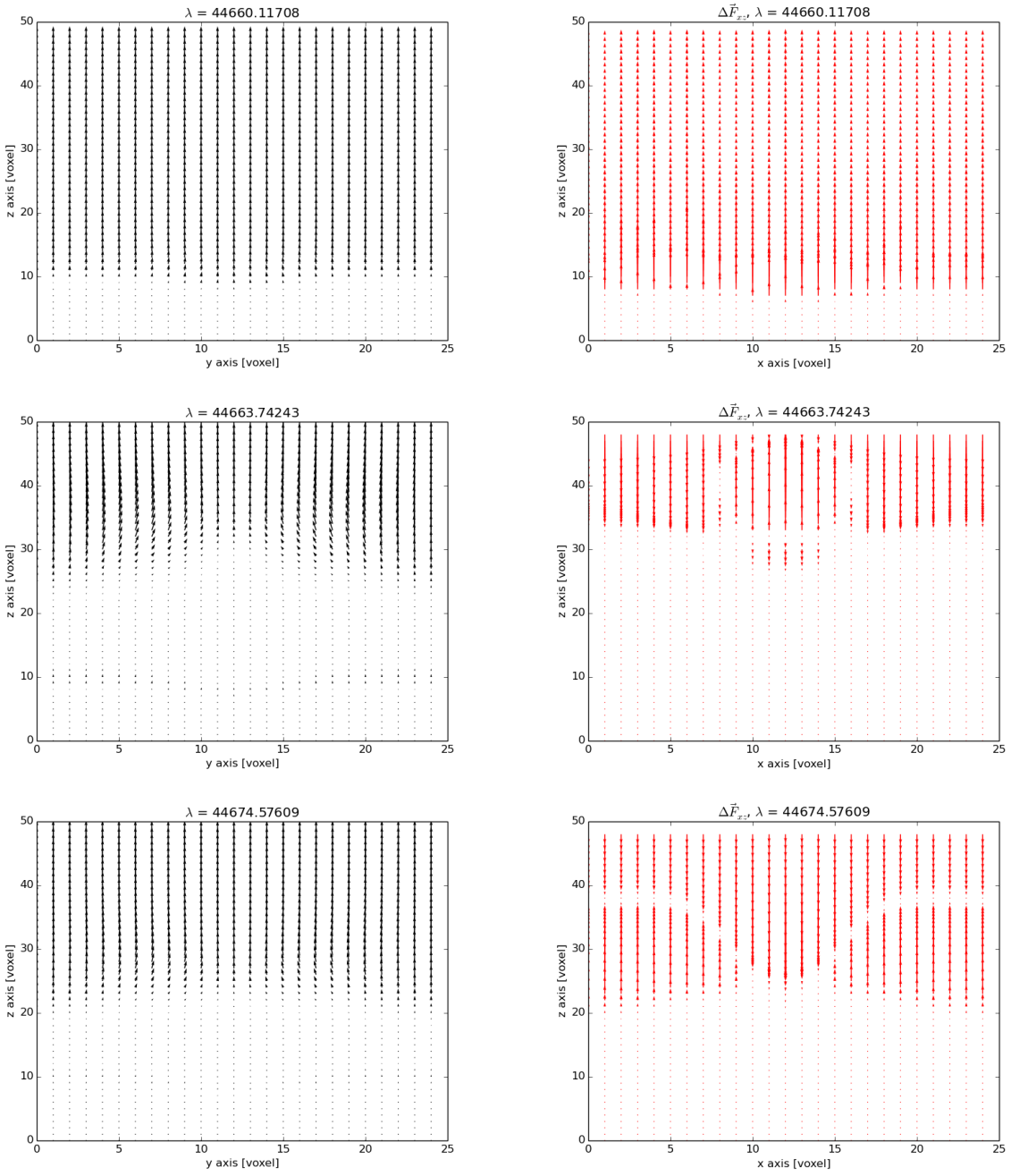

(a) NLTE Flux $\vec{F}_{\mathrm{NLTE}}$

(b) Difference to LTE $\vec{F}_{NLTE} - \vec{F}_{LTE}$

Figure 5.46: Flux, x and z components for a vertical slice of the grid through the core of the anomaly, where the y component should be zero. Shown are both NLTE Flux and difference to LTE flux.

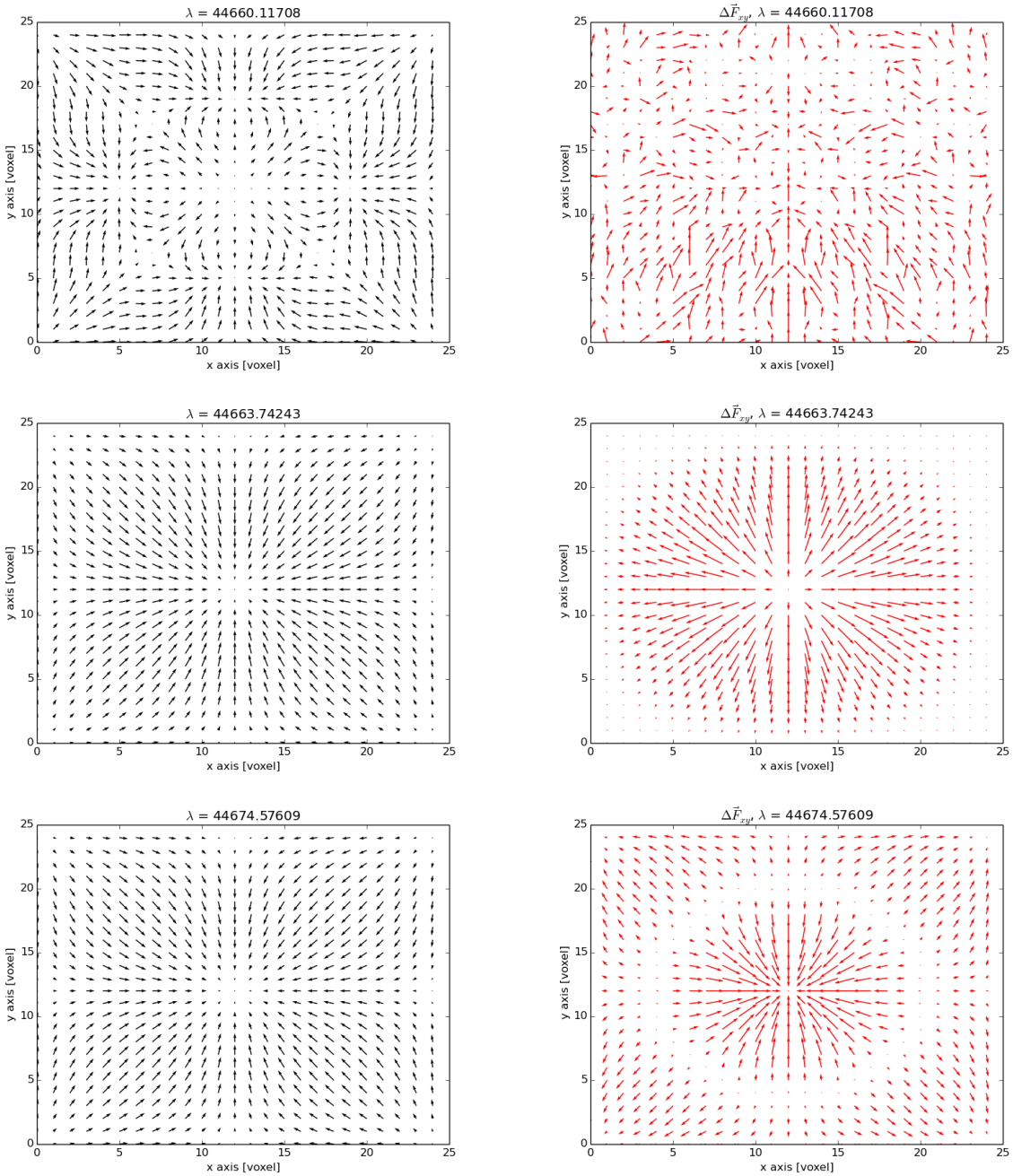

(a) NLTE Flux $\vec{F}_{\text{NLTE}}$

(b) Difference to LTE $\vec{F}_{NLTE} - \vec{F}_{LTE}$

Figure 5.47: Horizontal components of the Flux $\vec{F}$ for a plane through the upper part of the anomaly. Shown are both NLTE Flux and difference to LTE flux.

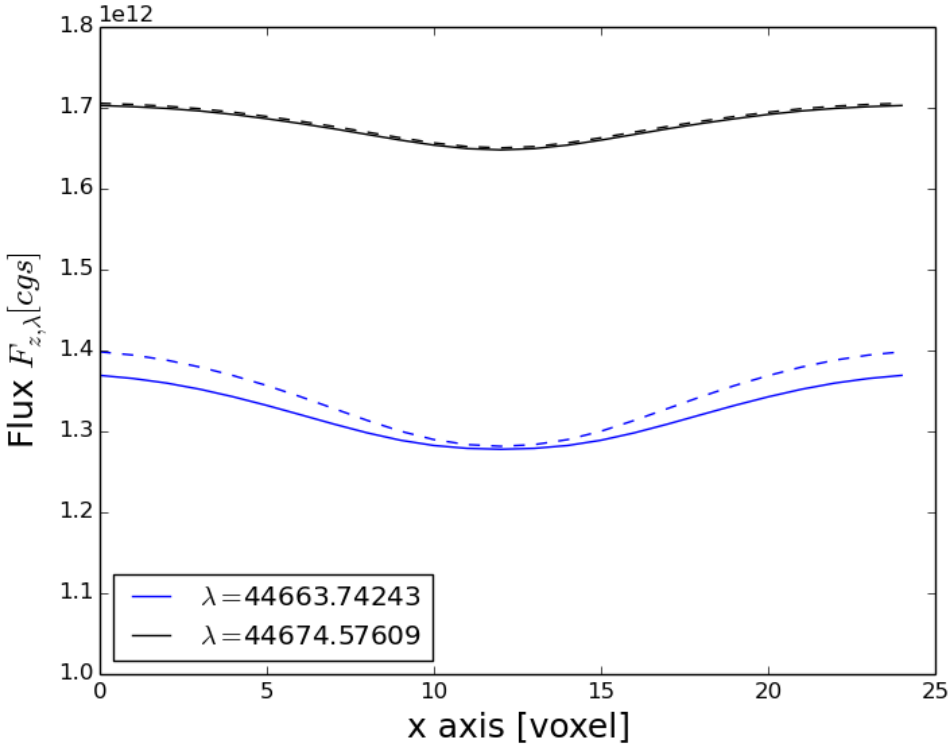

Figure 5.48: Surface flux profile for two different CO line wavelength. Solid lines are NLTE profiles, dashed lines are the LTE results.

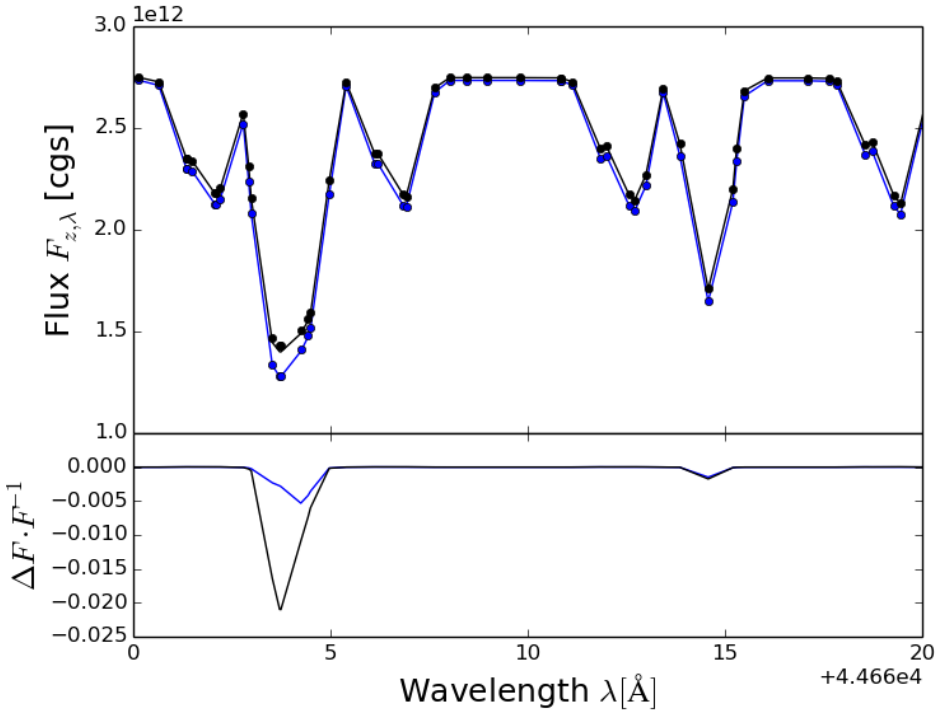

(a) $\Delta\nu = 1$

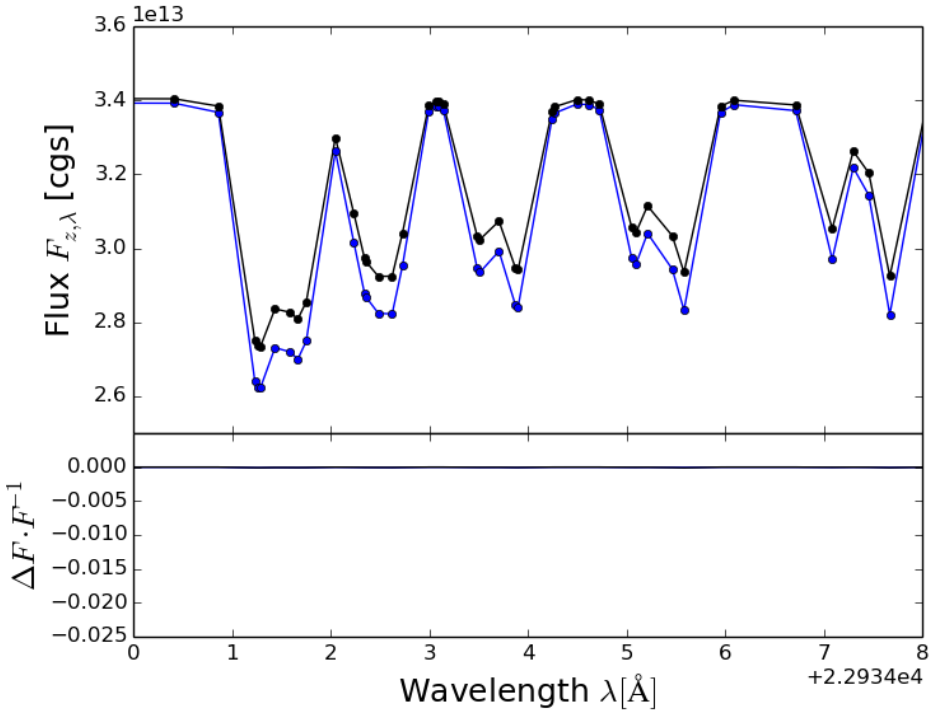

(b) $\Delta\nu = 2$

Figure 5.49: Resulting NLTE flux spectrum for several CO lines of the $\Delta\nu = 1$ and $\Delta\nu = 2$ bands. Black line represents spectrum in the corner of the grid, as far from the anomaly as possible. Blue line is spectrum above the center of the anomaly. Circles represent results of the LTE calculations.

Chapter 6

Future Prospects

The super level method was successfully implemented into the existing 3D radiative transfer framework and passed all standard tests. LTE is restored for with pure collisional excitation and de-excitation, as well as with black body radiation. Furthermore, the spherically symmetric tests reproduced results produced by the well-tested 1D implementation.

The super level algorithm is based on the assumption that individual levels are coupled strongly enough so that they can be treated as a single level, with respect to solving the rate equations. A comparison between the 3D super level NLTE results with the full level 1D NLTE results show that even super level configurations with a small number of super levels produce results that are reasonably close to more detailed calculations, given that the super levels are set up reflecting physical conditions. At the same time, the use of the super level algorithm drastically reduces both the computation time for the solution of the rate equations as well as the overall memory requirements.

Specifically, a selection of levels by excitation energy seems to be the best, so that models using energy as the sole criterion or one of the criteria produce the most accurate results.

The radiative rates lead to a more uniform population of levels in NLTE, while upper levels are exponentially less populated in LTE. Hence, we see a strong overpopulation in levels with high excitation energy. Levels with similar energy show similar departure coefficients, so that they can be combined into one super level with less loss of accuracy than if levels of vastly different departure coefficients were combined. However, this is only true as long as the upper levels are comparatively unpopulated in LTE. It might also change if additional non-CO lines in the vicinity of the CO lines are included and influence individual radiative rates by changing the mean intensity at CO line wavelength, which would require the use of a full line list. To ensure that the super level configuration always reflects the physical conditions, 1D tests using the full number of molecular levels should be used to find accurate super level configurations for different scenarios.

It would be of interest to test the different models for conditions outside of the photosphere or even outside of stars. For instance, chromospheres would be an interesting testing ground, as they have vastly different temperature and pressure structures with high temperatures and low pressures so that we would expect very low collisional rates while they are also optically thin, therefore, suggesting strong NLTE effects. Furthermore, the high temperatures in chromospheres will support much higher LTE population of highly energetic excited states of the molecules even without the influence of the radi-

ation field. Apart from chromospheres, giant branch stars might be another interesting testing ground, due to the fact that they have a different pressure structure. Additionally, the larger size of the star and therefore, a significantly larger optically thin region where the radiation field varies, might cause NLTE effects in entirely different parts of the atmosphere.

Beyond stars, the simulation of planetary atmospheres is another large field that could profit from the inclusion of molecular NLTE. Planetary atmospheres show in most cases temperatures that allow the formation of molecules. NLTE effects will most likely be found in the upper parts of planetary atmospheres where it is optically thin, given that the irradiation from the planets star is strong enough to support a radiation field that supersedes the collisional rates within the atmosphere and, thus, causes NLTE effects. However, if the irradiation is too strong and causes extreme temperatures in the atmosphere, it might also produce collisional rates that are high enough to suppress the radiative rates at least in part and cause a thermalization of the atmosphere so that NLTE effects will be relevant only in distinct parts of the atmosphere. In any case, this might have influence on transmission and reflectance spectra of the planet as different parts of the atmosphere are affected differently.

The results are consistent in the fact that NLTE effects are found where the atmosphere is optically thin so that the influence of the radiation field created by deeper, hotter layers of the atmosphere is dominant, while the electron densities and therefore, the collisional rates are low or non existent. This is, of course, biased by the fact that the collisional rates that were included into the calculations consisted solely of electron collisions. However, collisions with atoms such as hydrogen and helium should not be entirely neglected, in particular in regions where the electron densities are low so that these particles might dominate the collisional rates. Therefore, the results shown here lack one factor that would act to restore LTE conditions and, thus, limit the magnitude of the NLTE effects. However, the collisional rates also decrease with temperature and pressure. Hence, it is likely the increase in collisional rates through the inclusion of additional species will not be sufficient to cancel it out completely.

In general, this might confine NLTE effects to regions of even lower optical depth as the threshold below which NLTE effects occur gets slightly decreased by the inclusion of the additional collisional possibilities.

Since collisional rates for the particles mentioned are already included in the 1D implementation, even if they were disabled for the comparison, it is the logical next step to include them into the 3D implementation as well.

This will reduce the large departure coefficients seen in the optically thin parts of the atmosphere. Yet, due to the fact that the lines of both strong molecular bands with $\Delta\nu = \{1, 2\}$ are formed in regions below this region, we expect the changes this causes to the spectral lines to be rather small, at least for the models shown in this work. Most likely, the effect will be an additional variation in the $\tau = 1$ profile caused by the opacity additional changes in the uppermost layers of the photosphere which will translate to a slight shift in line depths.

To investigate the influence of the NLTE on the spectrum of an unresolved star, it would be interesting to simulate large scale temperature and pressure variations that are

distributed over the whole photosphere, as opposed to the very small scale models that were simulated here. Global temperature variations will have a much larger influence than a single local feature and should therefore, affect individual lines. However, this might require an increase of wavelength resolution to be able to show even small changes to the line shape in the outgoing spectrum caused by the angle integration over the whole surface, which, as was shown in this work, is computationally very expensive.

To circumvent this, the most important lines for NLTE effects, meaning those most strongly affected, have to be identified a priori. The most significant lines can then be sampled with high resolution individually. With respect to CO and atmospheric structures similar to those used in this work, this will most likely entail the strongest lines of the $\Delta\nu = 1$ band in the far infrared around 4.4μm, which are formed in regions where significant NLTE effects are found. The lines of the $\Delta\nu = 2$ band around 2.3μm are, at least in the models that were considered in this work, unaffected as they form deeper in the photosphere - however, this also might differ for vastly different temperature and pressure structures as found, e.g., in chromospheres or diverse planetary atmospheres.

Most promising for further investigation is how NLTE opacities affect the perceived structure of varying temperature compared to the actual structure of the temperature. The radiation field links spatially distant parts of the atmosphere that would initially be independent of each other. This leads to an equalization of the radiation field that would have seen a reduced intensity within cool zones of the atmosphere in LTE and an increased opacity in the hotter zones. The horizontal fluxes within the atmosphere change magnitude and to some extent even direction.

While this effect might not seem to be relevant by itself, as the surface of stars can usually not be resolved by current techniques, it has implications for the global temperature structure of the star. Without a stabilizing influence, physics would dictate that energy is redistributed from hotter to cooler regions, so that the temperatures would be equalized after a certain time. It is already known that this effect can be counteracted by local conditions, as the interaction between magnetic fields and convection cells forms both large and small-scale patterns of varying temperature on the surface of stars with varying lifespans.

In general, radiation is assumed to be supportive of any dissolution process that counteracts the forces stabilizing a varied temperature structure, as radiation is the primary way of energy transport within the photosphere. In LTE conditions, this effect leads to fluxes being redirected into any cool part of the atmosphere and changes to the $\tau = 1$ profile and, thus, the surface intensities as was already shown in previous work.

In NLTE, however, any cool zone might show an increased NLTE effect for molecules that have widespread bands of lines and, thus, affect photons at many different wavelengths. Hot zones, on the other hand, will show very different NLTE effects as the increased collisional rates cancel out the radiative rates to different degrees. This effect is further influenced by pressure and the density of both electrons and other species. NLTE effects spread the effect of any temperature variation beyond its physical limits while at the same time reducing its absolute differential between the inside and the outside. This affects the redirection of energy within the atmosphere so that energy is not redistributed into cool zones as efficiently but rather into regions surrounding the coolest zones that would usually be less affected.

By these means, cool regions within the photosphere gain an additional mechanism to stabilize themselves as the energy transport from hot regions to cool regions is, in part, inhibited. This is, of course, never the most significant mechanism of supporting cool zones but can bolster other effects already at work. On a global scale, this might lead to significant changes to the temperature structure of the photosphere, which might, in turn, have widespread effects on all measurements and simulations that use these as a prerequisite, such as the calculations of abundances. Additionally, we would expect that NLTE effects are not just relevant for the stability of temperature anomalies, but would also influence their formation mechanism in a similar manner.

In 1D, the effects of the temperature structure have already been studied, for instance by Schweitzer [1999]. However PHOENIX/3D does not currently support any means by which the temperature structure could be converged for radiative equilibrium. For this reason, it would be interesting to combine molecular NLTE as presented in this work, with radiation hydrodynamics to be able to investigate the dynamics of a system like this. As a first step, it would, for instance, be possible to use magneto-hydrodynamic models as a temperature structure to determine, how strong the effect seen in the parametrized models is in a more realistic temperature and pressure structure. Furthermore, this allows simulations of large scale structures as well, where we might see different effects as the variations of temperature and pressure affect a large region, but the variations themselves are smaller than those seen for very localized structures such as spots.

For the first tests, it is advisable to use structures seen on the solar surface, in particular those that feature a strong temperature differential. Using the sun has the benefit that direct observations of surface profiles for such structures is actually possible. In this way, it is possible to use observations for comparison directly without the problem that NLTE effects have to contribute to the integrated spectrum to be observable. In particular, 3D opacity structures have already been shown to produce different $\tau = 1$ profiles for different angles of view μ by Berkner et al. [2013] and, therefore, probe different layers of the atmosphere. As NLTE effects further change the shape of the $\tau = 1$ profile which will also affect the changes seen under different angles of view, NLTE effects will show in the limb darkening seen for surface structures such as sunspots. Thus, a number of additional observations are possible by tracking distinct structures on the solar surface from the solar center to the limb and comparing the results to the predicted limb darkening for different wavelengths. The result will directly show, how well the opacity structure has been modelled.

One aspect that needs to be revisited to be able to simulate both the influence of large global structures and small localized structures is the set-up of the grid. In this work, we have used either spherical models of an entire stellar atmosphere or plane-parallel models that focused on small-scale structures. Here, the model grid was set-up to use a symmetric distribution of voxels, were all voxel at the same depth have the same size. However, this would require an extremely high spatial resolution to adequately probe both local and global temperature structure. As the necessary computation time is linear in the number of voxels, extreme spatial resolutions would be expensive. The better way would be the use of an adaptive mesh grid that can be set-up in a way that allows for highly detailed structures were necessary without unnecessarily increasing the number of voxels in the more homogeneous parts of the atmosphere.

Note that, while MHD simulations can produce a consistent input temperature struc-

ture, they can not cover all possible temperature structures a star might have at any given moment. Individual structures might be used for comparison with the sun, but for all stars beyond the sun, the idea of 3D simulations is not to completely model the stellar surface in all details. The purpose of 3D simulations is to be able to include the possibility of complex temperature structures at all. As was shown in this work, even NLTE effects for just one molecular species in just a simple parametrized structure have a varying influence on the spectrum of a star, where each line is affected in its own way depending on the molecular states that it is coupled to. Knowing this, we can be certain that no individual line will be able reveal all the information that is be necessary to deduce if certain effects like starspots or accretional heating are present or not.

The use of MHD simulations is also a prerequisite for the investigation of the influence of magnetic fields on NLTE effects. As they change the level structure of atoms and molecules and, thus, shift the position of spectral lines, magnetic fields will influence the radiative rates. As with the temperature structure, we will likely see a redistribution of that influence of NLTE effects that connect spatially distant parts of the atmosphere for the same reasons as given before. However, this would also massively add to the complexity of the wavelength integration problem as the number, position, and shape of spectral lines shows differences between different parts of the simulation box, but the radiative transfer requires that all wavelengths points are calculated on all voxels.

In conclusion, the implementation of 3D NLTE for molecules has already shown that there is indeed a significant 3D influence both on the structure of the photosphere as well as the outgoing spectrum. The use of the super level algorithm has proven that it is possible to achieve an NLTE solution in 3D without exceeding the limits of computation time and memory, even if the requirements are still steep.

This work can now be used as a base to expand the algorithm and delve into the investigation of more detailed problems. However, several of the problems that turned up during the course of this investigation might have to be revisited in the future as the complexity of the models is increased.

In this work, only one molecular species was considered. Different species could be treated the same way, even if molecules with a significantly higher number of spectral lines as CO might pose an additional problem.

However, treating molecular species isolated is another approximation. Usually, there are several molecular species present at the same time and in regions, were NLTE effects are relevant for one species, it is likely that the radiation field will have a strong influence on the population of more than one species. As the interaction between different species is not only relevant due to overlapping lines, but also due to the fact that the rate equations for all species are linked through the electron density, another level of detail that should be treated is added to the problem, increasing the number of necessary wavelength points even further.

This is linked with a different aspect that was only discussed briefly thus far. In this work, ionization has only been treated in an extremely simplified manner, and molecule formation and NLTE dissociation have been neglected completely for reasons of simplicity and computational feasibility. In this way, the total CO number densities are only determined by temperature and pressure and independent of the radiation field. Ideally,

the NLTE solution should be linked with the equation of state, so that photo-dissociation and re-association is possible. A solution of what would then be called non local chemical equilibrium (NLCE) would undoubtedly, have a significant influence on the distribution of CO or any other molecule, especially at the rim of the molecular rich regions. In combination with radiation hydrodynamics, this would allow simulation of most of the dynamics between radiation field, equation of state, as well as temperature and pressure structure consistently - however, given the requirements of the NLTE problem alone, this is a task that has to be deferred to future generations of super computers.

Bibliography

C. W. Allen. *Astrophysical Quantities*. Athlone Press, London, Third Edition edition, 1973.

L. S. Anderson. Line blanketing without local thermodynamic equilibrium. II - A solar-type model in radiative equilibrium. *ApJ*, 339:558–578, Apr. 1989.

M. Asplund, N. Grevesse, and A. J. Sauval. The Solar Chemical Composition. In T. G. Barnes III & F. N. Bash, editor, *Cosmic Abundances as Records of Stellar Evolution and Nucleosynthesis*, volume 336 of *Astronomical Society of the Pacific Conference Series*, page 25, Sept. 2005.

D. H. Bailey, Y. Hida, X. S. Li, and T. Brandon. ARPREC: An arbitrary precision computation package. Technical report, Lawrence Berkeley National Laboratory, Berkeley, CA 94720, 2002.

E. Baron and P. H. Hauschildt. A 3D radiative transfer framework. II. Line transfer problems. *A & A*, 468:255–261, June 2007.

A. Berkner. 3D Radiative Transfer Simulation of Starspots in Stellar Atmospheres, 2011.

A. Berkner, P. H. Hauschildt, and E. Baron. 3D radiative transfer effects in parametrized starspots. *A & A*, 550:A104, Feb. 2013.

C. J. Cannon. Angular quadrature perturbations in radiative transfer theory. *J. Quant. Spectrosc. Radiat. Transfer* , 13:627–633, 1973.

A. Einstein. Zur Quantentheorie der Strahlung. *Physikalische Zeitschrift*, 18:121–128, 1917.

D. Goorvitch. Infrared CO line for the X 1 Sigma(+) state. *Astrophys. J. Supp.*, 95: 535–552, Dec. 1994.

D. Goorvitch and C. Chackerian, Jr. Calculation of (12)C(16)O and (13)C(16)O X(1)Sigma(+) rovibrational intensities for V less than or equal to 20 and J less than or equal to 150. *Astrophys. J. Supp.*, 91:483–489, Mar. 1994a.

D. Goorvitch and C. Chackerian, Jr. Rovibrational intensities of the minor isotopes of the CO X ^{1}Sigma $^+$ state for V less than or equal to 20 and J less than or equal to 150. *Astrophys. J. Supp.*, 92:311–321, May 1994b.

P. H. Hauschildt. A fast operator perturbation method for the solution of the special relativistic equation of radiative transfer in spherical symmetry. *J. Quant. Spectrosc. Radiat. Transfer* , 47:433–453, June 1992.

P. H. Hauschildt. Multi-level non-LTE radiative transfer in expanding shells. *J. Quant. Spectrosc. Radiat. Transfer* , 50:301–318, Sept. 1993.

P. H. Hauschildt and E. Baron. Numerical solution of the expanding stellar atmosphere problem. *Journal of Computational and Applied Mathematics*, 109:41–63, Sept. 1999.

P. H. Hauschildt and E. Baron. A 3D radiative transfer framework. I. Non-local operator splitting and continuum scattering problems. *A & A*, 451:273–284, May 2006.

P. H. Hauschildt and E. Baron. A 3D radiative transfer framework. III. Periodic boundary conditions. *A & A*, 490:873–877, Nov. 2008.

P. H. Hauschildt and E. Baron. A 3D radiative transfer framework. IV. Spherical and cylindrical coordinate systems. *A & A*, 498:981–985, May 2009.

P. H. Hauschildt and E. Baron. A 3D radiative transfer framework. VI. PHOENIX/3D example applications. *A & A*, 509:A36+, Jan. 2010.

P. H. Hauschildt and E. Baron. A 3D radiative transfer framework. XI. Multi-level NLTE. *A & A*, 566:A89, June 2014.

R. C. Hilborn. Einstein coefficients, cross sections, f values, dipole moments, and all that. *ArXiv Physics e-prints*, Feb. 2002.

A. A. Kutepov, D. Kunze, D. G. Hummer, and G. B. Rybicki. The solution of radiative transfer problems in molecular bands without the LTE assumption by accelerated lambda iteration methods. *J. Quant. Spectrosc. Radiat. Transfer* , 46:347–365, Nov. 1991.

D. H. Menzel and G. G. Cillié. Hydrogen Emission in the Chromosphere. *ApJ*, 85:88, Mar. 1937.

D. Mihalas. *Stellar Atmospheres.* A Series of Books in Astronomy and Astrophysics. W. H. Freeman and Company, San Francisco, 1970.

D. Mihalas. *Stellar Atmospheres.* W. H. Freeman and Company, San Francisco, Second edition, 1978.

G. L. Olson and P. B. Kunasz. Short characteristic solution of the non-LTE transfer problem by operator perturbation. I. The one-dimensional planar slab. *J. Quant. Spectrosc. Radiat. Transfer* , 38:325–336, 1987.

R. J. Rutten. *Radiative Transfer in Stellar Atmospheres.* Utrecht University lecture notes, 8th edition, 2003.

G. B. Rybicki and D. G. Hummer. An accelerated lambda iteration method for multilevel radiative transfer. I - Non-overlapping lines with background continuum. *A & A*, 245: 171–181, May 1991.

A. Schweitzer. *Spectra of M dwarfs: in non-LTE and with low metallicities*. PhD thesis, Universität Heidelberg, 1999.

A. Schweitzer, P. H. Hauschildt, and E. Baron. Non-LTE Treatment of Molecules in the Photospheres of Cool Stars. *ApJ*, 541:1004–1015, Oct. 2000.

S. Wedemeyer, B. Freytag, M. Steffen, H.-G. Ludwig, and H. Holweger. Numerical simulation of the three-dimensional structure and dynamics of the non-magnetic solar chromosphere. *A & A*, 414:1121–1137, Feb. 2004.

Acknowledgement

I'd like to thank all the people who helped with this work in one way or another and without whom this work would never have been finished.

First of all, I want to thank my advisor Peter Hauschildt for introducing me to the mysteries of radiative transfer, for answering all my questions and always pointing me towards the solution of any problem - and also for his unique way of running the PHOENIX group.

I'd also like to thank Andreas Schweitzer for laying the foundation of the Sybil code in 1D for me to build upon as well as for remembering every little detail of the old code and, thus, always having an answer why something was done in one way or another. Thanks for the general support of anything related to FORTRAN as well, and also for proof reading this work.

I also want to thank Soeren Witte for his help, for strange scientific and non-scientific discussions, for doing his best to keep me motivated through dire weeks of debugging and for being one of the pillars of this work group. I also thank him for being an amazing proof reader.

Thanks to Eddie Baron and his work group at the Oklahoma University for the collaboration and for an amazing stay in Norman. I'd like to thank Eddie in particular for discussing the results of this work with me as well as for proof reading this work.

Of course, I also thank all the other members of the PHOENIX group at the Hamburg Observatory who at one time or another shared office space, discussions and lunch breaks with me.

I also thank the rest of the members of my examination commission Dieter Horns, Robi Banerjee, Marcus Brüggen and Robert Baade.

The calculations presented in this work were done using a generous allocation of computing time of both the NERSC and the HLRN. This work was financed by the DFG. I'd like to thank all three organisations for their support.

Last but never least, I want to thank my parents and my friends for their everlasting support and Melanie Alke for always being the brightest star in my universe.

Eidesstattliche Versicherung

Hiermit erkläre ich an Eides statt, dass ich die vorliegende Dissertationsschrift selbst verfasst und keine anderen als die angegebenen Quellen und Hilfsmittel benutzt habe.

(Alexander Berkner)
Hamburg, 04. November 2014